FEMTOSECOND LASER INSCRIPTION OF OPTICAL WAVEGUIDE-BASED DEVICES ON LITHIUM NIOBATE

TEERAWAT PIROMJITPONG

Doctor of Philosophy

ASTON UNIVERSITY

July 2019

Aston University

Femtosecond Laser Inscription of Optical Waveguide-based Devices on Lithium Niobate

Teerawat Piromjitpong, Doctor of Philosophy, 2019

Abstract

This work explored the use of high-repetition-rate femtosecond laser pulses for the direct writing of optical waveguide-based devices in a sample of z-cut lithium niobate crystal. The effects of inscribing parameters including pulse energy, writing speed, writing direction and focus depth on the optical and physical properties of a laser-induced straight structure were revealed, and systematically investigated for the optimal regime of low-loss waveguide fabrication. Also, the impacts of optical aberrations due to refractive index mismatch and birefringent astigmatism on the laser focus were numerically studied and discussed with the results obtained from the experiments. To test the thermal-dependent characteristics of an inscribed sample, a series of heat treatments in a temperature range between 250 ^{o}C and 950 ^{o}C was applied. It was found that the heats up to the temperature of 500 ^{o}C enhanced the overall refractive index contrast of a Type-II laser modification, and also reduced the residual stress. For the temperatures greater than 500 ^{o}C, the annealing resulted in the deterioration of an inscribed structure.

In the part of straight waveguide fabrication, an optical-lattice-like geometry which consisted of multiple damaged tracks arranged in a multi-layer hexagonal packing was implemented for writing the depressed-cladding waveguide with various sets of inscribing parameters. To address the laser-focusing issue stemmed from the spherical aberration effects, the pulse-energy variation schemes were applied – resulting in more circular and symmetric optical mode-fields. The lowest propagation losses of (0.4 ± 0.1) dB/cm and (3.5 ± 0.2) dB/cm for TE and TM polarised light, respectively, at 1550 nm were achieved after thermally annealed at 350 ^{o}C for 3 hours. In addition, the waveguides were found to be thermally stable and showed the low-loss guiding up to the temperature of 700 ^{o}C. The fundamental guiding mode was observed over a wide range of spectral from 500 nm to 1550 nm.

Our laser inscription technique was also applied to fabricate the s-bend structures and power splitters which were based on the multi-mode interference. The computer simulation in COMSOL was used to optimize the interference pattern inside the waveguides such that the high intensity transmission could be obtained. The lowest insertion losses in TE mode of (4.23 ± 0.14) dB and (4.31 ± 0.20) dB for the two-output and three-output splitters, respectively, at 1550 nm were measured after the sample was annealed at 250 ^{o}C for 3 hours. Besides, the integration of s-bends and the splitter to allow the wider separation (293.7 μm) between two splitter's output branches was demonstrated. The insertion loss of this structure was found to be (4.96 ± 0.17) dB, and the splitting ratio of 0.48:0.52 was achieved for the TE propagation mode.

Keywords: femtosecond laser, laser-material processing, depressed-cladding waveguide, multi-mode interference splitter, s-bend waveguide

Acknowledgements

I would like to express my special gratitude to my supervisors Dr Sonia Boscolo and Dr Mykhaylo Dubov for the opportunity to work on this project, the immense knowledge and the continuous supports on my PhD research and thesis writing.

My sincere thanks also go to the Thai government and Aston university for the financial supports during my PhD study.

Last but not least, I am very grateful to my parents, my sister and friends for the precious supports and encouragements throughout my study and my life.

Teerawat Piromjitpong

List of contents

List of tables

List of figures

Chapter 1

Introduction

This chapter of the thesis introduction consists of three main sections that include the review of relevant literatures in the ***Section 1.1***, the study aims and scopes in the ***Section 1.2*** and the brief descriptions of the remaining chapters of this manuscript in the ***Section 1.3***. In the Section 1.1, the literature reviews will start by shortly explaining about the concept of the integrated photonics (IP) and will then discuss about the major material platforms, whose technical advantages and downsides regarding the optic and photonic applications will be elucidated, for the integrated photonics (IP) technologies. The Section 1.1.2 will describe the technique of micro-optical-device fabrications based on a femtosecond-laser inscription which is indeed a matter of interest of this study. Then, the Section 1.1.3 will introduce some physical mechanisms of laser-matter interactions that have been typically used for explaining the phenomena of femtosecond-pulse-induced modifications occurred on a dielectric medium. In the Section 1.1.4, a comprehensive review on the previous works on the femtosecond-laser writing of waveguides in a lithium niobite substrate will be presented. The section will summarize the experimental details and the key results of differing studies which will be used for our technical comparisons and discussions. Also, the research works on pulse-laser inscriptions of optical guiding structures on other types of well-known material platforms such as silicon (Si), indium phosphide (InP) and beta-barium borate (β-BaB_2O_4) will be mentioned in the Section 1.1.5.

1.1 Review of literatures

1.1.1 Material platforms for integrated photonics (IP)

The idea to combine many waveguide-based optical structures of different functionalities such as power splitters, gratings, optical modulators and so on into a compact-size device dating back to the mid-1990s [1] has been continuously studied and focused by researchers of many disciplines until nowadays. The modern term, 'integrated photonics (IP)', has been widely used to describe such optical systems, as well as other structures that share similar criteria. A variety of material platforms for IP were purposed, and some have become outstanding choices including silicon (Si), indium phosphide (InP), beta-barium borate (β-BaB_2O_4), lithium niobate ($LiNbO_3$) and so forth.

Silicon (Si) is considered the most CMOS-compatible material for IP, which allows the integrations of optical and electrical components via the conventional lithography-based micro-fabrications. This benefits the rapid developments in the well-controlled and scalable manufacturing environments and, thus, accelerates the growth in the research field of the so-called 'silicon photonics'. Due to the Si's intrinsic properties of an indirect bandgap and the lack of optical second-order nonlinearities, these prevent the pure-Si platform for the fabrication of an efficient active optical device such as light sources, detectors and modulators. To overcome these important issues, some researchers had recently reported on the integrations of Si substrates and other active photonic materials by means of various wafer bonding and/or epitaxial growth techniques. These choices of combined active materials may include a III-V compound semiconductor for the laser emissions at 1.3 μm [2], [3], a germanium (Ge) semiconductor for the light detections at 1550 nm [4], [5] and a $LiNbO_3$ crystal for the second harmonic generations (SHG) [6] and the electrooptic (EO) modulators [7]. However, because of a significant amount of coupling losses could be occurred due to the heterogenous-material structures, the fabrications of a complex IP circuit that composes of several components still a demanding task of this Si platform. Also, the Si's high optical absorption in the visible and ultra-violet spectrums have prevented it from being a versatile material platform for some kinds of applications such as optical sensors and optical spectroscopy.

Indium phosphide (InP) is a binary III-V semiconductor that has a direct bandgap of 1.344 eV, which corresponds to the photon wavelength of 923 nm at 300 K. In addition, its bandgap can be modified by combining it with other III-V semiconductors via certain approaches such as the selective-area epitaxial growth [8] and the core/shell heterostructures [9], making it a suitable medium for the applications of optical transmitters and receivers that can possibly operate in a broad spectrum range [8], [10]. The InP-based photonics has been intensively studied over decades by utilizing the lithographic and epitaxial techniques, nearly similar to that of the CMOS

technologies, resulting in its own state-of-the-art micro-fabrication process. This enables the efficient integrations of a number of optical and electrical components on a chip-sized device in large-scale manufacturing [11]. For example, a circuit of monolithic InP transmitter reported in [12] was demonstrated to operate at a high transmission rate of 2.25 Tbit/s over 40 wavelength-channels with a spectral bandwidth of 1 THz. This transmitter circuit consisted of 40 tuneable distributed feedback lasers that each connected to two optical paths of Mach-Zehnder modulators. However, it has been known that InP has a high degree of free-carrier absorptions which intrinsically occur at a photon wavelength less than 950 nm [13] that has limited its potential uses only in the spectrum range between the near-infrared and the mid-infrared wavelengths.

Beta-barium borate (β-BaB_2O_4) is an inorganic and birefringent compound, that is well-known for the applications in nonlinear optics and quantum photonics. Although it only has a moderate nonlinear coefficient of $d_{22} \approx 2.2$ pm/V, it has been still considered an attractive material because of its unique property of high transparency in a broad spectrum ranging from the deep ultraviolet to the mid-infrared ($\lambda \approx 190 - 3500$ nm). Beta-barium borate also has a high optical damage threshold that is suitable for the applications such as an entangled photon generation [14], a THz-pulse generation [15] and an optical parametric amplification [16], which are required to operate in the working condition of high optical-peak-intensity. Some literatures have been reported on the fabrications and analysis of optical waveguide structures on a substrate of β-BaB_2O_4 which were aimed for the applications in integrated photonics (IP). Typically, the fabrication methods used in these studies involved an ion-implantation [17]–[20], an organic-free hydrothermal method [21] and a femtosecond-laser inscription [22], [23].

Lithium niobite ($LiNbO_3$) is also one of the well-known material platforms for IP technologies, especially, in the nonlinear optics applications. $LiNbO_3$ has a wide transparency window ranging from 320 nm to 5 μm and a high nonlinear coefficient of $d_{33} \approx 31.5$ pm/V. By considering these two properties, lithium niobite is no doubt a preferred material for applications such as an electro-optic modulator [24] and a frequency conversion like a second-harmonic generation [25], and an optical parametric oscillators [26]. $LiNbO_3$ can be also combined with differing dopants such as Er, Fe, Ti, Mg and Zn in order to modify its optical and physical properties. For example, a waveguide laser fabricated on $LiNbO_3$ could be selectively doped with Er by a diffusion doping method [27] and was demonstrated to emit light at around 1550 nm wavelength [28]. To construct the laser cavity structures such as distributed Bragg reflectors (DBR), a Fe-doping was applied to enhance the photorefractive sensitivity of $LiNbO_3$ for a holographic grating patterning [29]. A doping of Ti in $LiNbO_3$, in addition to the uses of depressing the refractive index for waveguide cladding, had been also reported for adjusting the elasticity of the host medium for the surface acoustic waves (SAWs) devices such as an acousto-optically tuneable laser intracavity [28], [30]. It has been demonstrated that when the $LiNbO_3$ was

doped with a Mg-element the $LiNbO_3$ crystal had shown an improved optical damage threshold (a photorefractive damage resistance) of up to 3-4 times greater than that of an undoped substate when tested with both CW lasers [31] and pulsed lasers [32]. Hence, these significant improvements of optical damage-resisting capability have resulted in the expansions of $LiNbO_3$'s applications into the fields of high-power and high-peak-intensity lasers.

1.1.2 Femtosecond-laser inscription of optical structures

There are several micro-fabrication methods, such as Ti in-diffusion and ion implantation, that have been conventionally used for locally modifying a refractive index or other optical properties of a transparent dielectric material to construct a structure of optical devices. These methods are based on the lithographic techniques, which were typically required the multiple steps of fabrications e.g. UV-mask patterning, chemical diffusing, thermal annealing, and so on. Also due to the natures of the mentioned processes, the optical structures are likely restricted to a two-dimensional fabrication plane and, hence, may limit the practicable complexities and functionalities of an integrated photonics (IP) device manufactured by the mentioned methods. On the other hand, the femto-second laser inscription enables the optical structures to be directly written in the three-dimensional space at a flexibly-chosen depth ranging from a few micrometres to hundreds micrometres, depending on the laser-focusing lens specifications, beneath the substrate surface [33]. Also, because the femto-second laser inscription has been considered a single-step process, the cost and the development difficulties are considered significantly lower compared to those of the conventional micro-fabrication techniques that have been already mentioned.

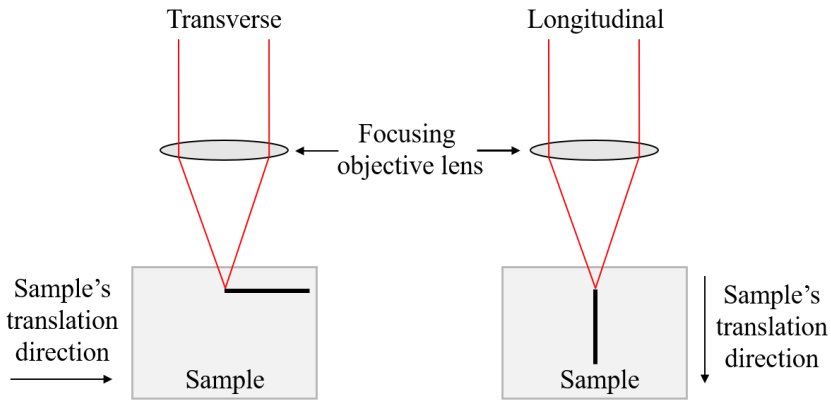

Figure 1.1 Schematic diagrams show (left) the transverse and (right) longitudinal writing geometries. It is assumed that the position of an objective lens is fixed, and only the translation of a sample occurs. The propagation direction of an inscribing laser is downward.

Since the interactions between the femto-second laser and the transparent materials are mainly occurred due to the nonlinear absorptions, the laser-modified volume is only restricted in a vicinity of the laser focal spot which usually has a few-micrometre size. By translating the

focused beam of femto-second pules over an inscribed medium via a system of computer-controlled stages, a region with the laser-modified physical properties can be precisely created along the beam's exposure paths. The relative directions of stage's translations can be either perpendicular (transverse writing geometry) or parallel (longitudinal writing geometry) to the propagation direction of an inscribing beam, as illustrated in Figure 1.1. Compared to the transverse writing, the longitudinal scanning typically benefits in the modified regions that have more cylindrical symmetry but can be written in a limited length which corresponds to the working distance of a focusing objective lens.

As shown in Figure 1.2, there are various structure configurations that have been so far suggested for the femto-second laser inscription of an optical waveguide. The differences between each type are not only the appearance of their cross-sectional arrangements, but also the physical mechanisms behind the structure's optical confinement that consequently result in the unique features of differing waveguide configurations. Note that the details of optical guiding characteristics of each waveguide geometry will be later discussed in the Section 1.1.4 and 1.1.5, where the literatures regarding the laser inscriptions of optical guiding structures will be reviewed. Based on these optical guiding mechanisms, the laser-inscribed waveguides can be roughly categorized into three groups: **1) positive-refractive-index induced waveguides** such as single-scan and multiple-scan types, **2) stress-field induced waveguides** such as dual track type, **3) depressed-cladding waveguides** such as single ring, double ring, and optical-lattice-like types. It is worth noting that the categorizations of optical waveguide types can be varied in different writing works depending on various manners, but typically they share similar criteria.

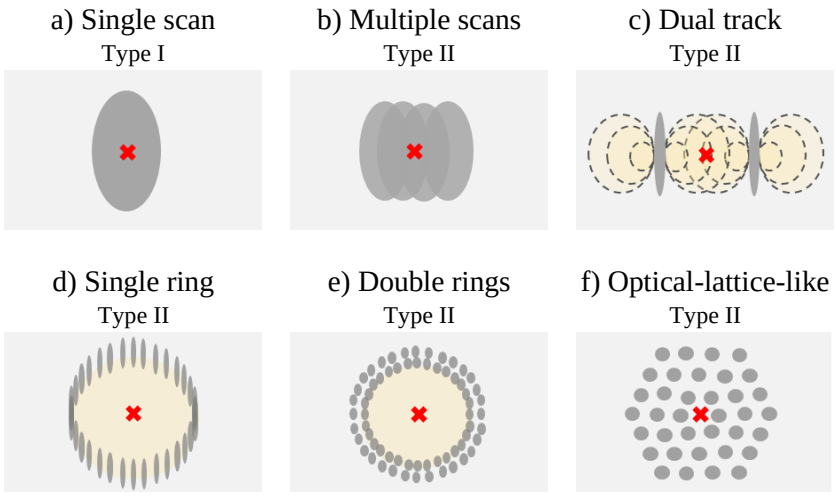

Figure 1.2 Schematic diagrams show the cross-sectional arrangements of laser-inscribed structures in various waveguide configurations. The darker areas represent the laser-modified regions, and the cross markers roughly indicate the areas of light confinement. Type I and II indicates the non-damaged and damaged modifications, respectively.

1.1.3 An introduction to femtosecond-laser/material interactions

Since the ultrafast-laser generation techniques such as the chirped pulse amplification (CPA) [34] were invented in the mid-1880s, the availability of shorter- and higher-peak-intensity pulse laser has pushed the new field of laser micromachining into the interests of many researchers. In 1994, the laser pulses of temporal width down to the regime of femtosecond (~150 fs) was firstly demonstrated to inscribe a damage feature in the fused silica [35]. Since then the researches in femtosecond laser micromachining have been widely extended into many applications including the fabrication of photonic devices [36]. Nowadays, it is well known that when the femtosecond laser which typically has the wavelength between the visible and near-infrared is focused inside a transparent dielectric, it rarely causes a valence electron to be linearly ionized. The processes of nonlinear excitation such as *nonlinear photoionization* and *avalanche ionization* must instead occur to initiate the mechanisms such as an optical breakdown that subsequently causes the localized modifications on a laser-exposed material [37]. The sub-sections below will describe about the mentioned nonlinear processes, and will also theoretically relate them to our experimental setup of a femtosecond-laser source.

1.1.3a Nonlinear photoionization

The light field with a photon energy ($h\upsilon$) less than the bandgap (E_g) of a material being illuminated may directly cause an electron from the valence band to be excited into the conduction band by means of two different nonlinear mechanisms which are the *multiphoton ionization* and *tunnelling ionization*. The conceptual diagrams of these two nonlinear phenomena can be seen in Figure 1.3. In general, the multiphoton absorption can occur if the number of photons m are simultaneously absorbed by a valence electron satisfying the condition of $mh\upsilon > E_g$. This multiphoton ionization can become dominant if the intensity of light field which is the number of photons per a unit area is low, and the frequency which is proportional to the photon energy is high but still lower than the requirement of a linear absorption. However, when the light field intensity is high enough (even if with low frequency) the potential barrier between the valence and conduction band can be distorted such that the electron excitations can occur through the effect of quantum tunnelling. In this regime, the tunnelling ionization becomes dominant. One may justify the transition between these two different mechanisms of nonlinear photoionization by using a formula known as the Keldysh parameter γ_K [37], [38] which is expressed by

$$\gamma_K = \frac{2\pi\upsilon}{e}\sqrt{\frac{m_e c n \epsilon_0 E_g}{I}} \tag{1.1}$$

where υ is the laser frequency, e is the electron charge, m_e is the reduced electron mass, c is the light speed, n is the material's refractive index, ϵ_0 is the free-space permittivity, E_g is the energy

bandgap, and I is the laser intensity. If $\gamma_K \gg 1$ the multiphoton ionization dominates the nonlinear ionization process, but if $\gamma_K \ll 1$ the tunnelling ionization instead becomes dominant.

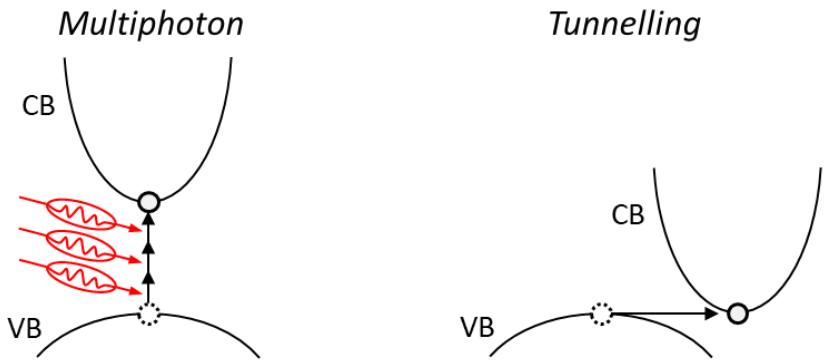

Figure 1.3 Schematic diagrams of nonlinear ionization processes, which are the multiphoton absorption (left) and the tunnelling excitation (right). The symbols VB and CB refer to the valence band and the conduction band, respectively.

One may find a calculation example of Equation 3.1 in [37], where the parameters for the femtosecond laser systems of 110 fs pulse-width, and 400 nm and 800 nm wavelengths were substituted into the formula. The literature showed that the calculated values of γ_K for differing well-known dielectrics including SF1, fused silica, and CaF_2 were in a range between 1 and 3, which could be interpreted that the optical breakdown mechanisms occurred in this condition of femtosecond-laser pulses were through the combination of multiphoton and tunnelling ionization mechanisms. For our experiment, the calculation by Equation 1.1 is plotted in Figure 1.4 using the laser frequency (υ) of $3.7948 \times 10^{14}\ s^{-1}$ ($\lambda = 790$ nm), the lithium niobate bandgap (E_g) of 4.9 eV [39], and the birefringent refractive indices of lithium niobate are $n_o = 2.2566$ and -

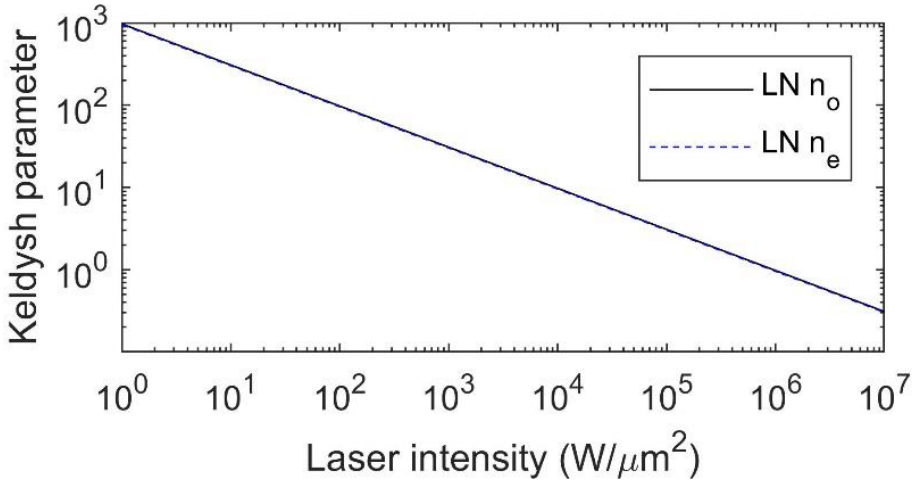

Figure 1.4 Plot of the Keldysh parameter versus the laser intensity, which was calculated from Eq 1.1 and was used the laser frequency of $\upsilon = 3.7948 \times 10^{14}\ s^{-1}$ ($\lambda = 790$ nm), the lithium niobate bandgap of $E_g = 4.9$ eV [39], and the birefringent refractive indices of lithium niobate are $n_o = 2.2566$ and $n_e = 2.1766$.

$n_e = 2.1766$. Once the optical breakdown intensity threshold of the material is known, the value of parameter γ_K can be straightforwardly determined from the plot in Figure 1.4.

1.1.3b Avalanche ionization

When an electron in the conduction band linearly absorbs photons and has the excess energy that is greater than the bandgap energy, it can cause the impact ionization onto a valence electron which can subsequently become a 'seed' for another excitation processes. The conceptual diagram of this impact ionization can be seen in Figure 1.5. Furthermore, if the light field keeps applying, the process can be repeated resulting in the generation of the excited electrons avalanche. Once the number of free electrons leads the critical density, the frequency of electron plasma becomes the frequency of the light field – which contributes to the strong absorption of photon energy and, consequently, the optical breakdown in the materials [36], [40]. Note that, apart from the mentioned process, the sources of an electron seed that initiates the avalanche ionization can present by other means such as lattice defects, thermal excitation, and the nonlinear photoionization processes which were previously described in the Section 1.1.3a.

It has been known that for the laser-matter interactions due to femtosecond laser pulses, both optical absorption mechanisms of nonlinear photoionization and avalanche ionization typically occur and cause the formation of free electron plasma [41]. However, the phenomena that take place after the energy from the excited electrons have released to the material lattice and subsequently generate the refractive index modifications have not been clearly understood. Since the avalanche ionization requires the electron seeds, it can be considered as the secondary process that could be occurred after the free electrons had been sufficiently energised by the processes like the nonlinear absorptions. In addition, some studies suggested that at high irradiances of femtosecond pulses the avalanche ionization could be the dominant mechanism, which was responsible for the dielectric breakdown and the strong structure damages, rather than the nonlinear photoionization [42], [43].

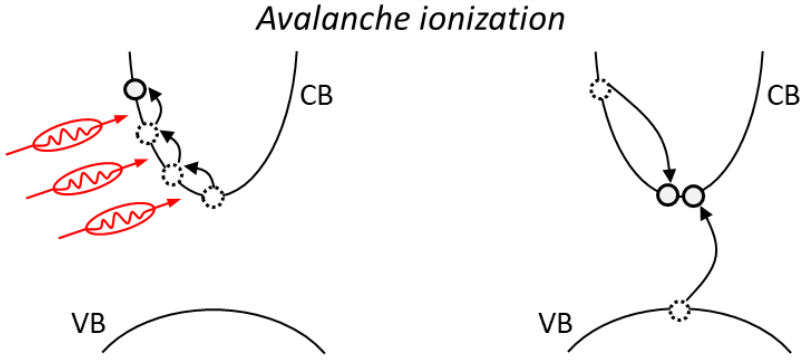

Figure 1.5 Schematic diagrams of the avalanche ionization process. The symbols VB and CB refer to the valence band and the conduction band, respectively.

1.1.4 Femtosecond-laser inscribed waveguides on lithium niobate

1.1.4a Positive-refractive-index induced waveguides

The sign of refractive index modification, which can be either a negative sign for the refractive index decrease or a positive sign for the refractive index increase, generated by the femtosecond-laser inscription processes depend on several factors which are relevant to both the properties of an inscribing laser and the physical nature of an inscribed medium. For a lithium niobate crystal, it has been known that the positive change in refractive index usually occurs if the amount of inscribing pulse energy is not exceeded the threshold of a material's optical breakdown [44]. In this regime, the material modification induced by the laser pulses is normally found non-damaged and thermally reversible. The positive change in an refractive index is presumably stemmed from the densification of the material lattice, the photo-refractivity and so on [45]. This kind of material change is typically called the **'Type I'** modification. The term has been generally used in the literatures for separating this modification type from the another type, the **'Type II',** that consists of the structural damages which is originated from an optical breakdown on an inscribed material [46], [47].

In 2004, Gui *et al* [48] demonstrated the use of a low-repetition-rate pulse laser to make the Y-splitters and waveguides that consisted of single-scan Type-I tracks in lithium niobate. The propagation loss of 1 dB/cm at 633 nm wavelength, and the positive refractive-index change of approximately 0.0006 were reported. Two years afterwards, Thomson *et al* [44] reported on the transition between the Type-I and -II modifications in lithium niobate by varying the pulse energy of the femto-second laser. Their Type-I single-track waveguides showed the light confinement of both perpendicular polarisation states at 650 nm wavelength, but, with a higher propagation loss of 9 dB/cm. Note that Thomson also mentioned about the thermal instability of their Type-I waveguides i.e. the light confinement at the 1550 nm wavelength was found temporary.

In 2006, Nejadmalayeri *et al* [45] showed that the uses of a relatively long pulse duration of 1 ps and a circularly-polarised state could be the fabrication keys for writing a structure with the higher thermal stability. By optimizing the pulse energy and the writing speed, Nejadmalayeri demonstrated the Type-I waveguides with the minimum losses in TE mode of 0.7 dB/cm and 1.0 dB/cm at the wavelength of 1330 nm and 1550 nm, respectively. Although the waveguides were found stable at the room-temperature, they did not survive after a thermal treatment at a temperature of 450 K. One year later, the same research group [49] claimed the first implementation of a high-repetition-rate laser for writing a Type-I waveguide on a lithium niobate sample by using the femtosecond laser with an adjustable repetition rate ranging from 100 kHz to 1.5 MHz. For their system, they found that the heat-accumulative modification regime was occurred when the repetition rate was equal or greater than 250 kHz. In addition, Nejadmalayeri

stated that in this laser-inscripiton regime the inscribed structures were found relatively smoother and, hence, resulted in a waveguide with the lower propagation loss of 0.6 dB/cm at a wavelength of 1300 nm when compared to that of a waveguide written in the regime of single-pulse interaction. They explained these observations by relating them to the effects of epitaxial regrowth and rapid thermal annealing, which typically happen when the laser pulses continuously interacted with the medium and produced the heats in the rate faster than the material's heat diffusion and cooling time [49].

Year [Ref]	**Type Sample**	R **[kHz]** τ **[fs]** λ_{fs} **[nm]**	Pol_{fs} E **[µJ]** s **[mm/s]**	D **[µm]** **NA** **OM**	α **[dB/cm]** λ_{gui} **[nm]** **(mode)**	β [% $\mathbf{W^{-1}cm^{-1}}$] λ_{SHG} **[nm]** **(mode)**
2004	Single scan	1	Circular	500	1.0	-
[48]	LN z-cut	150	10	0.4	633	
		775	0.05	20×	(-)	
2006	Single scan	5	Linear	250	9.0	-
[44]	LN z-cut	520	0.4	0.4	650	
		-	0.02	20×	(TE & TM)	
2006	Single scan	1	Circular	70	0.7	-
[45]	LN z-cut	1000	0.7	0.5	1300	
		800	0.9	-	(TE)	
			Circular		1.0	-
			0.7		1550	
			0.62		(TE)	
2006	Multi scans	1	-	20	2.25	0.006 [% W^{-1}]
[51]	PPLN z-cut	130	0.4	0.4	1550	782
		781	0.01	20×	(TM)	(TM)
2007	Single scan	**700**	Circular	110	0.6	-
[49]	LN z-cut	600	0.5	0.55	1300	
		1045	46	-	(TE)	
2007	Multi scans	**600**	Linear	150	0.6	-
[50]	LN z-cut	350	0.37	0.6	1550	
		1040	4	50×	(TM)	
2007	Multi scans	**600**	Linear	250	0.6	6.5
[52]	PPLN z-cut	350	0.37	0.6	1550	783
		1030	4	50×	(TM)	(TM)

Table 1.1 **$LiNbO_3$** - Summary of the literatures relating to the femtosecond-laser inscriptions of positive-refractive-index induced waveguides in lithium niobate. Symbol definitions: R (repetition rate), τ (pulse duration), λ_{fs} (femto-second laser wavelength), Pol_{fs} (femto-second laser polarisation), E (femto-second laser pulse energy), s (translation speed), D (inscription depth), NA (numerical aperture), OM (objective-lens magnification), α (propagation loss), λ_{gui} (guiding wavelength), β (SHG conversion efficiency) and λ_{SHG} (SHG wavelength).

Due to optical distortions, the single-scan waveguides fabricated by a transverse writing geometry usually suffer from the high asymmetry of waveguide cross-sections which result in many disadvantages such as the high coupling losses between the laser-written waveguides and an external optical fibre. The multi-scan fabrication, where a waveguide is produced by overlapping many inscribed structures of Type I, is one of the techniques introduced to overcome

this issue. In 2007, Bookey *et al* [50] applied the multi-scan technique to write a series of waveguides in a lithium niobate substrate and reported a minimum propagation loss of 0.6 dB/cm at a wavelength of 1550 nm. Their waveguide consisted of 20 single-scan tracks horizontally arranged with a separation of 0.4 μm resulting in a waveguide with the rectangular cross-sectional width of 8 μm. They claimed that due to the dimensional comparability with a standard single-mode fibre (Corning SMF-28), the low coupling loss of 1.1 dB/facet could be achieved. In addition, this multi-scan technique was demonstrated in [51] and [52] and succeeded in writing the optical guiding structures on in the samples of periodically-poled lithium niobate (PPLN), which partially preserved the second harmonic generation (SHG) properties. The summary of the literatures mentioned in this sub-section can be found in Table 4.1.

1.1.4b Stress-field induced waveguides

When a pair of the Type-II tracks were adjacently positioned like in Figure 1.2c, there could be an area that exhibits an increase of effective refractive index located in between the laser-written tracks. This refractive index increment has been presumably suggested by many literatures to stem from the effects of a stress field which is locally induced by the nearby material deformations [47]. In addition, the refractive index depression in the areas of the Type-II tracks also strengthens the beam confinement along the lateral directions in the area of refractive index increase. Compared to the Type-I waveguides mentioned in the Section 1.1.4a, this kind of dual-track waveguide had been demonstrated to provide the better thermal stability and more preservations of the material's intrinsic properties such as the second harmonic generation (SHG) [47], [53], [54] and electro-optic (EO) [55] in a core area that supports the light propagation.

In 2007, Burghoff *et al* [47] demonstrated the Type-II dual-track waveguide in a *x*-cut lithium niobate which could performed an optical guiding at a wavelength of 1064 nm in TM-mode with a propagation loss of 2.4 dB/cm, and was observed to remain after a thermal treatment at a temperature of 150 ^{o}C for 90 minute. They also showed that the waveguide could generate the frequency-doubling beam that propagated in the TE-mode with a conversion efficiency (β) of 0.6 % $W^{-1}cm^{-1}$ by the birefringent phase-matching technique. Several studies had also reported on the fabrication of waveguides for the quasi-phase-matching SHG in a PPLN host [53], [54] leading to the improvement of SHG conversion efficiency. In 2008, Liao *et al* [55] applied this dual-track configuration for the fabrication of a Mach-Zehnder modulator that could operate at a wavelength of 633 nm with an extinction ratio of 9.2 dB under the DC applied voltage difference of 19 V. It is worth mentioning that the waveguides of this type (fabricated in a lithium niobate medium) have been reported to confine the light only in the TM mode, where the light polarisation direction is parallel to the crystal's principle axis or the z-axis of a lithium niobate crystal. The summary of the literatures mentioned in this sub-section can be found in Table 1.2.

Year [Ref]	Type Sample SP [µm]	R [kHz] τ [fs] λ_{fs} [nm]	Pol_{fs} E [µJ] s [mm/s]	D [µm] NA OM	α [dB/cm] (mode) λ_{gui} [nm]	β [% $W^{-1}cm^{-1}$] (mode) λ_{SHG} [nm]
2007 [47]	Dual tracks LN x-cut 17	1 40 800	Linear 18 -	200 0.65 40×	2.4 (TM) 1064	0.6 (TE) 532
2007 [53]	Dual tracks PPLN z-cut 16	1 2500 800	Circular 0.4 0.8	50 0.65 40×	1.2 (TM) 1064	2.5 (TM) 532
2008 [55]	Dual tracks LN x-cut 8	1 40 800	Linear 0.09 0.02	20 0.9 100×	1 (TM) 633	-
2010 [54]	Dual tracks PPLN z-cut 10	1 50 800	Linear 10 0.4	200 0.4 25×	0.8 (TM) 1550	12.6 (TM) 774.6
2016 [56]	Dual tracks LN z-cut 15	1 120 795	Linear 2.1 0.02	75 0.4 20×	2.76 (TM) 632.8	-

Table 1.2 **$LiNbO_3$** - Summary of the literatures relating to the femtosecond-laser inscriptions of stress-field induced waveguides in lithium niobate. Symbol definitions: R (repetition rate), τ (pulse duration), λ_{fs} (femto-second laser wavelength), Pol_{fs} (femto-second laser polarisation), E (femto-second laser pulse energy), s (translation speed), D (inscription depth), NA (numerical aperture), OM (objective-lens magnification), α (propagation loss), λ_{gui} (guiding wavelength), β (SHG conversion efficiency) and λ_{SHG} (SHG wavelength).

1.1.4c Depressed-cladding waveguides

The studies on depressed-cladding waveguide fabrication by the femto-second laser direct writing have been considered less mature than that of the other waveguide types which were previously discussed in the Section 1.1.4a and 1.1.4b. The geometry configuration of this depressed-cladding waveguide typically consists of a number of tracks with a decrease in refractive index (Type-II or damage tracks) arranged in a cladding region that surrounds an inner area of unmodified material, which subsequently becomes a waveguide's core. The tracks can be aligned in differing cross-sectional geometries such as single ring, dual ring, optical-lattice-like structures and so forth. Examples of these waveguide geometries can be found in Figure 1.2d – 1.2f. The parameters such as track separation, cladding's and core's sizes that define the waveguide geometry can be accordingly adjusted, which thus enable the electric field profile of a guided mode to be flexibly engineered for a particular application. In addition, because the waveguide's core region is unaffected by the laser, the material's intrinsic properties of a host substrate can be fully preserved. Also, the optical guiding of this waveguide type fabricated on a lithium niobate wafer had been found to be less polarisation-dependent, when compared to the other types.

In 2013, He *et al* [57] reported on the fabrication of single-ring depressed-cladding waveguides that showed the low optical losses of ≈ 0.5 dB/cm at a wavelength of 1064 nm for

both perpendicular polarisations after a thermal annealing. However, due to the large core's diameter size of 50 µm, the multi-mode propagations were mainly excited in such structures. Krosen *et al* [58] demonstrated the integration of a single-ring waveguide with the laser-written Type-I Bragg grating and the electrodes that allowed the maximum reflected spectral shift (TM polarisation, centre wavelength of 1526 nm) of ±590 pm when a DC voltage of ±840 V was applied. In the paper [59], the same research group also reported on the integration of the waveguide and a multi-scan grating pattern inscribed in the waveguide core for the second harmonic generation. The normalized conversion efficiency of 0.0637 $\%W^{-1}$ cm^{-2} at a second harmonic wavelength of $\lambda_{SHG} = 532$ nm was achieved.

In 2017, Bhardwal *et al* [60] reported on the optimization of two fabrication parameters which were the stage's translation speed and the track's separations. Their results showed the low single-mode propagation losses of 0.56 dB/cm and 0.51 dB/cm at a wavelength of 1550 nm in the TE and TM polarisation modes, respectively. For the optical guidance at a mid-infrared spectrum, Nguyen *et al* [61] revealed that by using the waveguide cladding design of a double-ring arrangement the light at a wavelength of 3680 nm could be confined with the low attenuation losses of approximately 1.79 dB/cm for the TE and 1.25 dB/cm for the TM polarisation. They also showed that the heat treatments could be used to reduce the losses and to activate the single-mode excitation in the waveguide structures.

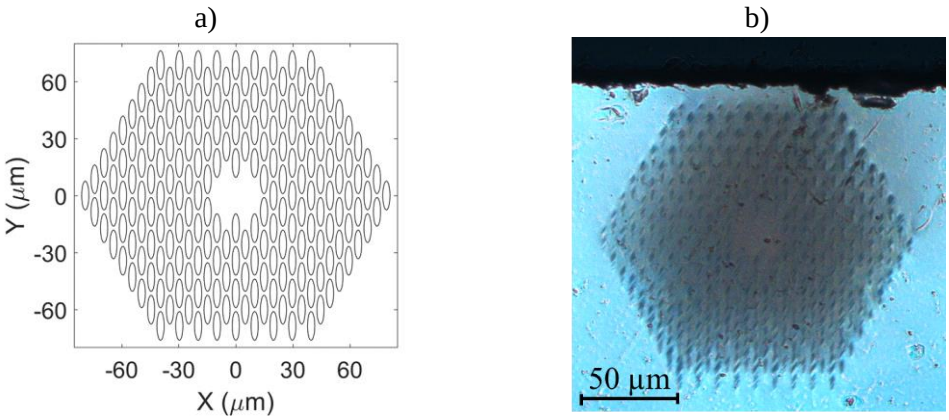

Figure 1.6 a) a schematic diagram of an optical-lattice-like waveguide geometry with 7 hexagonal layers of a cladding region. b) an example of waveguide cross-section fabricated in this study, which will be further discussed in the Chapter 5.

A waveguide geometry of optical-lattice-like, which consists of multiple damaged tracks arranged in a multi-layer hexagonal packing (as can be seen in Figure 1.6a), have been recently developed for the laser-inscriptions of an optical guiding structure. The track arrangements were usually designed to have an equal separation between adjacent tracks, and the positions of the most inner (hexagonal) layers were kept un-exposed by the laser pulses to create a region of light confinement or a waveguide's core. This type of waveguide's configuration had been found to benefit a large waveguide cladding region, but with the use of a smaller number of laser-inscribed

Year [Ref]	**Type Sample SP [µm] N_{tr} [track]**	**R [kHz] τ [fs] λ_{fs} [nm]**	**Pol_{fs} E [µJ] s [mm/s]**	**D [µm] NA MO**	**α [dB/cm] (mode) λ_{gui} [nm]**	**T_{anneal} [ºC] (time)**
2013 [57]	Single ring LN x-cut 3 -	1 120 800	Linear 5.04 0.5	150 0.4 20×	0.5* (TE & TM) 4000	260 (1 hour)
2014 [58]	Single ring LN x-cut 0.75 -	100 190 1028	Linear 0.065 8	100 0.8 100×	1.1 (TE) 3.0 (TM) 1064	-
2014 [65]	Double rings LN z-cut - -	**11000** 50 792	Linear 0.048 15	400 1.25 100×	3.0 (-) 600	-
2015 [59]	Single ring LN z-cut 2.5 40	1 120 800	Linear 0.15 0.08	100 0.8 100×	13.3 (TM) 532 8.33 (TM) 1064	-
2016 [56]	Single ring LN z-cut 3 -	1 120 795	Linear 2.1 0.5	75 0.4 20×	0.94 (TE) 2.57 (TM) 632.8	-
2016 [66]	Single ring LN z-cut 2 79	1 120 795	Linear 0.6 0.7	300 0.4 20×	2.9 (TE) 3683	-
2016 [64]	Opt.-lattice LN z-cut 10 84	1 120 795	Linear 2 0.75	180 0.65 40×	1.27 (TE) 1550	-
2017 [61]	Double ring LN z-cut 2 ~210	1 120 795	Linear 1.68 0.5	300 0.65 20×	1.79* (TE) 1.25* (TM) 3683	300 & 500 (3 hours each)
2017 [60]	Single ring LN x-cut 0.4 -	200 270 1030	- 0.3-0.4 5	- 0.45 20×	0.56 (TE) 0.51 (TM) 1550	-
2019 [67]	**Opt.-lattice LN z-cut 9.9 84**	**11000 66 790**	**Circular 0.054-0.064 10**	**~83 1.25 100×**	**0.4* (TE) 3.5* (TM) 1550**	**250 & 350 (3 hours each)**

Table 1.3 **$LiNbO_3$** - Summary of the literatures relating to the femtosecond-laser inscriptions of depressed-cladding waveguides in lithium niobate. Symbol definitions: SP (tracks separation), N_{tr} (number of track), R (repetition rate), τ (pulse duration), λ_{fs} (femto-second laser wavelength), Pol_{fs} (femto-second laser polarisation), E (femto-second laser pulse energy), s (translation speed), D (inscription depth), NA (numerical aperture), OM (objective-lens magnification), α (propagation loss), λ_{gui} (guiding wavelength), and T_{anneal} (annealing temperature). The symbol (*) indicates the propagation losses measured after the thermal annealing process.

tracks compared to the other packing geometries such as circular or rectangular track's arrangements. Recently, Karakuzu *et al* [62] showed in their numerical simulations that this packing geometry can possibly offer a low propagation loss over a wide range of wavelength, especially, in the near- to mid-infrared spectrum. They also reported that the simulation waveguides can be further improved in terms of light confinements by increasing the number of the hexagonal layer and/or by properly alternating the waveguide's cross-section via other track's disposition designs [63]. To the best of author's knowledge, there is only a few literatures that practically implemented this waveguide design for the femtosecond laser inscription technique. Prior to the publications of the works in this thesis, there was actually a study of LV *et al* [64] that demonstrated the use of an optical-lattice-like configuration for the laser-written structures of waveguides and power Y-splitters, which showed the optical guiding in TE-polarised propagation mode with a minimum attenuation loss of 1.27 dB/cm at a wavelength of 1550 nm. It is worth noting that there is not yet any report on the effects of photonic bandgap observed on the laser-inscribed waveguide, although the physical appearance of this optical-lattice-like structure highly resembles the cross-sectional arrangement of the photonic crystal fibres. The summary of the literatures mentioned in this sub-section can be found in Table 4.3.

1.1.5 Femtosecond-laser inscribed waveguides on other materials

To fulfil the completeness of literature review in this chapter, the present section will discuss about the femtosecond-laser inscription of optical waveguide structures on the other platforms of photonic material including silicon (Si), beta-barium borate (β-BaB_2O_4) and indium-phosphide (InP).

In a silicon (Si) platform, there are several studies that have been reported on the fabrications of optical waveguides using a tightly-focused pulse laser [68]–[72]. Due to the high Kerr nonlinear and plasma defocusing effects in silicon, a beam of high-peak-intensity was found strongly delocalized when it was focused deeply inside the Si substrate. This depth-dependent delocalization of pulse radiations results in the noticeable elongations and filamentations of the laser-induced structures. Also, the optical energy threshold required for a permanent laser-induced modification was reported to be significantly high compared to other dielectrics [73]. To date, the researchers addressed these issues by either writing a structure near the silicon's surface in a transverse writing geometry [68] or writing it in a longitudinal scanning geometry by using a long working distance objective lens [69]–[72]. The previous studies, see the list in Table 1.4, show that the waveguides of a single-scan type performed lossy guiding mainly stemmed from the optical scattering losses caused by the sub-micron photo-induced inhomogeneities [69]–[71]. It was hypothesised that these inhomogeneous features, observed on the waveguide structures, were originated from the formations of polycrystalline gains and amorphizations occurred when

the silicon crystal was exposed to the ultra-fast pulses and was resulted in the rapid melting and cooling processes [69]. Recently, Turnali *et al* [72] demonstrated that by using the circular depressed-cladding waveguide type where the light mainly propagated in an unmodified area a low propagation loss of approximately 2.2 dB/cm can be achieved at a wavelength of 1300 nm. It should be mentioned that the refractive index depression of $\approx 2\times10^{-4}$ generated by the femtosecond laser pulses with 150 kHz repetition rate and 1550 nm wavelength was reported in this mentioned literature [72].

Year [Ref]	**Type Sample Writing**	**R [kHz] τ [fs] λ_{fs} [nm]**	**Pol_{fs} E [µJ] s [mm/s]**	**D [µm] NA MO**	**α [dB/cm] (mode) λ_{gui} [nm]**	**T_{anneal} [ºC] (time)**
			Silicon (Si)			
2005 [68]	Single scan Silica-on Si Transverse	1 70 24000	Linear 1.7 0.033	90 - 130 0.5 40×	0.9 - 1.2 (⊥ to surface) 1320 0.7 - 0.8 (⊥ to surface) 1550	-
2016 [69]	Single scan c-Si Longitudinal	1 5×10^{6} 1550	Linear 0.7 – 2.4 50×10^{-6} – 2.5	1000 0.42 -	- - 1300	-
2017 [70]	Single scan c-Si Longitudinal	250 350 1500	Linear 2 0.03 – 0.1	- 0.5 -	- - 1500	-
2018 [71]	Single scan c-Si Longitudinal	400 800 1552	Linear 0.11 0.02	200 0.4 20×	4 – 6 - 1550	-
2019 [72]	Circular scan c-Si Mixing	150 5×10^{6} 1550	Linear 12.6 -	2900 0.25 -	2.2 - 1300	-
			Beta-barium borate (β-BaB_2O_4)			
2006 [74]	Ablated ridge β-BaB_2O_4 Transverse	0.962 176 775	Linear - 0.02	- - -	10* - 532	300 (8 hours)
2017 [22]	Single ring β-BaB_2O_4 Transverse	1 120 800	Linear 0.32 0.5	- 0.65 40	0.19 (TM) 800 2.80 multi-mode (TM) 400	-

Table 1.4 **Si and β-BaB_2O_4 -** Summary of the literatures relating to the femtosecond-laser inscriptions of optical waveguides in silicon and beta-barium borate. Symbol definitions: R (repetition rate), τ (pulse duration), λ_{fs} (femto-second laser wavelength), Pol_{fs} (femto-second laser polarisation), E (femto-second laser pulse energy), s (translation speed), D (inscription depth), NA (numerical aperture), OM (objective-lens magnification), α (propagation loss), λ_{gui} (guiding wavelength), and T_{anneal} (annealing temperature).

In a beta-barium borate (β-BaB_2O_4) platform, there is only a few studies of femtosecond-laser written waveguides that have been demonstrated so far. Degl'Innocenti *et al* [74] reported on the laser ablation of a ridge-type optical waveguide on β-BaB_2O_4. The post-possessing techniques of Ar^+ ion sputtering and thermal annealing were used for smoothening the ablated structure's sidewalls and reducing the residual defects, respectively. A propagation loss of 10 dB/cm at a wavelength of 532 nm was achieved in this study [74]. The same research group demonstrated the potential uses of this waveguide type for the second harmonic generation and the electro-optical amplitude modulation in the ultra-violet spectrum [17]. The laser micromachining of waveguides inside the wafer of beta-barium borate was recently realised by Li *et al* in [22] using a pulse laser with a wavelength of 800 nm and a repetition of 1 kHz. The single-ring depress-cladding waveguide type was implemented. A single-mode optical confinement with a low propagation loss of 0.19 dB/cm at a wavelength of 800 nm was reported. The optical guidance at a shorter wavelength of 400 nm showed a multi-mode excitation and a higher attenuation of 2.8 dB/cm [22]. It is worth noting that the guiding property is strongly polarisation-dependent, i.e. the waveguide only supported the TM-polarised mode, which was analogous to that of the same waveguide type fabricated in a lithium niobate substrate (see the Section 1.1.4c).

The research field of femtosecond-laser inscription for IP applications in the indium-phosphide (InP) is considered less mature than the other material platforms such as lithium niobite ($LiNbO_3$), silicon (Si) and beta-barium borate (β-BaB_2O_4). The fabrication of optical structures in this material mainly relies on the lithography-based techniques which have been intensively developed over decades [11]. To the best of author's knowledge, there is not yet any literature reporting on the direct-writing of optical waveguide in indium-phosphide by the ultrafast laser pulses. There are, however, a number of publications reported on the behaviors of this material upon the ultrafast laser-pulse irradiations [75]–[79]. The studies revealed the formations of polycrystalline and amorphous layers near the InP's surface when the incident pulse-energy density exceeded an optical breakdown threshold [75], [76]. Further increase of the pulse energy beyond the breakdown threshold resulted in the ablation of surface carters or grooves that had the dimensions and depths significantly relating to the pulse fluence and the relative direction of the laser-beam's polarization [80]. The formation of sub-wavelength periodic surface structures, presumably stemmed from the interference between the incident and surface-scattered laser beams, was also observed in indium-phosphide semiconductor [78].

In summary, this Section of 1.1 has reviewed the previous literatures that relate to the research study in this thesis. The reviewed topics include the material platforms for integrated photonics (IP), femtosecond-laser inscription of optical structures, an introduction of femtosecond-laser/material interactions, femtosecond-laser inscribed waveguides on lithium

niobate and other well-known materials. The review shows that although there are several literatures reported on the laser inscription of waveguide structures, it has been found that only a few of them utilizing the ultrafast pulses which interact with materials in a heat accumulative regime. Also, the optical-lattice-like geometry has been less used for fabricating the waveguides on this lithium niobate platform. The thermal annealing treatment at high temperatures are still unexplored regarding its impacts on an optical confinement at 1550 nm telecommunication wavelength on this particular type of the light guiding structures.

1.2 Aims and scopes of this study

The main goal of this study was to fabricate an optical waveguide that could be operated with a single-mode optical guiding and a low propagation loss at a telecommunication wavelength on a material host of lithium niobate crystal. A femtosecond-laser inscription by using the high-repetition rate pulses was chosen for our fabrication method. We had focused our studies on implementing the waveguide cross-sectional geometry of an optical-lattice-like packing, and investigating the optical guiding characteristics of our fabricated waveguides under a series of heat treatments up to very high temperatures. Plus, one of our aims was to apply the fabrication techniques of this optical waveguide for manufacturing the other types of optical devices such as the curvilinear guiding structures and the optical power splitters, which were also the important building blocks for the integrated photonics (IP) technology. The aims of this study can be roughly separated into three parts which had been mentioned in the following sentences.

Part 1.

To explore the influences of operational inscription parameters on the laser-written structures, and to investigate the most optimum range of such parameters for fabricating the waveguide structures with low optical propagation loss and fundamental-mode guiding.

Part 2.

To fabricate the optical waveguide structures and to optimize their optical guiding characteristics for the low-attenuation confinements at a spectral range of the near-infrared wavelength for the telecommunication and nonlinear optics applications. The characterization processes of the waveguides before and after a series of heat annealing treatments should be thoroughly performed to investigate the structure's thermal stability.

Part 3.

To numerically design and to fabricate the waveguide-based optical devices such as the curvilinear guiding structures and the optical power splitters which could be further adapted for the fabrications of more-complex optical structures. To demonstrate a structure integration of

multiple components which could potentially enhance the functionalities of a laser-inscribed optical structure.

1.3 Thesis structure

Chapter 2 will comprehensively explain the technical and experimental details of the works that had been done in this thesis. These topics will include the femtosecond-laser source and oscillator setups, the optical inspections of femtosecond-laser pulse, the controls and calibrations of the translation stages, the specifications of focusing objective lens, the sample alignment and positioning, the cutting and polishing processes, and the thermal annealing treatment. The chapter will also give a brief mathematic derivation of a calculation approach for the refractive index profile retrieval, which is called the Quantitative Phase Microscopy (QPM). Then, the processes of optical guiding characterization will be thoroughly explained along with a set of equations for an optical attenuation analysis and a list of all optical equipment and tools being used in this study.

Chapter 3 will present the experimental results of our study on the impacts of inscription parameters on the physical and optical properties of the laser-inscribed structures. These parameters include laser pulse energy, writing speed and direction, and laser focusing depth. This chapter will also discuss about the optical aberration effects such as a spherical aberration and a birefringent-induced astigmatism which can significantly cause the optical distortions on a beam focussing profile and, hence, can possibly result in an unsymmetrical and elongated photo-induced modification. A mathematical model, which was suggested by Török et al [81]–[83], based on a modified integral representation of light wave diffractions was implemented in our simulation studies. The numerical results will be presented and discussed together with the experiment data that had been observed from the parameter-controlled inscription tests. Finally, the influences of thermal annealing treatments at different temperatures ranging from 250 ^{o}C to 950 ^{o}C on the physical characteristics of laser-written structures will be revealed in this chapter.

Chapter 4 will present the cross-sectional arrangement of laser-inscribed damage tracks and the technical strategies for the fabrications of an optical-lattice-like waveguide on a lithium niobate substrate. The study on computer simulations in a Comsol Multi-physics software which were implemented to investigate a suitable range of a track separation, number of hexagonal ring and a size of waveguide core will be presented. Then, the experimental study of laser-inscription parameter optimizations which was aimed for fabricating a low-optical-loss guiding structure will be revealed. Also, the polarisation-dependent light guidance that have been typically observed in this type of waveguides will be analysed by means of two theoretical models, which were the anisotropic piezo-optic (APO) and the modal radiation leakage (MRL) effect. The last section of

this chapter will demonstrate the impacts of a series of thermal annealing treatments on the optical confinements of the fabricated waveguide structures.

Chapter 5 will demonstrate the applications of our waveguide fabrication techniques that had been developed and optimized in the Chapter 4 for the femtosecond-laser writing of optical structures with more structural complexities. The impacts of an increasing number of hexagonal lattice layers, from 4 to 7 layers, were tested on the variation of optical guiding characteristics on the straight and curvilinear waveguides. The optical attenuations stemmed from the waveguide's curvature were calculated and, subsequently, plotted as a function of the bending radius. This chapter will also report on the laser inscriptions of optical power splitters with 2 and 3 output-branches. The light splitting mechanism was based on the multi-mode interference, which had revealed the relatively low attenuation losses compared to the traditional splitter configurations. Then, an inscribed structure of optical splitter with an extended output separation up to ≈ 293.7 μm that could operate at a telecommunication wavelength with low attenuations and balanced splitting ratios will be presented in the last section of this chapter.

Chapter 6 contains the conclusion parts of this thesis and the author's perspectives on the potential works that could be possibly done to develop and enhance the experimental outcomes of this and other relevant studies. Also, the sources of author's publications and international presentations that are related to this thesis will be mentioned in this chapter.

References

[1] S. E. Miller, "Integrated optics: An introduction," *The Bell System Technical Journal*, vol. 48, no. 7, pp. 2059–2069, Sep. 1969, doi: 10.1002/j.1538-7305.1969.tb01165.x.

[2] Y. Hu *et al.*, "III/V-on-Si MQW lasers by using a novel photonic integration method of regrowth on a bonding template," *Light Sci Appl*, vol. 8, no. 1, pp. 1–9, Oct. 2019, doi: 10.1038/s41377-019-0202-6.

[3] B. Szelag *et al.*, "Hybrid III–V/Silicon Technology for Laser Integration on a 200-mm Fully CMOS-Compatible Silicon Photonics Platform," *IEEE Journal of Selected Topics in Quantum Electronics*, vol. 25, no. 5, pp. 1–10, Sep. 2019, doi: 10.1109/JSTQE.2019.2904445.

[4] J. Cui and Z. Zhou, "High-performance Ge-on-Si photodetector with optimized DBR location," *Opt. Lett., OL*, vol. 42, no. 24, pp. 5141–5144, Dec. 2017, doi: 10.1364/OL.42.005141.

[5] S. Liao *et al.*, "36 GHz submicron silicon waveguide germanium photodetector," *Opt. Express, OE*, vol. 19, no. 11, pp. 10967–10972, May 2011, doi: 10.1364/OE.19.010967.

[6] A. Rao *et al.*, “Highly Efficient Nonlinear Integrated Photonics in Ultracompact Periodically-Poled Lithium Niobate on Silicon,” in *Frontiers in Optics / Laser Science (2018), paper JTu3A.59*, 2018, p. JTu3A.59, doi: 10.1364/FIO.2018.JTu3A.59.

[7] A. Rao and S. Fathpour, “Compact Lithium Niobate Electrooptic Modulators,” *IEEE Journal of Selected Topics in Quantum Electronics*, vol. 24, no. 4, pp. 1–14, Jul. 2018, doi: 10.1109/JSTQE.2017.2779869.

[8] F. Lemaitre *et al.*, “Foundry Photonic Process Extension With Bandgap Tuning Using Selective Area Growth,” *IEEE Journal of Selected Topics in Quantum Electronics*, vol. 25, no. 5, pp. 1–8, Sep. 2019, doi: 10.1109/JSTQE.2019.2922069.

[9] R. Toufanian, A. Piryatinski, A. H. Mahler, R. Iyer, J. A. Hollingsworth, and A. M. Dennis, “Bandgap Engineering of Indium Phosphide-Based Core/Shell Heterostructures Through Shell Composition and Thickness,” *Front. Chem.*, vol. 6, 2018, doi: 10.3389/fchem.2018.00567.

[10] M. Smit, K. Williams, and J. van der Tol, “Past, present, and future of InP-based photonic integration,” *APL Photonics*, vol. 4, no. 5, p. 050901, May 2019, doi: 10.1063/1.5087862.

[11] M. Smit *et al.*, “An introduction to InP-based generic integration technology,” *Semicond. Sci. Technol.*, vol. 29, no. 8, p. 083001, Jun. 2014, doi: 10.1088/0268-1242/29/8/083001.

[12] J. Summers *et al.*, “Monolithic inp-based coherent transmitter photonic integrated circuit with 2.25 Tbit/s capacity,” *Electronics Letters*, vol. 50, no. 16, pp. 1150–1152, Jul. 2014, doi: 10.1049/el.2014.2011.

[13] L. P. Gonzalez, J. M. Murray, S. Krishnamurthy, and S. Guha, “Wavelength dependence of two photon and free carrier absorptions in InP,” *Opt. Express, OE*, vol. 17, no. 11, pp. 8741–8748, May 2009, doi: 10.1364/OE.17.008741.

[14] A. Villar, A. Lohrmann, and A. Ling, “Experimental entangled photon pair generation using crystals with parallel optical axes,” *Opt. Express, OE*, vol. 26, no. 10, pp. 12396–12402, May 2018, doi: 10.1364/OE.26.012396.

[15] D. A. Valverde-Chávez and D. G. Cooke, “Multi-Cycle Terahertz Emission from β-Barium Borate,” *J Infrared Milli Terahz Waves*, vol. 38, no. 1, pp. 96–103, Jan. 2017, doi: 10.1007/s10762-016-0335-0.

[16] A. Nautiyal and P. B. Bisht, “Broadly tunable parametric line emission from β-barium borate on pumping with picosecond pulses,” *Optics Communications*, vol. 281, no. 12, pp. 3351–3355, Jun. 2008, doi: 10.1016/j.optcom.2008.02.054.

[17] G. Poberaj, R. Degl’Innocenti, C. Medrano, and P. Günter, “UV integrated optics devices based on beta-barium borate,” *Optical Materials*, vol. 31, no. 7, pp. 1049–1053, May 2009, doi: 10.1016/j.optmat.2007.12.020.

[18] T. Liu, P. Liu, L. Zhang, Y.-F. Zhou, X.-F. Yu, and X.-L. Wang, "Planar waveguide in beta barium borate formed by proton implantation and optical properties in visible and near-infrared band," *Optical Materials*, vol. 35, no. 12, pp. 2068–2071, Oct. 2013, doi: 10.1016/j.optmat.2013.05.021.

[19] A. Boudrioua, P. Moretti, J. C. Loulergue, and K. Polgar, "Helium ion-implanted planar waveguide in Y-cut and Z-cut β-BBO (BaB2O4)," *Optical Materials*, vol. 14, no. 1, pp. 31–39, Mar. 2000, doi: 10.1016/S0925-3467(99)00101-9.

[20] R. Degl'Innocenti, A. Guarino, G. Poberaj, and P. Günter, "Second harmonic generation of continuous wave ultraviolet light and production of β-BaB2O4 optical waveguides," *Appl. Phys. Lett.*, vol. 89, no. 4, p. 041103, Jul. 2006, doi: 10.1063/1.2234275.

[21] G. Qu, Z. Hu, Y. Wang, Q. Yang, and L. Tong, "Synthesis of Optical-Quality Single-Crystal β-BaB2O4 Microwires and Nanowires," *Advanced Functional Materials*, vol. 23, no. 10, pp. 1232–1237, 2013, doi: 10.1002/adfm.201201866.

[22] Z. Li, C. Cheng, C. Romero, Q. Lu, J. R. Vázquez de Aldana, and F. Chen, "Low-loss optical waveguides in β-BBO crystal fabricated by femtosecond-laser writing," *Optical Materials*, vol. 73, pp. 45–49, Nov. 2017, doi: 10.1016/j.optmat.2017.07.049.

[23] N. Dong, F. Chen, and J. R. V. de Aldana, "Efficient second harmonic generation by birefringent phase matching in femtosecond-laser-inscribed KTP cladding waveguides," *physica status solidi (RRL) – Rapid Research Letters*, vol. 6, no. 7, pp. 306–308, 2012, doi: 10.1002/pssr.201206224.

[24] C. Wang, M. Zhang, B. Stern, M. Lipson, and M. Lončar, "Nanophotonic lithium niobate electro-optic modulators," *Opt. Express, OE*, vol. 26, no. 2, pp. 1547–1555, Jan. 2018, doi: 10.1364/OE.26.001547.

[25] R. Luo, H. Jiang, S. Rogers, H. Liang, Y. He, and Q. Lin, "On-chip second-harmonic generation and broadband parametric down-conversion in a lithium niobate microresonator," *Opt. Express, OE*, vol. 25, no. 20, pp. 24531–24539, Oct. 2017, doi: 10.1364/OE.25.024531.

[26] L. Arizmendi, "Photonic applications of lithium niobate crystals," *physica status solidi (a)*, vol. 201, no. 2, pp. 253–283, 2004, doi: 10.1002/pssa.200303911.

[27] I. Baumann *et al.*, "Erbium incorporation in LiNbO3 by diffusion-doping," *Appl Phys A*, vol. 64, no. 1, pp. 33–44, Dec. 1996, doi: 10.1007/s003390050441.

[28] W. Sohler, B. K. Das, D. Dey, S. Reza, H. Suche, and R. Ricken, "Erbium-Doped Lithium Niobate Waveguide Lasers," *IEICE TRANSACTIONS on Electronics*, vol. E88-C, no. 5, pp. 990–997, May 2005.

[29] G. E. Peterson, A. M. Glass, and T. J. Negran, "Control of the Susceptibility of Lithium Niobate to Laser-Induced Refractive Index Changes," *Appl. Phys. Lett.*, vol. 19, no. 5, pp. 130–132, Sep. 1971, doi: 10.1063/1.1653854.

[30] J. Frangen, H. Herrmann, R. Ricken, H. Seibert, W. Sohler, and E. Strake, “Integrated optical, acoustically tunable wavelength filter,” *Electronics Letters*, vol. 25, no. 23, pp. 1583–1584, Nov. 1989, doi: 10.1049/el:19891063.

[31] Y. Furukawa, K. Kitamura, S. Takekawa, A. Miyamoto, M. Terao, and N. Suda, “Photorefraction in LiNbO3 as a function of [Li]/[Nb] and MgO concentrations,” *Appl. Phys. Lett.*, vol. 77, no. 16, pp. 2494–2496, Oct. 2000, doi: 10.1063/1.1318721.

[32] Z. Su, Q. Meng, and B. Zhang, “Analysis on the damage threshold of MgO:LiNbO3 crystals under multiple femtosecond laser pulses,” *Optical Materials*, vol. 60, pp. 443–449, Oct. 2016, doi: 10.1016/j.optmat.2016.08.036.

[33] S. Gross and M. J. Withford, “Ultrafast-laser-inscribed 3D integrated photonics: challenges and emerging applications,” *Nanophotonics*, vol. 4, no. 3, pp. 332–352, 2015, doi: 10.1515/nanoph-2015-0020.

[34] D. Strickland and G. Mourou, “Compression of amplified chirped optical pulses,” *Optics Communications*, vol. 56, no. 3, pp. 219–221, Dec. 1985, doi: 10.1016/0030-4018(85)90120-8.

[35] D. Du, X. Liu, G. Korn, J. Squier, and G. Mourou, “Laser-induced breakdown by impact ionization in SiO_2 with pulse widths from 7 ns to 150 fs,” *Appl. Phys. Lett.*, vol. 64, no. 23, pp. 3071–3073, Jun. 1994, doi: 10.1063/1.111350.

[36] R. Osellame, G. Cerullo, and R. Ramponi, *Femtosecond Laser Micromachining Photonic and Microfluidic Devices in Transparent Materials*, vol. 123. Springer, 2011.

[37] C. B. Schaffer, A. Brodeur, and E. Mazur, “Laser-induced breakdown and damage in bulk transparent materials induced by tightly focused femtosecond laser pulses,” *Meas. Sci. Technol.*, vol. 12, no. 11, pp. 1784–1794, Oct. 2001, doi: 10.1088/0957-0233/12/11/305.

[38] L. V. Keldysh, “Ionization in the Field of a Strong Electromagnetic Wave.pdf,” *Soviet Physics Jetp*, vol. 20, no. 5, p. 1307, 1965.

[39] S. Mamoun, A. E. Merad, and L. Guilbert, “Energy band gap and optical properties of lithium niobate from ab initio calculations,” *Computational Materials Science*, vol. 79, pp. 125–131, Nov. 2013, doi: 10.1016/j.commatsci.2013.06.017.

[40] B. C. Stuart, M. D. Feit, S. Herman, A. M. Rubenchik, B. W. Shore, and M. D. Perry, “Nanosecond-to-femtosecond laser-induced breakdown in dielectrics,” *Phys. Rev. B*, vol. 53, no. 4, pp. 1749–1761, Jan. 1996, doi: 10.1103/PhysRevB.53.1749.

[41] S. J. Mihailov, “6 - Femtosecond Laser-Inscribed Fiber Bragg Gratings for Sensing Applications,” in *Opto-Mechanical Fiber Optic Sensors*, H. Alemohammad, Ed. Butterworth-Heinemann, 2018, pp. 137–174.

[42] C. N. LaFratta and L. Li, “Chapter 9 - Making Two-Photon Polymerization Faster,” in *Three-Dimensional Microfabrication Using Two-photon Polymerization*, T. Baldacchini, Ed. Oxford: William Andrew Publishing, 2016, pp. 221–241.

[43] I. Mingareev, L. Shah, M. Richardson, and M. Ramme, “Chapter 18 - Direct Infrared Laser Machining of Semiconductors for Electronics Applications,” in *Advances in Laser Materials Processing (Second Edition)*, J. Lawrence, Ed. Woodhead Publishing, 2018, pp. 541–570.

[44] R. R. Thomson, S. Campbell, I. J. Blewett, A. K. Kar, and D. T. Reid, “Optical waveguide fabrication in z-cut lithium niobate ($LiNbO_3$) using femtosecond pulses in the low repetition rate regime,” *Appl. Phys. Lett.*, vol. 88, no. 11, p. 111109, Mar. 2006, doi: 10.1063/1.2186389.

[45] A. H. Nejadmalayeri and P. R. Herman, “Ultrafast laser waveguide writing: lithium niobate and the role of circular polarization and picosecond pulse width,” *Opt. Lett., OL*, vol. 31, no. 20, pp. 2987–2989, Oct. 2006, doi: 10.1364/OL.31.002987.

[46] S. Gross, M. Dubov, and M. J. Withford, “On the use of the Type I and II scheme for classifying ultrafast laser direct-write photonics,” *Opt. Express, OE*, vol. 23, no. 6, pp. 7767–7770, Mar. 2015, doi: 10.1364/OE.23.007767.

[47] J. Burghoff, C. Grebing, S. Nolte, and A. Tünnermann, “Waveguides in lithium niobate fabricated by focused ultrashort laser pulses,” *Applied Surface Science*, vol. 253, no. 19, pp. 7899–7902, Jul. 2007, doi: 10.1016/j.apsusc.2007.02.148.

[48] Li Gui, Baoxi Xu, and Tow Chong Chong, “Microstructure in lithium niobate by use of focused femtosecond laser pulses,” *IEEE Photonics Technology Letters*, vol. 16, no. 5, pp. 1337–1339, May 2004, doi: 10.1109/LPT.2004.826112.

[49] A. H. Nejadmalayeri and P. R. Herman, “Rapid thermal annealing in high repetition rate ultrafast laser waveguide writing in lithium niobate,” *Opt. Express, OE*, vol. 15, no. 17, pp. 10842–10854, Aug. 2007, doi: 10.1364/OE.15.010842.

[50] H. T. Bookey *et al.*, “Femtosecond Laser Inscription of Low Insertion Loss Waveguides in Z-Cut Lithium Niobate,” *IEEE Photonics Technology Letters*, vol. 19, no. 12, pp. 892–894, Jun. 2007, doi: 10.1109/LPT.2007.897534.

[51] Y. L. Lee *et al.*, “Second-harmonic generation in periodically poled lithium niobate waveguides fabricated by femtosecond laser pulses,” *Appl. Phys. Lett.*, vol. 89, no. 17, p. 171103, Oct. 2006, doi: 10.1063/1.2364832.

[52] R. Osellame *et al.*, “Femtosecond laser writing of waveguides in periodically poled lithium niobate preserving the nonlinear coefficient,” *Appl. Phys. Lett.*, vol. 90, no. 24, p. 241107, Jun. 2007, doi: 10.1063/1.2748328.

[53] J. Thomas, M. Heinrich, J. Burghoff, S. Nolte, A. Ancona, and A. Tünnermann, "Femtosecond laser-written quasi-phase-matched waveguides in lithium niobate," *Appl. Phys. Lett.*, vol. 91, no. 15, p. 151108, Oct. 2007, doi: 10.1063/1.2799178.

[54] Z. Huang *et al.*, "Femtosecond second-harmonic generation in periodically poled lithium niobate waveguides written by femtosecond laser pulses," *Opt. Lett., OL*, vol. 35, no. 6, pp. 877–879, Mar. 2010, doi: 10.1364/OL.35.000877.

[55] Y. Liao *et al.*, "Electro-optic integration of embedded electrodes and waveguides in $LiNbO_3$ using a femtosecond laser," *Opt. Lett., OL*, vol. 33, no. 19, pp. 2281–2283, Oct. 2008, doi: 10.1364/OL.33.002281.

[56] J. Lv, Y. Cheng, Q. Lu, J. R. Vázquez de Aldana, X. Hao, and F. Chen, "Femtosecond laser written optical waveguides in z-cut MgO:$LiNbO_3$ crystal: Fabrication and optical damage investigation," *Optical Materials*, vol. 57, pp. 169–173, Jul. 2016, doi: 10.1016/j.optmat.2016.05.003.

[57] R. He, Q. An, Y. Jia, G. R. Castillo-Vega, J. R. V. de Aldana, and F. Chen, "Femtosecond laser micromachining of lithium niobate depressed cladding waveguides," *Opt. Mater. Express, OME*, vol. 3, no. 9, pp. 1378–1384, Sep. 2013, doi: 10.1364/OME.3.001378.

[58] S. Kroesen, W. Horn, J. Imbrock, and C. Denz, "Electro–optical tunable waveguide embedded multiscan Bragg gratings in lithium niobate by direct femtosecond laser writing," *Opt. Express, OE*, vol. 22, no. 19, pp. 23339–23348, Sep. 2014, doi: 10.1364/OE.22.023339.

[59] S. Kroesen, K. Tekce, J. Imbrock, and C. Denz, "Monolithic fabrication of quasi phase-matched waveguides by femtosecond laser structuring the $\chi_{(2)}$ nonlinearity," *Appl. Phys. Lett.*, vol. 107, no. 10, p. 101109, Sep. 2015, doi: 10.1063/1.4930834.

[60] S. Bhardwaj *et al.*, "Inscription of type I and depressed cladding waveguides in lithium niobate using a femtosecond laser," *Appl. Opt., AO*, vol. 56, no. 20, pp. 5692–5697, Jul. 2017, doi: 10.1364/AO.56.005692.

[61] H.-D. Nguyen *et al.*, "Low-loss 3D-laser-written mid-infrared $LiNbO_3$ depressed-index cladding waveguides for both TE and TM polarizations," *Opt. Express, OE*, vol. 25, no. 4, pp. 3722–3736, Feb. 2017, doi: 10.1364/OE.25.003722.

[62] H. Karakuzu, M. Dubov, and S. Boscolo, "Control of the properties of micro-structured waveguides in lithium niobate crystal," *Opt. Express, OE*, vol. 21, no. 14, pp. 17122–17130, Jul. 2013, doi: 10.1364/OE.21.017122.

[63] H. Karakuzu, M. Dubov, S. Boscolo, L. A. Melnikov, and Y. A. Mazhirina, "Optimisation of microstructured waveguides in z-cut $LiNbO_3$ crystals," *Opt. Mater. Express, OME*, vol. 4, no. 3, pp. 541–552, Mar. 2014, doi: 10.1364/OME.4.000541.

[64] J. Lv, Y. Cheng, J. R. V. de Aldana, X. Hao, and F. Chen, "Femtosecond Laser Writing of Optical-Lattice-Like Cladding Structures for Three-Dimensional Waveguide Beam Splitters

in $LiNbO_3$ Crystal," *Journal of Lightwave Technology*, vol. 34, no. 15, pp. 3587–3591, Aug. 2016, doi: 10.1109/JLT.2016.2573841.

[65] M. Dubov, S. Boscolo, and D. J. Webb, "Microstructured waveguides in z-cut $LiNbO_3$ by high-repetition rate direct femtosecond laser inscription," *Opt. Mater. Express, OME*, vol. 4, no. 8, pp. 1708–1716, Aug. 2014, doi: 10.1364/OME.4.001708.

[66] H.-D. Nguyen *et al.*, "Heuristic modelling of laser written mid-infrared $LiNbO_3$ stressed-cladding waveguides," *Opt. Express, OE*, vol. 24, no. 7, pp. 7777–7791, Apr. 2016, doi: 10.1364/OE.24.007777.

[67] T. Piromjitpong, M. Dubov, and S. Boscolo, "High-repetition-rate femtosecond-laser inscription of low-loss thermally stable waveguides in lithium niobate," *Appl. Phys. A*, vol. 125, no. 5, p. 302, Apr. 2019, doi: 10.1007/s00339-019-2609-6.

[68] A. H. Nejadmalayeri, P. R. Herman, J. Burghoff, M. Will, S. Nolte, and A. Tünnermann, "Inscription of optical waveguides in crystalline silicon by mid-infrared femtosecond laser pulses," *Opt. Lett., OL*, vol. 30, no. 9, pp. 964–966, May 2005, doi: 10.1364/OL.30.000964.

[69] M. Chambonneau, Q. Li, M. Chanal, N. Sanner, and D. Grojo, "Writing waveguides inside monolithic crystalline silicon with nanosecond laser pulses," *Opt. Lett., OL*, vol. 41, no. 21, pp. 4875–4878, Nov. 2016, doi: 10.1364/OL.41.004875.

[70] I. Pavlov *et al.*, "Femtosecond laser written waveguides deep inside silicon," *Opt. Lett., OL*, vol. 42, no. 15, pp. 3028–3031, Aug. 2017, doi: 10.1364/OL.42.003028.

[71] G. Matthäus, H. Kämmer, K. A. Lammers, C. Vetter, W. Watanabe, and S. Nolte, "Inscription of silicon waveguides using picosecond pulses," *Opt. Express, OE*, vol. 26, no. 18, pp. 24089–24097, Sep. 2018, doi: 10.1364/OE.26.024089.

[72] A. Turnali, M. Han, and O. Tokel, "Laser-written depressed-cladding waveguides deep inside bulk silicon," *J. Opt. Soc. Am. B, JOSAB*, vol. 36, no. 4, pp. 966–970, Apr. 2019, doi: 10.1364/JOSAB.36.000966.

[73] "OSA | Delocalization of femtosecond radiation in silicon." [Online]. Available: https://www.osapublishing.org/ol/abstract.cfm?uri=ol-37-16-3369. [Accessed: 20-Nov-2019].

[74] R. Degl'Innocenti, S. Reidt, A. Guarino, D. Rezzonico, G. Poberaj, and P. Günter, "Micromachining of ridge optical waveguides on top of He+-implanted β-BaB2O4 crystals by femtosecond laser ablation," *Journal of Applied Physics*, vol. 100, no. 11, p. 113121, Dec. 2006, doi: 10.1063/1.2396716.

[75] A. Borowiec, M. MacKenzie, G. C. Weatherly, and H. K. Haugen, "Femtosecond laser pulse ablation of GaAs and InP: studies utilizing scanning and transmission electron microscopy," *Appl Phys A*, vol. 77, no. 3, pp. 411–417, Aug. 2003, doi: 10.1007/s00339-002-1949-8.

[76] J. Bonse, S. M. Wiggins, and J. Solis, “Dynamics of femtosecond laser-induced melting and amorphization of indium phosphide,” *Journal of Applied Physics*, vol. 96, no. 4, pp. 2352–2358, Aug. 2004, doi: 10.1063/1.1771822.

[77] J. Bonse, S. M. Wiggins, and J. Solis, “Ultrafast phase transitions after femtosecond laser irradiation of indium phosphide,” *Journal of Applied Physics*, vol. 96, no. 5, pp. 2628–2631, Sep. 2004, doi: 10.1063/1.1776311.

[78] J. Bonse, M. Munz, and H. Sturm, “Structure formation on the surface of indium phosphide irradiated by femtosecond laser pulses,” *Journal of Applied Physics*, vol. 97, no. 1, p. 013538, Dec. 2004, doi: 10.1063/1.1827919.

[79] J. Bonse *et al.*, “Ablation and structural changes induced in InP surfaces by single 10 fs laser pulses in air,” *Journal of Applied Physics*, vol. 106, no. 7, p. 074907, Oct. 2009, doi: 10.1063/1.3236630.

[80] A. Borowiec and H. K. Haugen, “Femtosecond laser micromachining of grooves in indium phosphide,” *Appl. Phys. A*, vol. 79, no. 3, pp. 521–529, Aug. 2004, doi: 10.1007/s00339-003-2377-0.

[81] P. Török, P. Varga, Z. Laczik, and G. R. Booker, “Electromagnetic diffraction of light focused through a planar interface between materials of mismatched refractive indices: an integral representation,” *J. Opt. Soc. Am. A, JOSAA*, vol. 12, no. 2, pp. 325–332, Feb. 1995, doi: 10.1364/JOSAA.12.000325.

[82] C. J. R. Sheppard and P. Török, “Effects of specimen refractive index on confocal imaging,” *Journal of Microscopy*, vol. 185, no. 3, pp. 366–374, Mar. 1997, doi: 10.1046/j.1365-2818.1997.d01-627.x.

[83] P. Török, “Focusing of electromagnetic waves through a dielectric interface by lenses of finite Fresnel number,” *Journal of the Optical Society of America A*, vol. 15, no. 12, p. 3009, Dec. 1998, doi: 10.1364/JOSAA.15.003009.

Chapter 2

Methodologies

This chapter will discuss the methodological information of the research experiments presented in this thesis. The topics of our technical discussions from the ***Section 2.1*** to the ***Section 2.4*** will include the systems of femtosecond-laser oscillator and pulse inspection devices, the pulse's energy and polarisation controllers, the mechanical stages for three-dimensional translation, the focusing objective lens, the approaches for substrate alignment and positioning, the post-processing methods of substrate cutting and polishing, and the thermal annealing processes. In addition to the mentioned inscription-related topics, the details of sample tests and characterizations will be thoroughly explained in the ***Section 2.5***. These characterization methods involve the refractive index profile retrieval based on the quantitative phase microscopy (QPM), the waveguide's near-field intensity detections and the optical guiding loss analysis.

As illustrated in Figure 2.1, the workflow diagram briefly describes the overall process of our femtosecond-laser inscription experiments, consisting of both the sample fabrications and characterizations, that were arranged in a chronological order. The conditional loop linking between the step 3 of laser-inscription and the step 4 of laser-induced structure checks represents the procedure that involved the alterations and optimizations of inscription parameters aiming to achieve the suitable conditions for the laser writing of an optical depressed-cladding waveguide, which will be later discussed in the Chapter 3 and the Chapter 4.

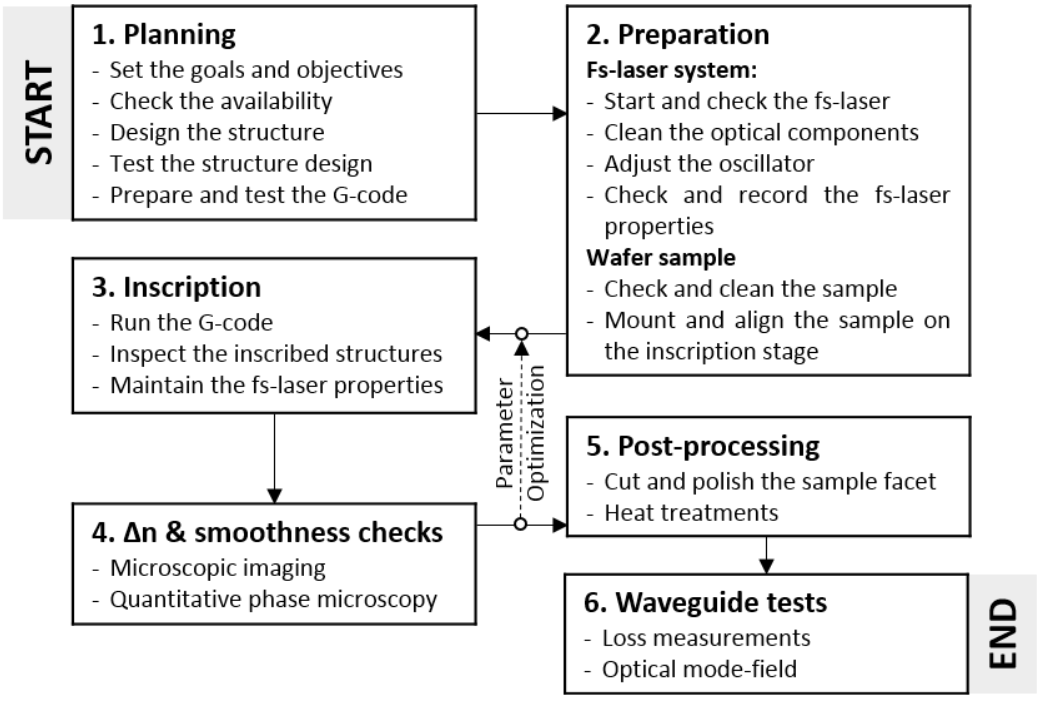

Figure 2.1 An overall experiment workflow.

2.1 System of femtosecond laser

2.1.1 Technical details

The laser system used in the laser-inscription process in this study was the 'Femtosource Scientific-XL' which was purchased from the Femtolasers Produktions GmbH. The system composed of two integrated units which were 1) a laser source and 2) a mode-locking laser oscillator. The laser source of the Verdi-V10 from Coherent was a solid-state diode-pumped and frequency-doubled Nd:YVO_4 laser that was connected to a water cooling system that had a setting temperature of ≈ 17.6 ºC. This light source could generate a continuous-wave (CW) laser with a narrow-band wavelength that was centred at 532 nm and had an optical power up to 10 W.

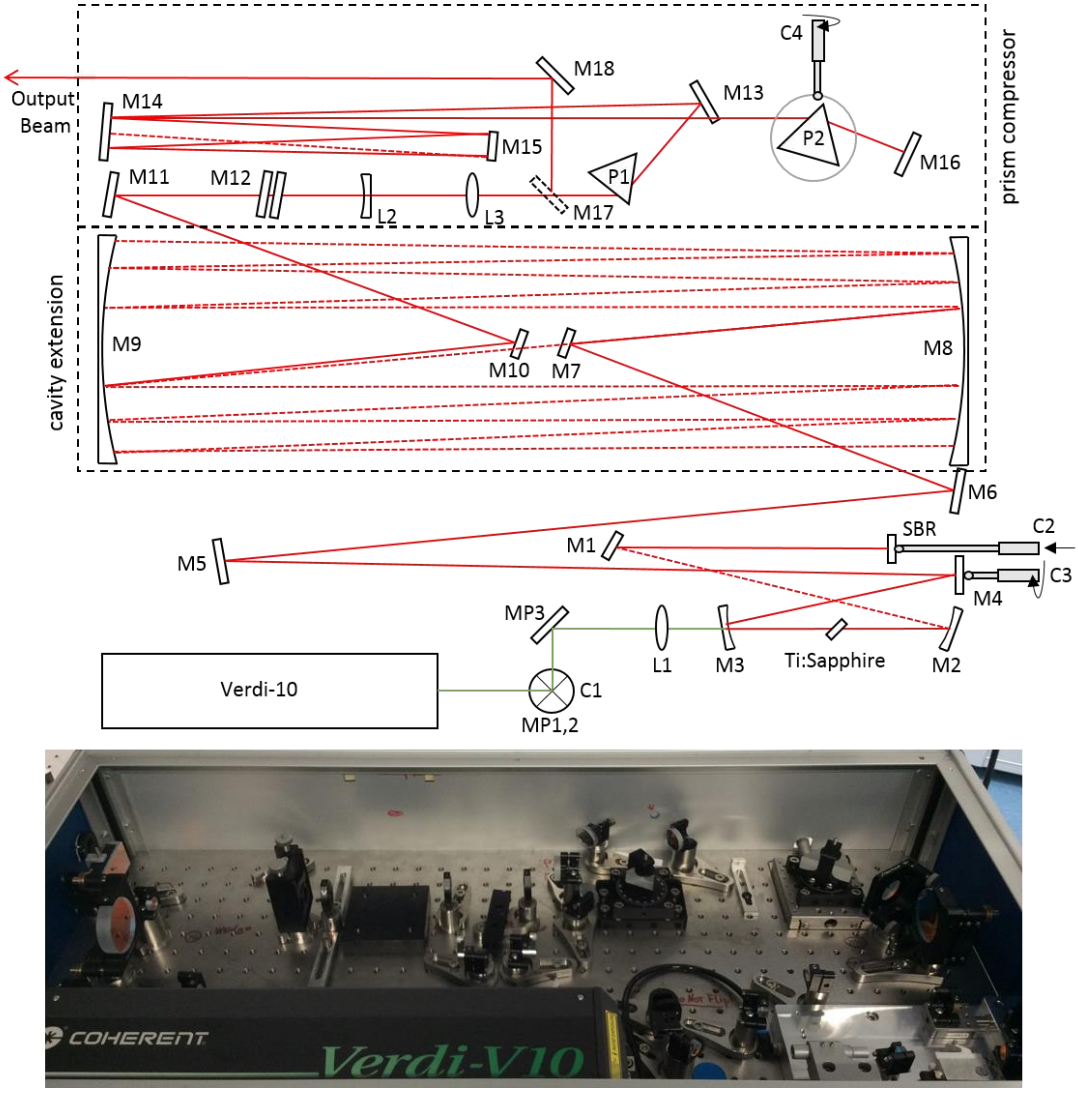

Figure 2.2 An optical cavity layout (top) and a photograph (bottom) of the Scientific-XL oscillator. The symbol's descriptions: MP1-3 are the steering mirrors, SBR is a saturable absorber, M8-9 are the telescope mirrors in the cavity extension, M13-18 are chirped mirrors, P1-2 are the prisms, M12 are the output coupling mirrors, C1 is picometre-step controller, C2 is a push rod, C3 is a cavity-length adjusting screw and C4 is a prism-angle adjusting knob.

In a normal working condition, the setting values of a laser source's power were at 0.1 W and 7.7 W (which corresponded to a pump current of $I \approx 24$ A) for the optical alignment and the laser-inscription processes, respectively. The pulse-duration compressing mechanism of this laser oscillator was based on a self-mode locking that utilized a gain medium of Ti:Sapphire that incorporated with a passive saturable absorber. As shown in an optical diagram of this Scientific-XL system in Figure 2.2, a laser beam with a wavelength of 532 nm was delivered into a laser cavity through the tilted gain-medium by a set of adjustable mirrors (**MP1-3**). In addition, the cavity arrangement which consisted of two telescope mirrors (**M8-9**) was acted as a Herriott multi-pass cell that provided an extension of the laser cavity's spatial length. In fact, the advantage of this cavity configuration was that the whole oscillator's system could have a compact footprint.

To address the optical nonlinear issues such as self-phase-modulation and self-focusing effects, our laser oscillator of Scientific-XL was designed to utilize the chirped-pulse amplification (CPA) technology with a positive dispersion regime (PDR) [1] operation. In general, the basic principle of this CPA technique is based on stretching-out a train of laser pulses in the time domain before it is introduced to the gain medium, which is followed by re-compressing them into pulses with a shorter temporal width after the processes of optical amplification have been done. A pulse train is typically stretched to have a pulse duration of few picoseconds which results in the peak power that is usually less than a threshold for nonlinear phenomena [2]. This mechanism has been known to provide a laser operation with more optical stability and to prevent the damages that can be possibly occurred on any optical components along a beam path. It should be mentioned that, in our system, a specially designed set of chirped mirrors and prisms was used for these mentioned processes of pulse stretch and compression.

The section of a prism compressor shown in Figure 2.2 helped to recompress the temporal width of chirped pulses into a femtosecond scale before they were outputted from the oscillator. The push rod **C2**, attached on a saturable absorber, was used to initiate the self-mode locking. The screw **C3** was utilized for adjusting the cavity length and, thus, allowed the pulse's spectral profile to be modifiable. The knob **C4** was used for rotating the prism **P2**, which enabled the manipulations of the pulse phase and the temporal duration. During our experiments, the relative positions and tilt angles of these oscillator's components were routinely checked and adjusted to ensure the optimal performance of the femtosecond-laser pulse generator. It is worth mentioning that if any re-alignment process would be required for the similar type of laser oscillator, based on our experiences, the process should start by trying to adjust the output beam intensity profile by using the output coupling mirrors (**M12**), then maximizing an output power of the non-amplified beam by fine-tuning the mirror **M1.** It would be also crucial to ensure that the proper beam-spot patterns can be observed on the telescope mirrors **M8-9** and the plane mirror **M14**. In addition, there should be no beam clipping presented on any part of reflectors or prisms.

2.1.2 Inspection of pulse properties

It has been known that the physical and optical properties of a laser-inscribed structure are highly sensitive to the optical characteristics of an inscribing laser beam. Some key parameters of these beam characteristics usually include the pulse power (P_{avg}), the temporal duration (τ), the spectral width ($\Delta\lambda$), the central wavelength (λ_0) and the spatial intensity distribution at a beam focus. Hence, it was necessary for our study to monitor and control such parameters to be remained in the range of values that could lead to the productions of a desirable outcome of laser modifications. The Table 2.1 shows the set of these inscribing-laser's parameters that was found, from the inscription parameter tests in the Chapter 3, to produce the laser-material modification with the optimized properties for our works. Also, some technical details of the relevant measurement tools have been described in the mentioned table. Figure 2.3 and 2.4 depict some examples of computer software's interfaces used with the inspection tools. In fact, the beam spatial and spectral profiles in Figure 2.3, as well as the laser temporal and spectral profiles in Figure 2.4, could be simultaneously monitored which greatly benefited our optical adjustment processes. The in-situ alignments of these devices will be shown in the next section.

Table 2.1 The range of laser pulse parameters and the corresponding tools of measurement.

Properties	Optimum range	Model of measurement tools	Vender
P_{avg}	0.88 – 0.95 W (CW) 0.98 – 1.05 W (Pulse)	FieldMaxII-TOP laser power meter	Coherent
τ	70 – 80 fs	Frog Grenouille 8-50 auto-correlator	Swamp Optics
$\Delta\lambda$	22 – 26 nm	QE65000 spectrometer	Ocean Optics
λ_0	790 – 794 nm		
beam profile	Slightly elliptic	BP109-IR beam profiler	Thorlabs

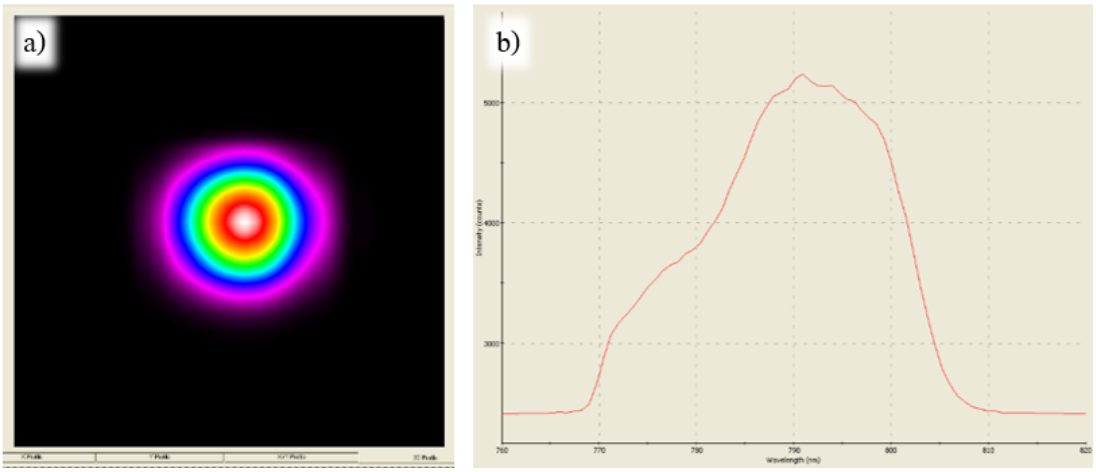

Figure 2.3 Software interfaces of a) BP109-IR beam profiler (Thorlabs) and b) QE65000 spectrometer (Ocean Optics) for monitoring the beam intensity distribution and the spectral profile, respectively.

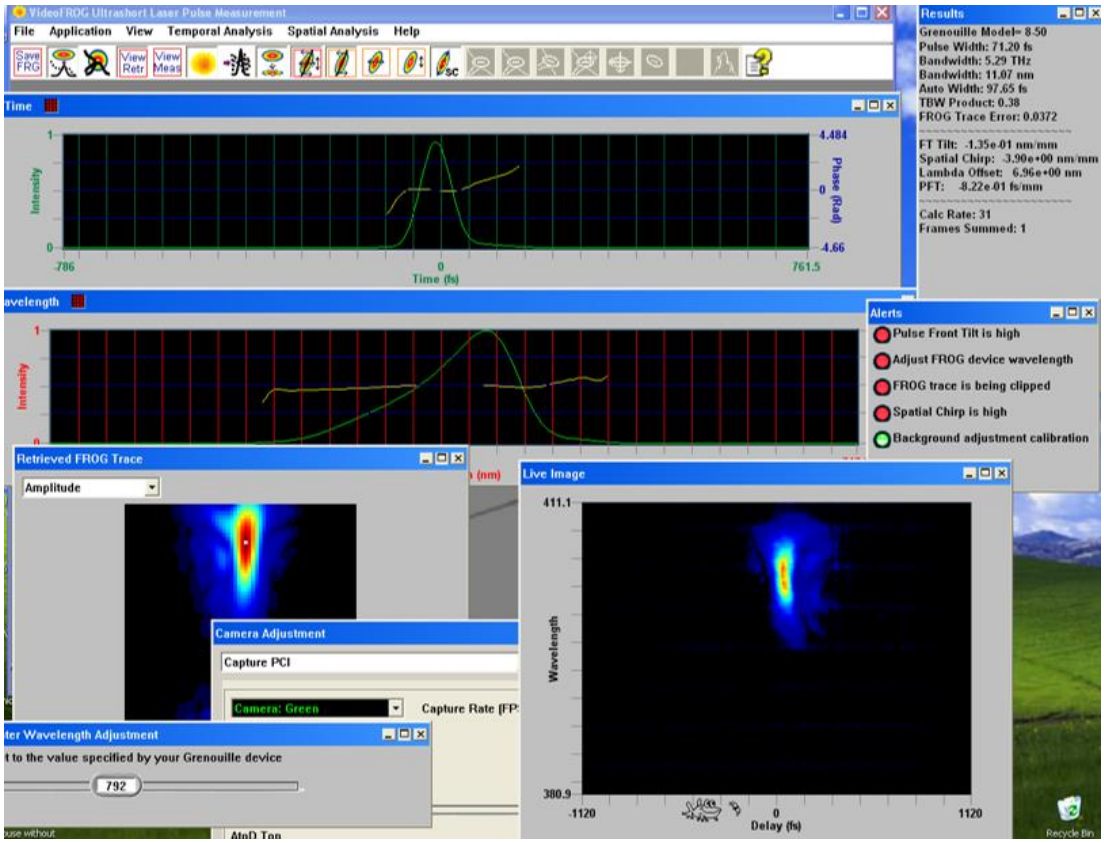

Figure 2.4 Software interface of FROG Grenouille 8-50 auto-correlator (Swamp Optics). The pulse duration and the spectral and temporal profiles of the fs-laser pulse could be checked and recorded.

2.2 System of inscription stages

2.2.1 Pulse energy and polarisation controls

To control the amount of laser energy that was focused onto the sample, the sets of half-wave plate (**#2**) and Brewster-angle polarisers (**#3**) were used and they were arranged as illustrated in Figure 2.5. By adjusting a relative axial angle between the waveplate and the polarisers by means of an attached rotary stage (PI Physik Instrumente), the amount of pulse energy could be precisely controlled to be in a desired range during the laser inscription. The laser power meter (FieldMaxII-TOP) or the beam profiler (BP109-IR) could be selectively inserted into the beam path at a position of **#12** to measure either the beam average power or the intensity distribution, respectively. A portion of the laser beam was scattered from the laser-stop plate (**#9**) into the spectrometer (**#10**, QE65000 spectrometer) to allow the spectral profile inspections. The mirror **#5** could be flipped-up to re-direct the laser into the FROG Grenouille 8-50 auto-correlator (**#7**) for evaluating the pulse temporal width and its phase profile. In this study, the laser pulse state of circular polarisation was set by using a quarter-wave plate that was located at a position of **#11**.

To better understand the temporal width analysis which was a crucial process for monitoring and controlling the inscribing-pulse properties, the basic mechanism of FROG will be briefly described here. FROG or 'the frequency-resolved optical gating' is a technique that had been developed for characterizing an ultrashort laser pulse. It partially shares the same ideas of a measurement based on the autocorrelation technique in which the pulse is used to measure itself, but FROG involves the analysis of pulse's spectrogram which can provide the full characterizations of pulse properties in both temporal and spectral domains [3]. Basically, the process requires splitting of the pulses into two beams, temporally retarding one, and overlapping them in a nonlinear medium which has a frequency-conversion capability such as the second- and the third-harmonic generations. Then, by adjusting the relative time-delay and observing the variations of a frequency-converted signal, an information of the pulses in a temporal domain can be obtained along with a spectrogram collected by a spectrometer located in the beam traces. Finally, an iterative algorithm such as the generalized projections (GP's) [4] is typically used for evaluating the data of pulse's intensity and phase as the functions of both frequency and time.

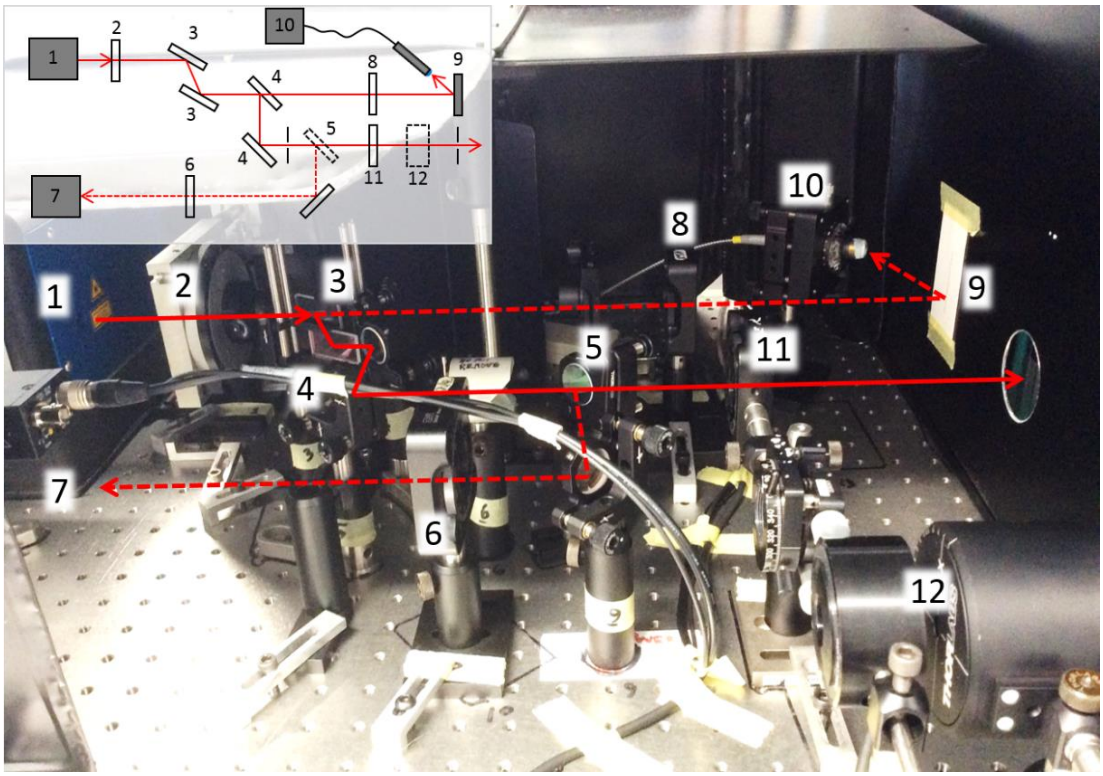

Figure 2.5 Photograph and layout (inset) of the experimental setup show 1) Scientific-XL oscillator, 2) a half-wave plate attached to rotary stage (PI Physik Instrumente), 3) a pair of Brewster angle polarisers, 4) mirrors, 5) a flip mirror, 6) a half-wave plate, 7) an auto-correlator (Frog Grenouille 8-50), 8) a half-wave plate, 9) a laser-stop plate, 10) a spectrometer (QE65000), 11) a half- or queater-wave plate, and 12) laser power meter (FieldMaxII-TOP) or beam profiler (BP109-IR). Red arrow represents the beam path of fs-laser. The beam from the wave plate (11) entered the inscription unit through the circular hole of the metal enclosure.

2.2.2 Focussing lens and translation stages

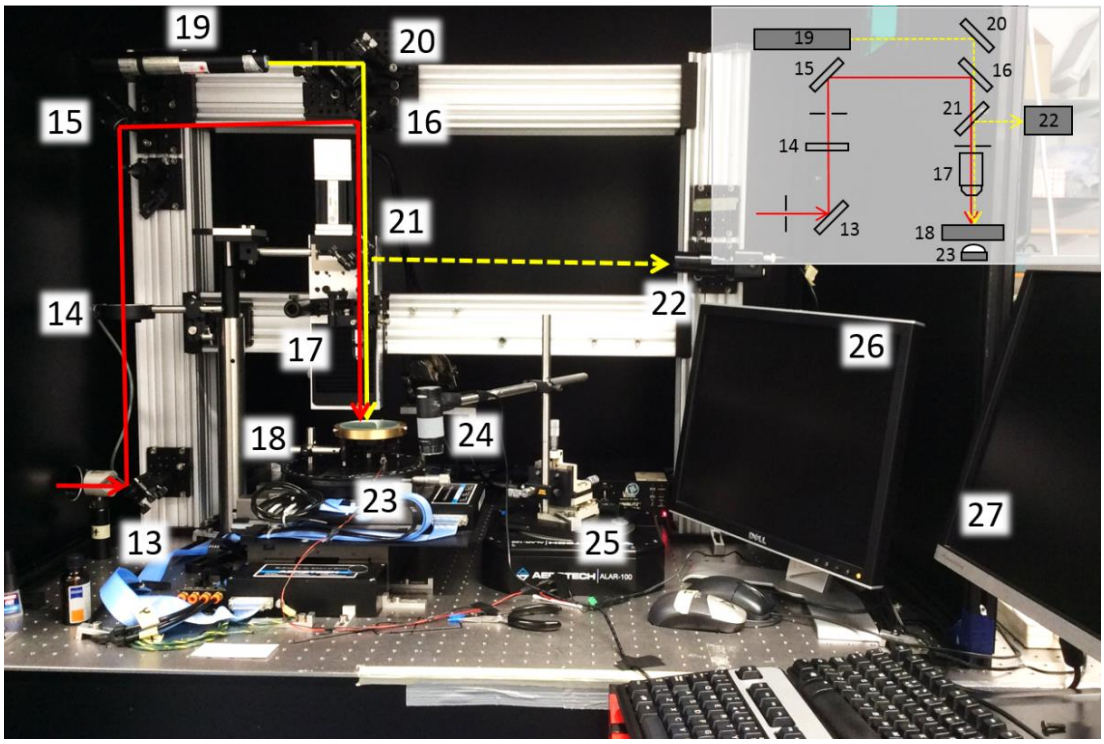

Figure 2.6 Photograph and layout (inset) of the experimental setup show 13-16) mirrors directing the beam to 17) the microscope objective and into a sample on 18) a sample holder and a horizontal translation stage, 14) an electronic shutter (Uniblitz Electronic), 19) HeNe laser (Uniphase), 21) a splitter, 22) a CCD camera (Watec WAT-202B), 23) an illumination light source (general white LED), 24) an inspecting microscope camera, 25) camera's position adjusting knobs and a rotary stage (Aerotech ALAR100LP), 26-27) computer monitors. Red arrows represent the beam path of fs-laser. Yellow arrows represent the beam path of HeNe laser used for the sample aligning purpose. The fs-laser beam path continued from Figure 2.5.

Continued from Figure 2.5, the laser beam represented by the red line enters the system for laser inscriptions shown in Figure 2.6 through a circular hole on the side wall of a laser shielding box. The beam reflected on the mirrors of the number #13, #15 and #16, then passed through an electronic shutter purchased from Uniblitz Electronic at #14 into an oil-immersed microscope objective (#17). The specifications of the objective lens were a magnification of 100× and the numerical aperture of 1.25. This focusing lens was required to be applied with an Immersol-518F immersion oil that had a refractive index of 1.518, which was purchased from Zeiss. The vertical position of the microscope objective was adjusted by means of an attached linear mechanical-bearing stage (Aerotech ATS100-100) that could operate with a spatial accuracy of ±0.5 μm. The sample holder located at #18 was attached to a two-dimensional air-bearing translation stage (Aerotech ABL10050-LN) that was able to move with a translation accuracy of ±0.2 μm and a maximum travelling distance of 50 mm along both *x* and *y* directions. The translation stages were controlled via a desktop-computer interface through the A3200 Npaq motor driver and controller from Aerotech. A commercial software called 'Aerotech motion

composer' was utilized for sending the G-code commands to the stage's controller. The combinations of vertical and horizontal movements of the stages enabled a transverse writing of a three-dimensional structure with a micrometre-scale resolution inside the inscribed sample to be done. In fact, the maximum inscription depth was depending on a working distance of the focusing objective. The maximum depth of this objective lens was found to be approximately 250 μm for a laser-inscribed medium of lithium niobite crystal.

2.3 Sample alignment and positioning

To ensure that the horizontal plane of a sample surface was parallel to the moving plane of the two-dimensional translation stages, the alignment of sample's tilt angles had to be accordingly done prior to the laser-inscription processes. A set of equipment including a helium-neon laser (**#19**, Uniphase) and a CCD camera (**#22**, Watec WAT-202B) which was used in this aligning process was depicted in Figure 2.6. The yellow line represents an optical path of the HeNe laser beam which was split by a splitter (**#21**) into two beams that passed through (a solid line) the objective lens onto an inscribed sample and reflected (a dashed line) onto an optical sensor of the CCD camera (**#22**). To start the sample alignment process, the focusing microscope objective was positioned such that the HeNe beam was exactly focused on a top surface of the sample. This in-focus position of the focusing lens could be justified by observing an optical interference pattern (see Figure 2.7.a, for example) that was visualized by means of the CCD camera (**#22**). If the planes of a sample's surface and the 2-D translation stages were not parallel, any horizontal movements of the stages would typically result in the pattern deformations or an absence of the optical interface ring. Hence, the tilt angles and the horizontal plane of an inscribed sample could be corrected by using this fact.

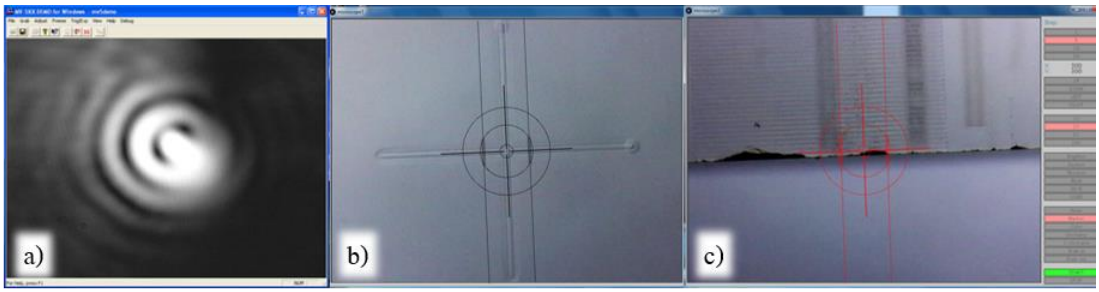

Figure 2.7 Screenshots of a) optical interference fringes detected by the CCD camera (#22 in Figure 2.6, Watec WAT-202B) which was used in the sample alignment, b) a marker inscribed on a microscopic slide and c) waveguide structures inscribed on a periodically-poled lithium niobate sample captured by the digital microscope camera (#24 in Figure 2.6).

To locate the beam focus in regard to the sample position, a digital microscope camera (**#24** in Figure 2.6) was used for visualizing the sample-surface's features in the vicinity where the beam was focused on. Aside from the positioning purpose, the camera was found a useful tool for

checking if there was any dust, crack or defects that could cause problems during the inscription process. Also, the images captured from this camera could be used for observing the top-view shape of a laser-modified region. It should be noted that there was a LED lamination source installed under the sample holder (**#23** in Figure 2.6) for enhancing the brightness and contrast of a captured image. Figure 2.7b and 2.7c depict examples of the microscopic images recorded by the digital camera through a house-made image-visualizing software that provided the handful image-processing functions of marker positioning and image resizing.

2.4 Post-processing processes

2.4.1 Cutting and Polishing processes

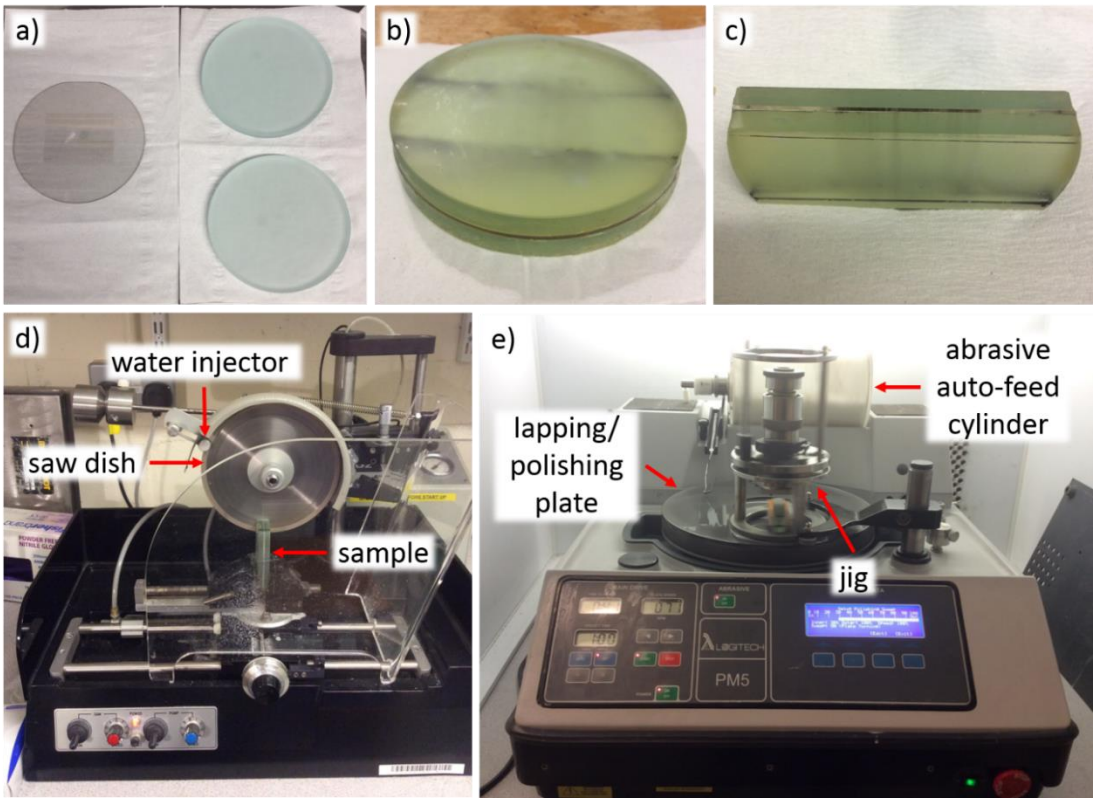

Figure 2.8 Photographs of a) a sample wafer and supporting substrates, b) a sample glued with a pair of supporting substrates, c) a sample after the cutting and before the polishing process, d) a disc saw (Logitech Model 15), and e) a lapping and polishing machine (Logitech PM5).

The lithium niobate samples that were used in this work were shipped from the manufacturer in a form of circular-shaped and surface-polished wafers. The sample's details and photograph can be found in Table 2.2 and Figure 2.8a, respectively. In order to test the optical guiding characteristics of the laser-inscribed structures, the samples were required to be cut such that there were two parallel facets like in Figure 2.8c where the testing beam could be delivered through the sample. In the cutting process, a diamond disc saw of Logitech Model 15 (see Figure

2.8d) that operated with a water coolant was utilized. It should be mentioned that before the sample could be cut it had to be glued with a pair of supporting glass substrates by a thermal quartz wax that had a melting temperature at ≈ 80 ^{o}C. Figure 2.8b shows an image of a sample attached onto supporting substrates, which was ready for the cutting and polishing processes.

Cut axis	Dopant	Vendor	Diameter	Thickness
x	5% MgO	Fujian Antek Optics	50 mm	0.5 mm
z	5% Mg	Fujian Antek Optics	76 mm	1.0 mm

Table 2.2 Sample details of the lithium niobate wafers used in this study.

After the sample was cut, its facets of two opposite sides were smoothened and polished into the surfaces with an observed transparency of optical grade by a PM5 lapping/polishing machine that is depicted in Figure 2.8e from Logitech. This polishing machine consisted of three main components which were a lapping/polishing plate, an abrasive feeding cylinder and a sample holder jig. In addition, there were two types of plates i.e. a cast iron plate and a NaClO-coated plate which were used in the lapping and polishing processes, respectively. The feeding cylinder could be used to store a slurry that was a mixture of abrasive powder and distilled water for a maximum amount of 1.5 litre. There were two types of abrasive powders, i.e. calcined aluminium oxide and amorphous silica which were applied in the stages of lapping and polishing, respectively. The feeding rate of abrasive slurry, as well as the rotational speed of the plate, were required to be adjusted accordingly. One may find the Table 2.3 for an example recipe of the lapping/polishing operational settings used in this study for a sample of z-cut lithium niobate.

Step	Type	Slurry type	Slurry amount	Plate type	Rotation Speed	Duration
1	Lap	9 μm particle	2.5 litres	Plain cast iron	70 rpm	2.5 hours
2	Lap	1 μm particle	2.5 litres	Plain cast iron	70 rpm	2.5 hours
3	Polish	50 nm (SF1)	5.0 litres	NaClO coated	70 rpm	17 hours

Table 2.3 An example recipe of the lapping/polishing operations for a facet of the sample

2.4.2 Heat treatment

An open-air furnace purchased from Carbolite was used in the thermal annealing processes. The temperature had to be manually adjusted for each annealing step. The temperature range of this furnace was between 25 ^{o}C and 1200 ^{o}C.

2.5 Characterization processes

2.5.1 Refractive index modification

To estimate a change of material's refractive index caused by the femtosecond laser inscription, a technique called 'Quantitative Phase Microscopy (QPM) [5], [6] which was able to evaluate a phase profile of an optical field transmitted through a non-absorptive sample was implemented in this study. This approach has been widely used in many fields, especially in the biology sciences [7], for enhancing the refractive-index-contrast information of the microscopic images captured by a traditional light-transmission microscope. In practical, the calculation processes of this QPM technique required at least three images in the bright field mode, which had to be captured at different depths of focus. These three depths included one at the in-focus depth, and two at the positive and negative de-focusing positions. The example images recorded at these varying distances were illustrated in Figure 2.9.a-c. It is worth mentioning that the terms of positive and negative de-focus were used here to describe the depths that were vertically upper and lower than the image's in-focus position, respectively.

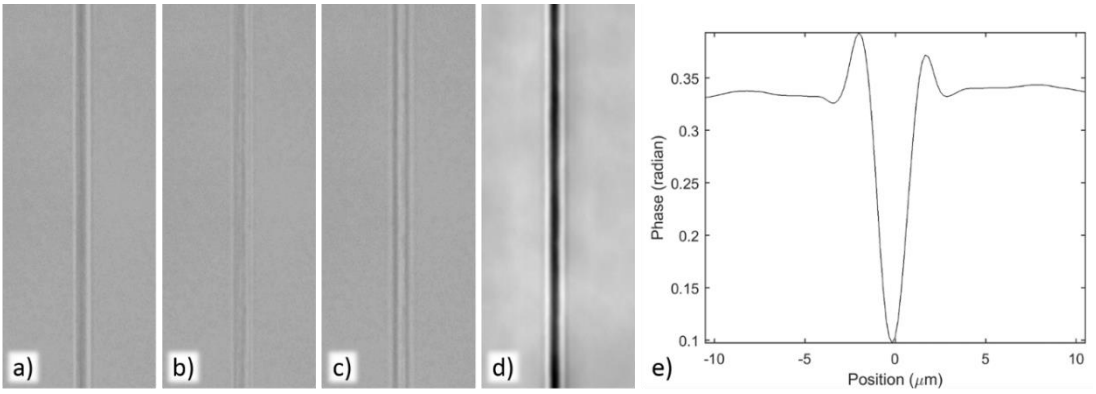

Figure 2.9 Bright-field images of an inscribed line in z-cut lithium niobate of a) negative de-focus, b) in-focus, and c) positive de-focus captured by a 20× microscope objective with a NA of 0.5. d) A phase profile calculated from the images a-c by an IATIA QPm software. e) A plot of phase versus position, averaged over a length of 0.5 mm along the inscribed line.

The choices of an objective magnification and the de-focusing distance should be accordingly chosen based on an actual size of the structures being analysed. In this study, a microscope objective with a magnification of 20x and a numerical aperture of 0.5 (plan-neofluar) was used. A distance of 4 μm was equally set for the positive and negative de-focus values. The microscope model used in our experiment was the Zeiss Axipkop 2-mot-plus, which was mounted with a band-pass filter that allowed a spectral centred at 530 nm wavelength to be transmitted. After the bright-field images had been captured, they were proceeded into the process of phase calculations by using a QPm software from IATIA. An example of the calculated 2-dimentional

phase profile is presented in Figure 2.9d. In addition, the average phase measured across the straight-line structure retrieved from the data in Figure 2.9d was plotted in Figure 2.9e.

Here, the calculation algorithm of the mentioned QPm software will be briefly discussed. Let's consider a coherent monochromatic light wave that propagates along the z-axis. Its complex amplitude that satisfies the Helmholtz equation under the paraxial approximation [8] can be expressed by the following equation.

$$A(\boldsymbol{r}) = u(\boldsymbol{r})e^{ikz} = \sqrt{I(\boldsymbol{r})}e^{i\phi(\boldsymbol{r})}e^{ikz},$$

where I is the light intensity defined by $I(r) \equiv |u(r)|^2$, ϕ is the wave phase and $\boldsymbol{r} \equiv (x, y, z)$. The term mentioned above can be rearranged such that it is in the form of

$$u(\boldsymbol{r}) = \sqrt{I(\boldsymbol{r})}e^{i\phi(\boldsymbol{r})} \tag{2.1}$$

which should still satisfy the paraxial Helmholtz condition, i.e.

$$\nabla_{\perp}^2 u(\boldsymbol{r}) + 2ik\frac{\partial}{\partial z}u(\boldsymbol{r}) = 0 \tag{2.2}$$

where $k = 2\pi/\lambda$ and $\nabla_{\perp}^2 = (\partial^2/\partial x^2) + (\partial^2/\partial y^2)$.

By inserting Equation 2.1 into Equation 2.2 and taking only their imaginary part, the equation becomes

$$I(\boldsymbol{r})\,\nabla_{\perp}^2\phi(\boldsymbol{r}) + \nabla_{\perp}I(\boldsymbol{r}) \cdot \nabla_{\perp}\phi(\boldsymbol{r}) + k\frac{\partial}{\partial z}I(\boldsymbol{r}) = 0 \tag{2.3}$$

Then, by rearranging Equation 2.3, one should get the following formula.

$$\nabla_{\perp} \cdot [I(\boldsymbol{r}) \cdot \nabla_{\perp}\phi(\boldsymbol{r})] = -k\frac{\partial}{\partial z}I(\boldsymbol{r}) \tag{2.4}$$

where the identities $\nabla^2(fg) = f\nabla^2 g + 2\nabla f \cdot \nabla g + g\nabla^2 f$ and $\nabla \cdot (fg) = f\nabla \cdot g + g\nabla \cdot \mathrm{f}$ were used. This equation of 2.4 has been known as the 'Transport of Intensity Equation' or TIE, which was derived by Teague in his literature [8]. Also, he did also introduce an auxiliary function ψ that satisfies the relation $\nabla_{\perp}\psi = I\nabla_{\perp}\phi$. By substituting this function into Equation 2.4, a formula that contains the second-order derivative term and a partial derivative of the transmission filed intensity can be expressed by

$$\nabla_{\perp}^2\psi(\boldsymbol{r}) = -\frac{2\pi}{\lambda}\frac{\partial}{\partial z}I(\boldsymbol{r}). \tag{2.5}$$

Since the information of the light intensity distribution (I) can be directly obtained from the microscopic images, the derivative term on the right-hand side of Equation 2.5 can be approximated by using the approach of finite difference which is

$$\frac{\partial}{\partial z} I(\boldsymbol{r}) \approx \left[\frac{I(x, y, z_0 + \Delta z) - I(x, y, z_0 - \Delta z)}{2\Delta z}\right] \tag{2.6}$$

where z_0 and Δz denotes the in-focusing depth and the de-focusing distance, respectively. Eventually, the phase $\phi(\boldsymbol{r})$ in Equation 2.4 can be retrieved by either the deterministic approach [9] or the iterative approach [10].

To convert the phase profiles calculated from the technique of QPm into the refractive index change of a laser-modified structure, a value of the lowest phase which was normally located nearby the centre of the average phase plot (like in Figure 2.9.e) was chosen and subtracted by the phase value taken from the area of un-exposed material. Then, if one labels this subtraction result as $\Delta\varphi$, the refractive index modification Δn should be evaluated by the following expression.

$$\Delta n = \frac{\lambda\, \Delta\varphi}{2\pi d} \tag{2.7}$$

where d is the thickness of the inscribed structure and λ is a wavelength of the microscope's source of illumination. The Δn defined in Equation 2.7 will be hereafter called the **'refractive index contrast'**, which will be used for representing the quantitative amount of a refractive index modification caused by the femtosecond-laser pulses on a material in our study.

2.5.2 Near-field mode and propagation loss

The optical guiding characteristics including the near-field mode, the mode-field diameter or MFD, the insertion loss, and the propagation loss of our laser-micromachined waveguides were measured by the equipment setup that is depicted in Figure 2.10. The light source located at **#1** emitted a laser beam that passed through a polarisation control unit, which consisted of a Glan-Taylor prism polariser (**#2**) and a half-wave plate (**#3**). The focusing lens module at **#4** was utilized to couple the light beam into a single-mode fibre pigtail, whose another end was attached to a fibre holder and a 6-axis NanoMax Max 603L/M alignment stage purchased from Thorlabs at **#5**. The positions (x, y, z) and tilted angles $(\theta_x, \theta_y, \theta_z)$ of the input fibre pigtail were carefully adjusted during the beam coupling process, such that the testing light beam was delivered through a sample which was attached on a rotating stage (**#6**). After the light beam left the tested sample, it was collimated by an Ealing microscope objective with a working distance of 16 mm and a numerical aperture of 0.4 at the number **#8**. The orientation of this collimating objective was

manipulated by using the second 6-axis stage located at **#9** so that the output beam was properly entered on a desired tool of measurements. In our experiment setup, these applicable measurement tools included the CCD camera (**#11**), the optical power detector (**#12**) and the fibre coupling unit (**#13**) of the optical spectrum analyser (**#14**). It should be noted that the reflectors at positions **#10** and **#12** could be flipped-up or -down to alter the beam path. More technical details of these mentioned tools and light sources can be found in Table 2.4.

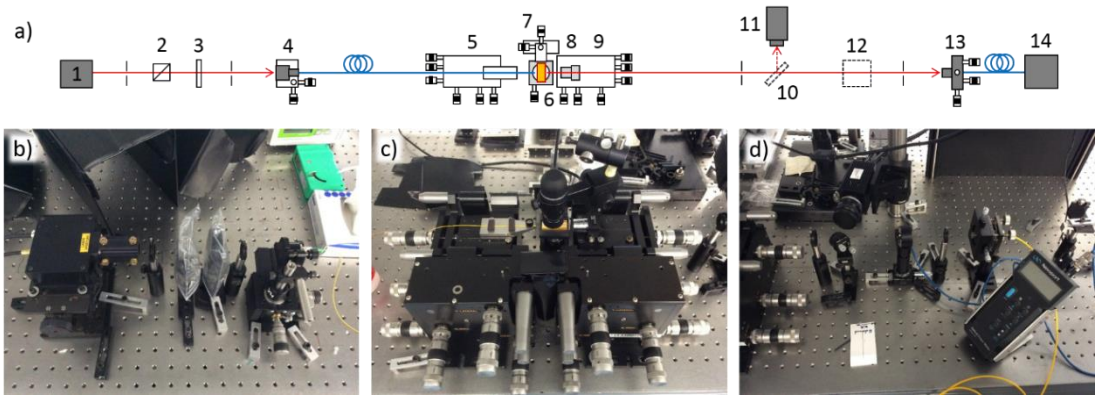

Figure 2.10 Layout (a) and photographs (b-d) of the experimental setup show 1) a laser source, 2) a Glan-Taylor prism polariser, 3) a half-wave plate, 4) a fibre coupling unit, 5) and 9) 6-axis alignment stages (Thorlabs NanoMax Max 603L/M), 6) a sample and its holder with angle adjustment, 7) a 3-axis alignment stage, 8) a microscope objective (Ealing, working distance = 16 mm, NA = 0.4), 10) a flip mirror, 11) a CCD camera, 12) a power detector (Newport) attached on a flip stand, 13) a fibre coupling unit, 14) an optical spectrum analyser (Agilent 86142B)

The near-field intensity distribution of the waveguide's output was monitored and recorded by the CCD camera (**#11**). The distance between the sample (**#6**) and the collimating lens (**#8**) was adjusted so that the beam spot was in-focused, i.e. the peak intensity showed the highest value and the beam profile became the most compact size. The mode (near-) field diameter (MFD), mathematically defined as the diameter where the intensity drops to $1/e^2$ of the field maximum intensity, was evaluated by applying the Gaussian fitting function onto the measured data to calculate the standard deviation (σ). Then, the MFD can be approximated by using the following formula.

$$\mathrm{MFD} = \frac{\sqrt{2}\,\mathrm{FWHM}}{\sqrt{\ln 2}} \approx 4.001\sigma. \tag{2.5}$$

The intensity profiles of waveguides were scaled by comparing them with the beam output from a standard single-mode fibre whose mode-field diameter (MFD) had been already provided by the vender.

The optical propagation loss (α) of a fabricated waveguide was calculated by using the mathematical expression below.

$$\alpha\ [\mathrm{dB/cm}] = \frac{L_i - 2L_c - L_m}{l} \tag{2.6}$$

where L_i is the insertion loss, L_c is the coupling loss, L_m is the mode-mismatch loss and l is the length of an optical waveguide.

The insertion loss L_i was calculated from the measured input optical power P_{in} and the measured output power P_{out} through the following relation:

$$L_i\ [dB] = 10 \log_{10} \frac{P_{in}}{P_{out}} \tag{2.7}$$

The coupling loss L_c, due to the Fresnel reflections at the medium interfaces, was approximated by

$$L_c = 10 \log_{10} \left\{ 1 - \frac{(n_1 - n_2)^2}{(n_1 + n_2)^2} \right\} \tag{2.8}$$

where n_1 and n_2 are the refractive indices of the air and lithium niobite, respectively. It is worth mentioning that there were two different values of L_c of our tested wavelength because of the birefringence characteristics of the medium of inscription (lithium niobate crystal).

Last but not least, the loss due to the optical mode mismatch (L_m) was evaluated by using the overlap integral approach which was expressed by

$$L_m = \frac{|\int E_1^* E_2 dA|^2}{\int |E_1|^2 dA \int |E_2|^2 dA} \tag{2.9}$$

where E_1 and E_2 were the electric fields that were presented before and after coupled into a tested sample, respectively.

Table 2.4 Details of the measurement tools in the processes of waveguide characterizations.

Tool	Vendor	Model	Specifications
Light source	Fianium	SC450-AOTF Supercontinuum light source with tuneable filter	λ = 450 – 700 nm Output power < 4.0 mW λ = 1022 – 1768 nm Output power < 1.5 mW
	QPhotonics	QFBGLD-1060-40 fiber coupler laser diode	λ = 1064.5 nm, Δλ = 0.03 nm Output power < 40 mW
		QRBGLD-1450-150 fiber coupler laser diode	λ = 1456.4 nm, Δλ = 2.44 nm Output power < 150 mW
		QDFBLD-1550-50 fiber coupler laser diode	λ = 1539.8 nm, Δλ = 0.01 nm Output power < 50.6 mW
	Lightwave	ILX MPS-8033 laser diode	λ = 1310 nm, Δλ = n/a Output power < 1.1 mW
Bandpass filter	Semrock	FF02-531/22-25	λ = 531 nm, FWHM = 28.1 nm Transmission > 93 %
		FF01-700/13-25	λ = 700 nm, FWHM = 20.4 nm Transmission > 93 %
		FF01-840/12-25	λ = 840 nm, FWHM = 21.1 nm Transmission > 93 %
Laser diode driver controller	Newport	Model 505	Current range = 0 – 200 mA Resolution = 0.1 mA
Laser temperature controller		Model 325	Current range = 0 – 2.5 A Accuracy = ± 2.5 A
CCD camera	Ophir	GRAS20 Firewire Si CCD	λ = 190 – 1100 nm Resolution = 1600x1200 pixels Pixel size= 4.4 μm x 4.4 μm
	Goodrich	SU320MS-1.7RT InGaAs CCD	λ = 900 – 1700 nm Resolution = 320x256 pixels Pixel size= 25 μm x 25 μm
Power detector	Newport	818-SL Si detector	λ = 400 – 1100 nm Sensitivity = 1 pW – 2 W Accuracy = ± 2 %
		818-IR Ge detector	λ = 780 – 1700 nm Sensitivity = 100 pW – 140 mW Accuracy = ± 3 %
Power meter		840-C optical power meter	Current range = 100 nA – 1 μA Accuracy = ± (2.0 – 2.5) %
Optical spectrum analyser	Agilent	Model 86142B	λ = 600 – 1700 nm Resolution = 60 pm – 10 nm Accuracy = ± 0.5 dB

Summary

In this chapter, the methodologies of our laser-inscription experiments and characterization processes have been thoroughly discussed. The figures of relevant instruments and the schematic diagrams of experimental setups have been included to clarify the contexts. In addition, the mathematical derivations which formed the basis of our sample characterizations involving the quantitative phase microscopy (QPM) and the calculations of optical guiding loss have been described. Hopefully, these texts of methodological explanations shall suffice an accurate repetition of any prospective studies.

References

[1] V. L. Kalashnikov and A. Apolonski, "Chirped-pulse oscillators: A unified standpoint," *Phys. Rev. A*, vol. 79, no. 4, p. 043829, Apr. 2009.

[2] V. L. Kalashnikov, E. Podivilov, A. Chernykh, and A. Apolonski, "Chirped-pulse oscillators: theory and experiment," *Appl. Phys. B*, vol. 83, no. 4, p. 503, Apr. 2006.

[3] R. Trebino *et al.*, "Measuring ultrashort laser pulses in the time-frequency domain using frequency-resolved optical gating," *Review of Scientific Instruments*, vol. 68, no. 9, p. 3277, Jun. 1998.

[4] K. W. DeLong, D. N. Fittinghoff, R. Trebino, B. Kohler, and K. Wilson, "Pulse retrieval in frequency-resolved optical gating based on the method of generalized projections," *Opt. Lett., OL*, vol. 19, no. 24, pp. 2152–2154, Dec. 1994.

[5] A. Barty, K. A. Nugent, D. Paganin, and A. Roberts, "Quantitative optical phase microscopy," *Opt. Lett., OL*, vol. 23, no. 11, pp. 817–819, Jun. 1998.

[6] D. Paganin and K. A. Nugent, "Noninterferometric Phase Imaging with Partially Coherent Light," *Phys. Rev. Lett.*, vol. 80, no. 12, pp. 2586–2589, Mar. 1998.

[7] C. L. Curl *et al.*, "Quantitative phase microscopy: a new tool for measurement of cell culture growth and confluency in situ," *Pflugers Arch - Eur J Physiol*, vol. 448, no. 4, pp. 462–468, Jul. 2004.

[8] M. R. Teague, "Deterministic phase retrieval: a Green's function solution," *J. Opt. Soc. Am., JOSA*, vol. 73, no. 11, pp. 1434–1441, Nov. 1983.

[9] T. E. Gureyev, A. Roberts, and K. A. Nugent, "Phase retrieval with the transport-of-intensity equation: matrix solution with use of Zernike polynomials," *J. Opt. Soc. Am. A, JOSAA*, vol. 12, no. 9, pp. 1932–1941, Sep. 1995.

[10] S. Mehrabkhani, L. Wefelnberg, and T. Schneider, "Fourier-based solving approach for the transport-of-intensity equation with reduced restrictions," *Opt. Express, OE*, vol. 26, no. 9, pp. 11458–11470, Apr. 2018.

Chapter 3

Single-scan Track Structures written by Fs-laser

The aims of this chapters were, firstly, to study the trends of track's properties in regards to various inscription setting, and secondly, to investigate a set of operational parameters that was most suitable for our fabrications of a depressed-cladding optical waveguide and other optical devices in the Chapter 4 and 5, respectively. It should be noted that the discussions here will concentrate only on a damaged (or the so-called 'Type II') structure. The other kinds of laser-induced modifications such as Type I structures, micro-voids and micro-grating structures will not be included in this part of thesis.

The key points of discussion in this chapter will focus on three important factors that have been known to influence the physical and optical characteristics of a structure inscribed by femtosecond-laser pulses on, particularly, our samples of *z*-cut lithium niobite crystal. These factors include the optical distortions of a beam focus, the total energy deposition of inscribing laser pulses, and the post-processing method of thermal annealing treatments. Note that the technical details of our femtosecond laser setup and relevant inscription systems can be found in the Chapter 2. The sets of tested structures consisted of an array of straight lines, which will be hereafter called 'tracks', created by the single-pass scan of laser pulses. The systemic alternations of the operational parameters had been applied to differing sets of laser-inscribed tracks.

The chapter consists of four main sections, in which the first three sections will be related to the mentioned factors affected the femtosecond-laser inscription and the last section will be the chapter's discussions and summary. In the ***Section 3.1***, two optical distortion effects including the spherical aberration and the birefringence-induced astigmatism will be theoretically discussed by using the numerical methods based on the integral representation of light diffraction. The obtained formulas were applied into the computer simulations for calculating the optical intensity profiles of a beam focus. Then, the results will be compared with the experiment results of track inscriptions at varying focus distances. In the ***Section 3.2***, the practical impacts of total pulse-energy deposition on a laser-modified volume will be demonstrated. This section composes of two parts which will separately discuss upon the operational parameters of the pulse energy and the writing speed. Plus, the writing-direction-dependent properties of an inscribed tracks will be reported. The ***Section 3.3*** will mention on the variations of track's properties after thermally treated by heats at different temperatures ranging from 250 to 950 ^{o}C.

3.1 Optical distortions of beam focus

When a beam of femtosecond-laser pulses was focused by a focusing micro-objective lens and delivered into a material for the inscription to take place, an intensity distribution of the beam's focus could be spatially distorted by many means such as a spherical aberration, an astigmatism aberration and so on. These kinds of optical distortions can consequently result in an irregular and/or asymmetric formation(s) of the laser-modified areas inside the material. In this section, the causes and effects of these beam distortions will be comprehensively discussed on both theoretical and experimental perspectives. For the laser inscriptions in this study, it was presumed that the most relevant optical aberrations involved the ***spherical aberration*** and the ***birefringent-astigmatism aberration***.

3.1.1 Spherical aberration

Let's start by considering a schematic diagram in Figure 3.1 of a beam that was focused by an objective lens. It has been known that a spherical aberration can occur if there is a mismatch of refractive indices between the first medium of an immersion oil with an index n_1 and the second medium of an inscribed material with an index n_2. The presence of this aberration type can consequently result in spatial variations of the beam focus from an ideal Gaussian intensity distribution, and also degradations of its peak intensity and energy density. In addition, this effect has been found to be more severely observed when the depth of focus became increased which is considerably problematic for a laser-inscription process presented in this thesis. Because of this reason, it is crucial to study this kind of refractive-index-mismatching induced effect in order to investigate and optimize the parameters and experimental settings of our experiments such that an optical waveguide structure can be precisely created and hence performs a desirable optical characteristic.

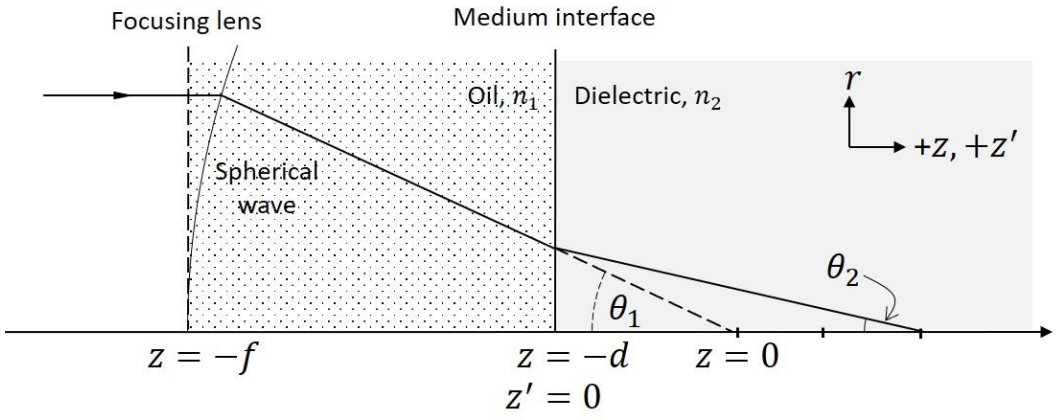

Figure 3.1 A schematic diagram of the focusing geometry for the study of optical focusing aberrations. It is assumed the case that $n_2 > n_1$.

This section applies the mathematical formulas derived in the literatures by Török *et al* [1]–[3], who extended the integral representation of light wave diffraction in a homogenous medium, proposed by Wolf [4], to a special case of a light wave that was focused through two mediums of different refractive indices. The details of theoretical derivations will not be presented here, instead, the key formulas that had been required for our study of numerical simulations will be explained. To proof the validity of our simulations, a set of calculation examples will be additionally presented and compared with the previous publications.

In Figure 3.1, a microscope objective lens with a focal length f was used for focusing an incoming plane-wave that propagates from the first to the second mediums of refractive indices n_1 and n_2, respectively. The plane-wave was assumed to be monochromatic and linearly polarised. The direction of wave propagation was along the *z*-axis, whose origin ($z = 0$) was located at a focusing position of the lens if the two mediums were assigned with an identical refractive index i.e. $n_1 = n_2$. For the sake of simplicity, a position of the interface between two mediums was designated at $z = -d$ and the position of lens focus was at $z = -f$. The variables θ_1 and θ_2 were the convergence angles of the focused rays of beam occupied in the first and the second mediums, respectively. In fact, it was assumed that the relation between θ_1 and θ_2 obeyed the Snell's law of refraction, which was

$$\theta_2 = \sin^{-1}\left(\frac{n_1}{n_2}\sin\theta_1\right) \tag{3.1}$$

Since it was assumed the paraxial approximation can be applied to this problem, the magnitude of an electric field distribution at an arbitrary position (r, z) in the cylindrical coordinates in the vicinity of the beam focus [5], [6] can be written in an expression of

$$\begin{aligned} E(r,z) = \int_0^{\Omega} & \sqrt{\cos\theta_1}\sin\theta_1 \boldsymbol{J_0}(k_1 r\sin\theta_1) \\ & \times \exp[ik_1\boldsymbol{\Psi} + ik_2 z\cos\theta_2] \\ & \times \left(\tau_s + \tau_p\, cos\,\theta_2\right) d\theta_1 \end{aligned} \tag{3.2}$$

where the aberration function $\boldsymbol{\Psi}$ was presumably defined by

$$\boldsymbol{\Psi} = -d(n_1\cos\theta_1 - n_2\cos\theta_2)\,, \tag{3.3}$$

and the wave factors k_1 and k_2 for the first and the second mediums were

$$k_1 = 2\pi n_1/\lambda_0\,, \qquad k_2 = 2\pi n_2/\lambda_0\,. \tag{3.4}$$

Then, if one considered a schematic diagram in Figure 3.2 that represents the directions of electric fields in two components of s- and p-polarisations, it was apparent that the Fresnel transmission coefficients (τ_s and τ_p) corresponding to these component can be expressed as the functions of the convergent angles θ_1 and θ_2 as

$$\tau_s = \frac{2n_1 \cos\theta_1}{n_1 \cos\theta_1 + n_2 \cos\theta_2} \qquad (3.5)$$
$$\tau_p = \frac{2n_1 \cos\theta_1}{n_2 \cos\theta_1 + n_1 \cos\theta_2}$$

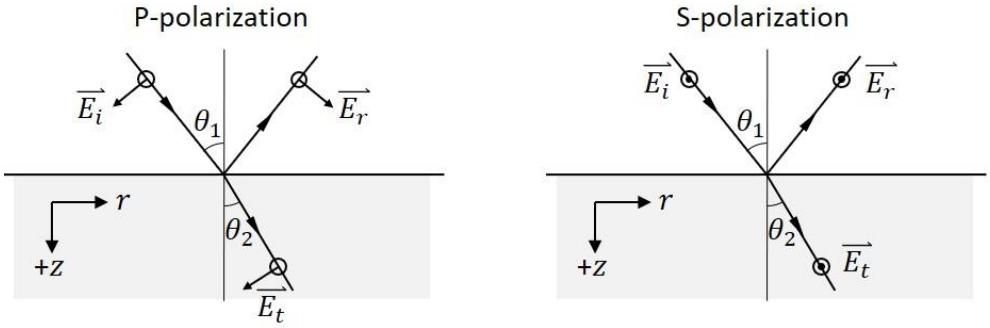

Figure 3.2 A schematic diagram shows the polarisation directions of the incident electric fields $\overrightarrow{E_\iota}$, the reflected electric fields $\overrightarrow{E_r}$, and the transmitted electric fields $\overrightarrow{E_t}$. The θ_1 and θ_2 are the incident angle and the refracted angle, respectively.

The function $\boldsymbol{J_0}(k_1 r \sin\theta_1)$, which was a Bessel function of the first kind, can then be ignored if only the field along the *z*-axis was needed to be evaluated. Hence, the Equation 3.2 can be simplified into a form of

$$E(z) = \int_0^{\Omega} \sqrt{\cos\theta_1}\sin\theta_1 \times \exp[ik_1\boldsymbol{\Psi} + ik_2 z\cos\theta_2] \times (\tau_s + \tau_p \cos\theta_2) d\theta_1 \qquad (3.6)$$

which actually represented an **axial electric-field distribution** or $\boldsymbol{E(0,z)}$ of the focused beam. It is worth mentioning that the integration limit, the semi-aperture angle Ω, can be approximated by using the formula $\Omega \approx \sin^{-1}(\mathrm{NA}/n_1)$, where NA was a numerical aperture of the focusing objective lens. To retrieve the magnitude of light intensity, the following equation shall be applied:

$$I(r,z) = |E(r,z)|^2 \ . \qquad (3.7)$$

In order to quantitively illustrate the mentioned effects of spherical aberration on the practical system of laser inscriptions, the Equations 3.1 -3.7 were used for programming in a

MATLAB software. An integral of the function in Equation 3.6 was calculated by a built-in numerical function that implemented an adaptive quadrature approach benefiting in an effective division of integration intervals. The accuracy of our simulation software was verified by applying the same set of calculation parameters presented in the previous literature by Marcinkevičius *et al* [5], and then observing their correspondences in the beam's intensity distributions. These parameters included the refractive index of an immersion oil $n_1 = 1.515$, the refractive index of a silica glass $n_2 = 1.473$, the laser wavelength $\lambda_0 = 800\,nm$, and the numerical aperture (NA) of an objective lens NA = 1.35. Our computational results of the axial and the two-dimensional intensity distribution of a focused beam when it was distorted by the spherical aberration were presented in Figure 3.3a and 3.3b, respectively. It can be clearly observed that, in Figure 3.3a, the intensity profiles were broadened and decreased in the intensity maximum when the focusing depth increased. In addition, some minor peaks occurred toward the direction of beam propagation can be noticed. The two-dimensional intensity profile in Figure 3.3b illustrates that the beam peaks also spread in a horizontal plane which results in a highly asymmetric focus's profile. In comparison with the Marcinkevičius's paper [5], our calculation results have apparently shown a good agreement.

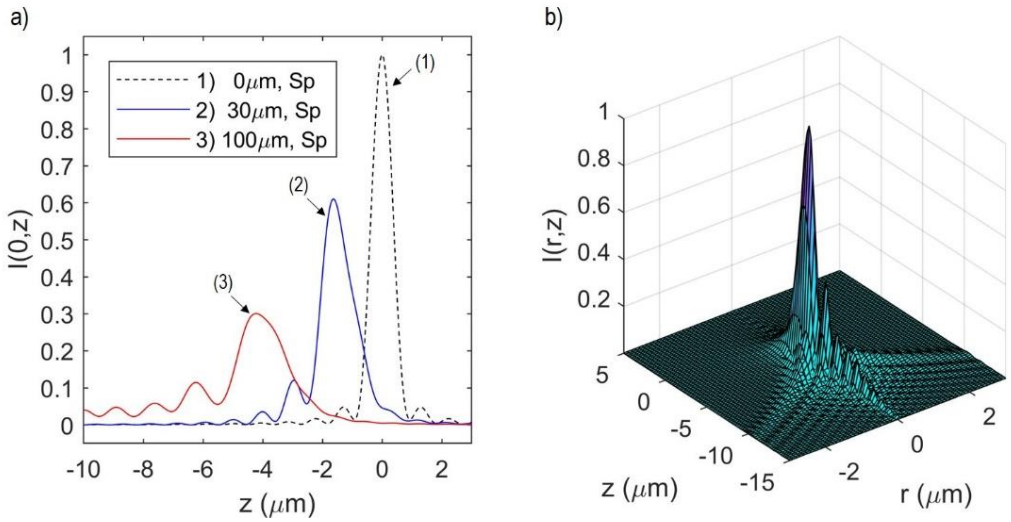

Figure 3.3 Computer simulation results of the spherical aberration effects: a) axial intensity distribution at different depths of focus $d = 0, 30, 100$ μm, and b) two-dimensional spatial intensity at a focus depth of $d = 30$ μm. The parameters were taken from [5]: $\lambda_0 = 800$ nm, NA = 1.35, $n_1 = 1.515$ and $n_2 = 1.473$.

The next section will discuss about another important cause of optical distortions on a focused beam, the "birefringent-astigmatism", which has been reported by many researchers to be significantly problematic for a laser-inscription process in any materials with birefringent refractive-indice. In the Section 3.1.3, the analysis of the combined effects of spherical and birefringence-induced aberrations, which was adapted for our laser system, will be presented.

3.1.2 Birefringent-astigmatism aberration

A crystalline lithium niobate, which was the material substrate mainly used in this study, is known as a uniaxial-birefringent dielectric that has an extraordinary refractive index (n_e) less than an ordinary refractive index (n_o). In fact, the refractive index difference $n_o - n_e$ of a lithium niobate crystal of roughly 0.08 has been reported, which was calculated from the $n_o = 2.2566$ and $n_e = 2.1766$ at a wavelength of $\lambda \approx 790$ nm [7] corresponding to our inscribing pulses. This amount of refractive index difference had been experimentally and numerically demonstrated to be sufficient in inducing the beams of different polarisations to be focused at separate distances. This phenomenon is known as the 'focus splitting' [8]. In order to quantitatively examine the influences of this birefringent-induced focus splitting which in this case presumably occurs along with the previously mentioned spherical aberration, this section will purpose a set of formulas that have been modified from those in the Section 3.1.1 to include the effects of birefringent-astigmatism in the similar scenario of an focused beam. It must be pointed out that this derivation will be based on a simplified assumption that the s- and the p-polarised components of the electric field distribution in Equation 3.6 can be separately considered and written as a following expression:

$$E(r,z) = E_s(r,z) + E_p(r,z). \tag{3.8}$$

Then, one can see that for the beam propagates like in Figure 3.1 (where the optical axis of lithium niobate is along the z-axis) the s-component should feel only the ordinary refractive index (n_{2o}) and will not be affected by the birefringence. Thus, the magnitude of an electric field distribution in s-component E_s can be written as

$$\begin{aligned} E_s(r,z) = \quad & \int_0^{\Omega} \tau_s' \sqrt{\cos\theta_1}\, \sin\theta_1 \boldsymbol{J_0}(k_1 r \sin\theta_1) \\ & \times \exp[ik_1 \boldsymbol{\Psi_s} + ik_{2s} z \cos\theta_{2s}] d\theta_1. \end{aligned} \tag{3.9}$$

where the related symbols in Equation 3.6 are labelled with *s* to refer to the s-component. The symbol of the second-medium's index n_2 was replaced by n_{2o} which represents the ordinary refractive index of the crystal. The Equations 3.3-3.5 become

$$\begin{aligned} \tau_s' = \quad & \frac{2n_1 \cos\theta_1}{n_1 \cos\theta_1 + n_{2o} \cos\theta_{2s}} \\ \boldsymbol{\Psi_s} = \quad & -d(n_1 \cos\theta_1 - n_{2o} \cos\theta_{2s}) \\ k_{2s} = \quad & \frac{2\pi n_{2o}}{\lambda_0} \end{aligned} \tag{3.10}$$

The convergent angle θ_{2s} (similar to θ_2, see Figure 3.1) relates to θ_1 by

$$\theta_{2s} = \sin^{-1}\left(\frac{n_1}{n_{2o}}\sin\theta_1\right). \tag{3.11}$$

For the p-component polarisation, the subscript *p* is here added to the related symbols. Then, the Equation 3.6 is rewritten only for the component of p-polarisation i.e.

$$\begin{aligned} E_p(r,z) = \quad & \int_0^{\Omega} \tau_p' \cos\theta_{2p} \sqrt{\cos\theta_1}\, \sin\theta_1 \boldsymbol{J_0}(k_1 r \sin\theta_1) \\ & \times \exp\left[ik_1 \boldsymbol{\Psi_p} + ik_{2p} z \cos\theta_{2p}\right] d\theta \end{aligned} \tag{3.12}$$

The refractive index n_{2p} in an equation of an electric-field in Equation 3.12, in contrast to that of the s-component, varies with the angle of beam that propagates in the second medium. This variation of effective refractive n_{2p} can be represented by a formula of index-ellipse, i.e.

$$n_{2p} \approx \frac{n_{2o} n_{2e}}{\sqrt{n_{2o}^2 \sin^2\theta_{2p} + n_{2e}^2 cos^2\,\theta_{2p}}} \tag{3.13}$$

In consequence of the Equation 3.13, the variables in the Equation 3.12 should be re-defined by using the following formulas,

$$\begin{aligned} \tau_p' = \quad & \frac{2n_1 \cos\theta_1}{n_{2p}\cos\theta_1 + n_1 \cos\theta_{2p}} \\ \boldsymbol{\Psi_p} = \quad & -d\left(n_1 \cos\theta_1 - n_{2p}\cos\theta_{2p}\right) \\ k_{2p} = \quad & \frac{2\pi n_{2p}}{\lambda_0} \end{aligned} \tag{3.14}$$

where the angle θ_{2p} can be related back to the refracting angle of the s-component θ_{2s} by the below approximation,

$$\theta_{2p} \approx \tan^{-1}\left(\frac{n_{2o}^2}{n_{2e}^2}\tan\theta_{2s}\right) \tag{3.15}$$

In Figure 3.4, the plots show the computer simulation results of the axial intensity distributions of a focused beam by using the purposed sets of equations, the Equations 3.7-3.15. The parameters for the presented simulations were retrieved from a literature by Zhou *et al* [8]. The left plot compares the axial intensity profiled that were affected by the spherical aberration only (labelled by 'Sp') and by both aberration effects (labelled by 'Sp+Bi'). The result clearly demonstrate that the refractive-index birefringence added to the calculations results in splitting of a focused beam into two factions of intensity peaks. In the case of Sp+Bi, the intensity maximum

was significantly decreased in its magnitude, and was also shifted to a shallower position along the *z*-axis. The right plot demonstrates the impacts of the combined aberrations on the beam focus at different depths ranging from 15 to 45 μm. It can be observed that the intensity profiles were dramatically deformed from its original shape when the beam was deeply focused inside the material. Although there were some minor differences such as the shifts of peak position when compared with the paper of Zhou *et al* [8], it was apparent that the important features such as the splits of the 2nd and 3rd peaks can be observed at closely similar depths. It should be also mentioned that if the plots of an axial intensity in Figure 3.3a and 3.4a were compared, the ripple-like intensity regions had the decreasing trends toward the opposite directions along the z-axis. These results indicated the varying impacts of spherical aberration on the different conditions of medium's refractive indices, i.e. the ripple-like trend was toward the -z when $n_2 < n_1$ like in Figure 3.3a and it was toward the +z which was the beam propagation direction when $n_2 > n_1$ shown in Figure 3.4a.

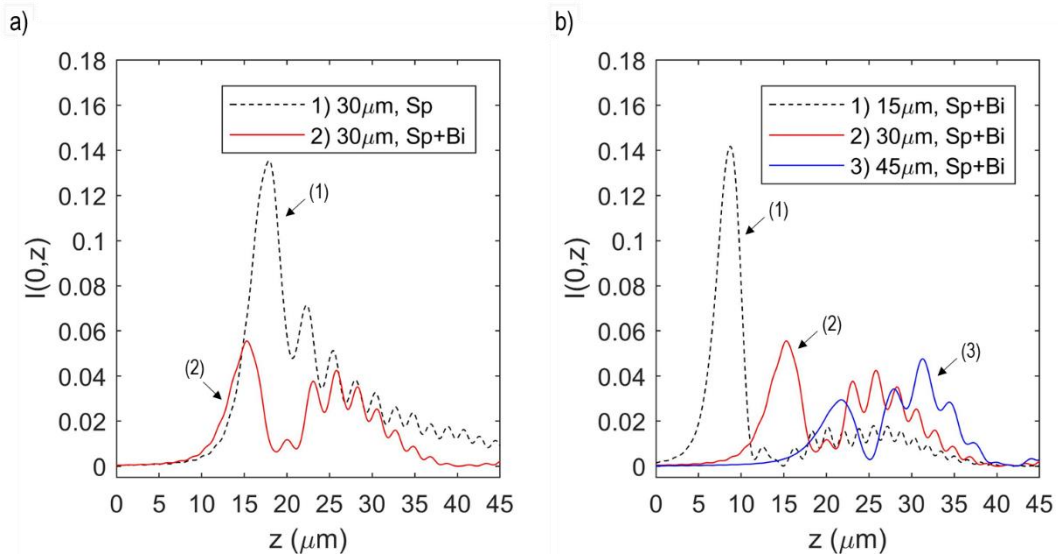

Figure 3.4 Computer simulation results show the combined effects of the spherical aberration and the birefringent astigmatism on the focused axial intensity distribution. a) A comparison between 1) the spherical aberration only ($n_{2o} = n_{2e} = 2.2291$) and 2) the combined effects ($n_{2o} = 2.2391,\ n_{2e} = 2.2191$). b) A comparison of the combined effects at different depths of focus $d = 15, 30, 45$ μm. Other parameters retrieved from [8] were $\lambda_0 = 800\ nm$, NA = 1.45, and $n_1 = 1.518$.

3.1.3 Simulations of optical focusing aberrations

In this section, the numerical methods (Equations 3.7-3.15) that had been developed in the Section 3.1.1 and 3.1.2 will be applied to simulate the laser focusing conditions of our experiment setups. The corresponding parameters used in the software included a numerical aperture (NA) of the focusing lens of 1.25, an inscribing laser wavelength (λ_0) of 790 nm and a refractive index (n_1) of an immersion oil (the first medium) of 1.518. It should be noted that a refractive index (n_2) of the second medium which was a lithium niobate crystal was applied with different sets of

values i.e. ($n_{2o} = n_{2o} = 2.2166$) were used for simulating only the spherical aberration and ($n_{2o} = 2.2266$ and $n_{2e} = 2.2066$) were used for calculating the additional influences of birefringent astigmatism.

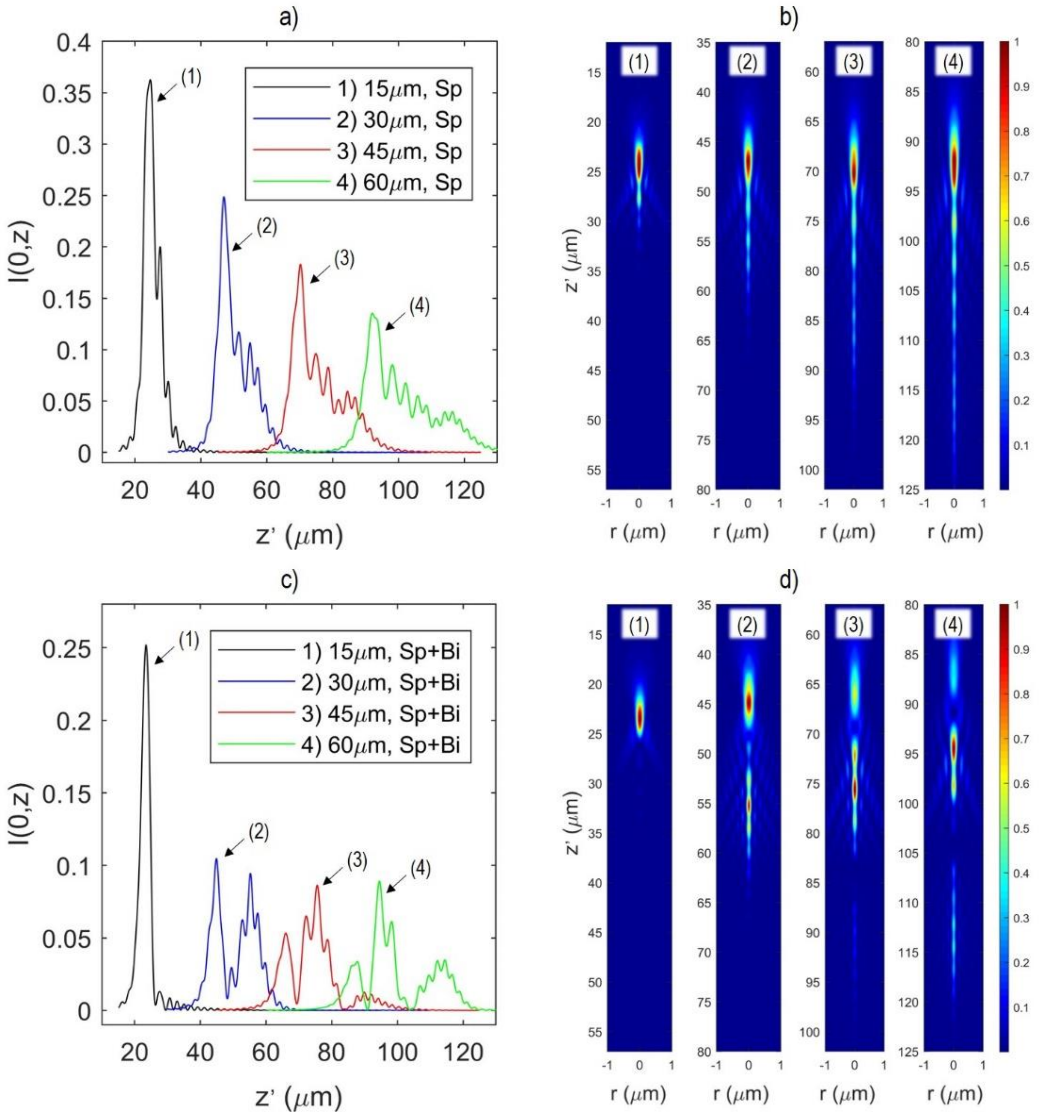

Figure 3.5 Computer simulation results show the effect of a-b) spherical aberration only ($n_{2o} = n_{2e} = 2.2166$) and c-d) the combined effect of spherical aberration and birefringent astigmatism ($n_{2o} = 2.2266, n_{2e} = 2.2066$) on the axial intensity distribution shown in a) and c) and the two-dimensional intensity profile in b) and d). The results were calculated using four different depths of focus $d = 15, 30, 45, 60$ µm. Other parameters were set based on our experimental setup, i.e. $\lambda_0 = 790$ nm, NA = 1.25 and $n_1 = 1.518$.

It is apparent that under a spherical aberration only, see Figure 3.5a, the axial intensity profiles of a focused beam were noticeably elongated along the *z*-axis when the depth of focus increased. Also, the presence of minor peaks can be observed toward the direction of beam propagation. The simulations of two-dimensional intensity, in Figure 3.5b, illustrated the elliptic shape of beam profiles that incorporated with the tails of intensity elongations. In Figure 3.5c and 3.5d, the inclusion of birefringent refractive index resulted in the splits of the beam intensity

starting from the focusing depth of 30 μm. In addition, the magnitude of peaks with the highest intensity had been noticeable decreased when compared with the beam profiles in Figure 3.5a that were un-affected by the birefringent astigmatism. It was found that in certain ranges of focusing depth ($d \approx 33 - 51\mu m$, see Figure 3.5c-d and 3.6f) the position of peaks with the highest intensity became shifted toward the direction of beam propagation, i.e. from the first to the second splitting peak location where the minor splits of intensity distribution can be observed. This shifting behaviour of beam spot might potentially cause an issue on the laser-inscription process, since it would be difficult to precisely predict the actual position along the beam-propagation direction of a laser-inscribed structure. Therefore, these kinds of numerical simulation presented in this section should offer a useful information for the experiments in this thesis and other related studies for estimating the highest intensity location of a focused laser beam. It should be noted -

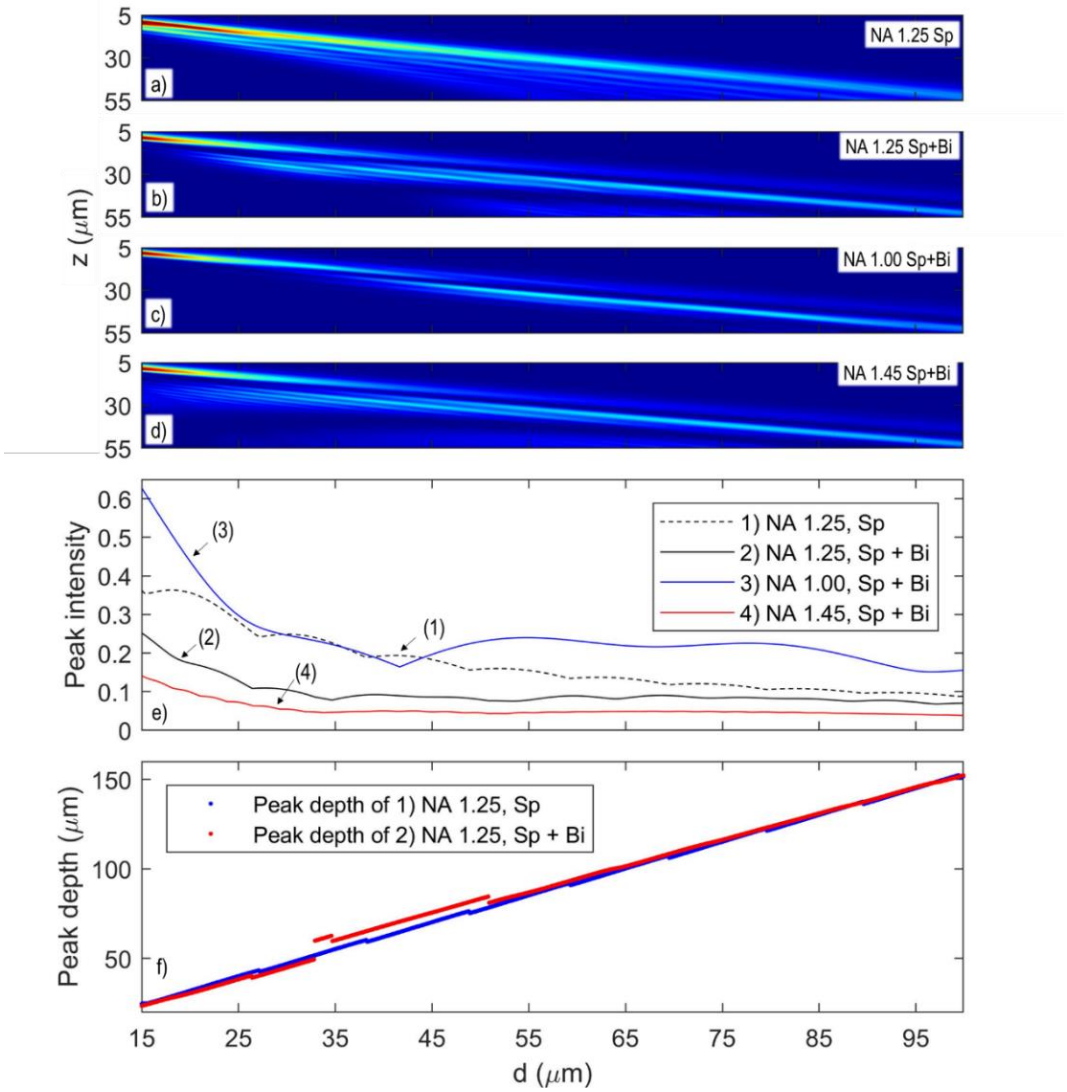

Figure 3.6 The effect of the spherical aberration only ($n_{2o} = n_{2e} = 2.2166$) and the combined effect of spherical aberration and birefringent astigmatism ($n_{2o} = 2.2266, n_{2e} = 2.2066$) at different values of the numerical aperture (NA $= 1.00, 1.25, 1.45$), which were plotted versus the distance d in horizontal axis. $\lambda_0 = 790$ nm and $n_1 = 1.518$.

that the z'-axis shown in the plots in Figure 3.5 was actually represented a distance measured from the medium interface, which can be equally described by "a distance measured in the z-coordinate plus the distance d." The schematic diagram in Figure 3.1 may be used for further clarifying.

In Figure 3.6-3.7, the numerical-aperture (NA) dependence of the focused-beam intensity distributions under the previously mentioned aberrations are presented. Figure 3.6a-3.6d illustrate the colour-plots of beam intensity variations, where the vertical and horizontal axes represent the z-position and the distance d, respectively. Under only the effect of spherical aberration, the focused beam profile became more spreading over the z-axis when the distance d increased. By comparing the differences between Figure 3.6a and 3.6b, the added effect of refractive-index birefringence resulted in the position shifts of maximum intensity for the distance greater than approximately 35 μm which corresponded to the plot in Figure 3.5c and 3.6f. Note that the beam intensity in Figure 3.6b seems to be less spreading than that of Figure 3.6a. The same behaviours of maximum split and position shift can be also observed for the simulations using different values of the numerical aperture (NA) i.e. NA = 1.00 and 1.45. In fact, the use of a lower NA of 1.00 tends to produce a narrower intensity profile and less presences of the minor peaks, which can actually be the preferable characteristics of a focused laser distribution for the laser-inscription process if there is no other effect has been considered. To emphasize these different features of beam intensity distributions, Figure 3.7 were plotted with the axial intensity profiles of various simulation conditions but with a fixed distance d of 60 μm which corresponds to the focusing depth (a distance measured from the medium interface and located in the second medium) of roughly 95 μm.

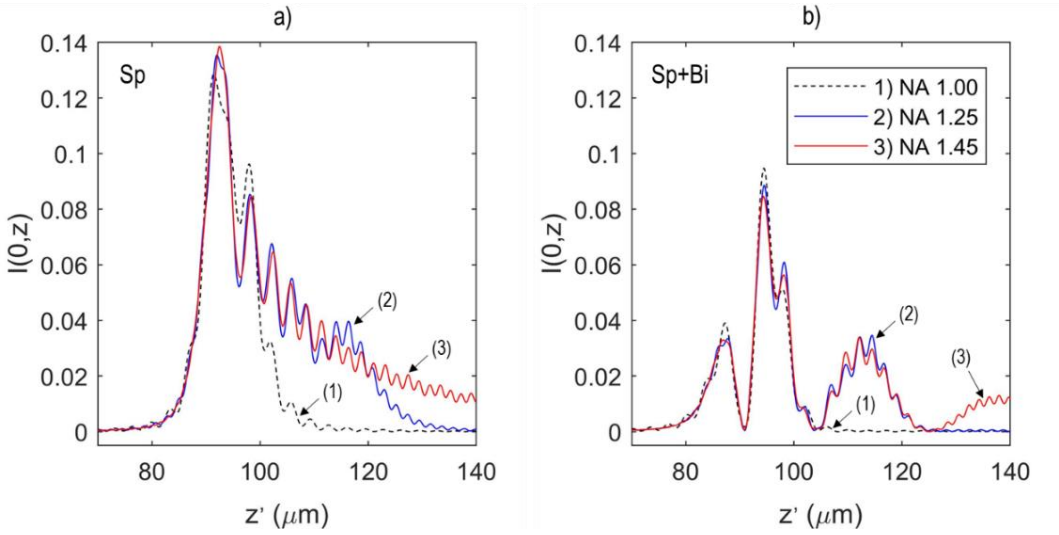

Figure 3.7 The effect of a) spherical aberration only ($n_{2o} = n_{2e} = 2.2166$) and b) the combined effect of spherical aberration and birefringent astigmatism ($n_{2o} = 2.2266, n_{2e} = 2.2066$) on the axial intensity distribution. Three different numerical apertures, i.e. NA = 1.00, 1.25 and 1.45, were used. $\lambda_0 = 790$ nm, $n_1 = 1.518$ and $d = 60$ μm.

Figure 3.6e plots a normalised optical intensity of the maximum peak occurred in the focused beam profile at various distance d and with different NA. All plots show a rapid decreasing inclination at the range of small d, which is followed by a slowly varying trend when the distance d exceeded certain values. The results in Figure 3.6e also show that the use of higher values of NA results in a lower magnitude of the maximum intensity in the focused-beam profile. This can be an important information for the femtosecond-laser inscriptions in adjusting the inscribing pulse power when either the depth of focus or the numerical aperture of a focusing lens was altered.

3.1.4 Effects of the depth of focus

Since it had been already discussed about the theory and computer simulations upon the effects of depth-dependent distortions, this section will demonstrate the impacts of the variation of this focus depth which had been practically observed on the laser-inscribed structures in our experiments. There were three sets of laser-inscribed tracks that were fabricated by three differing levels of pulse energy (E) i.e. 40.9, 45.5 and 54.6 nJ. Each set was comprised of 10 tracks whose setting depths (D_{set}) of inscription were varied from 10 to 100 μm and with an increasing depth step of 10 μm. It should be noted that since the distance between the objective lens and the substrate in our experiment setup was adjusted by a vertical translation stage, the setting depth was analogous to the relative travelling distance of this stage in vertical direction. It should be also mentioned that after the inscriptions the tracks were observed to present at the approximate depths (D_{obs}) between 40 and 174 μm. It could be assumed that this position shift of laser-inscribed structures was stemmed from the beam refractions inside the lithium niobate material

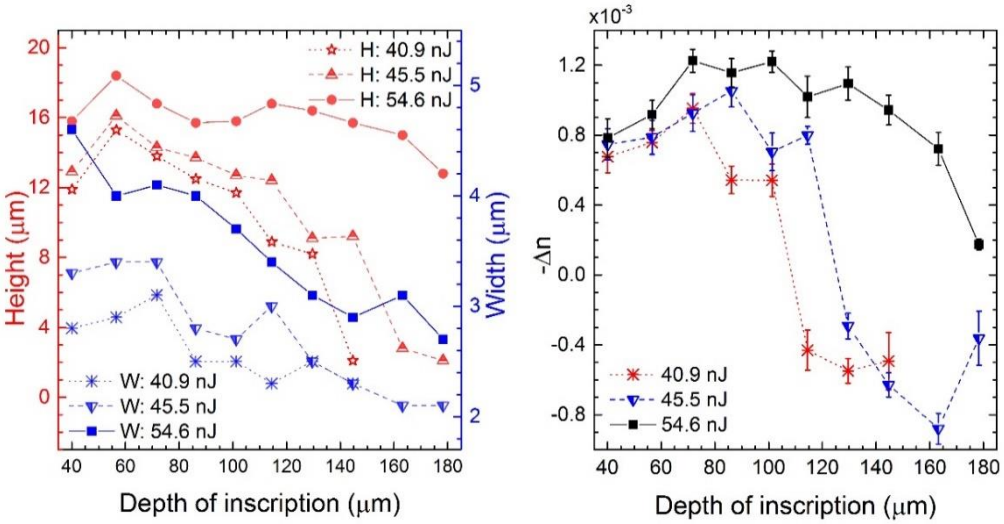

Figure 3.8 Plots of the inscribed track's a) cross-sectional dimensions: height and width versus track's observed depth, and b) negative refractive index contrast $-\Delta n$ versus track's observed depth. The inscription speed was set at 10 mm/s. The inscription direction was toward the $-x$ of crystal. This figure is adapted from [9].

and a non-zero offset of distances between the objective lens and the substrate surface. All straight-line tracks were written by single scan of the laser pulse that translated along the x-axis of the crystal with a constant speed of 10 mm/s.

D_{set} (µm)	10	20	30	40	50
D_{obs} (µm)	≈40	≈57	≈72	≈86	≈99
$E = 40.9$ nJ $P = 0.45$ W	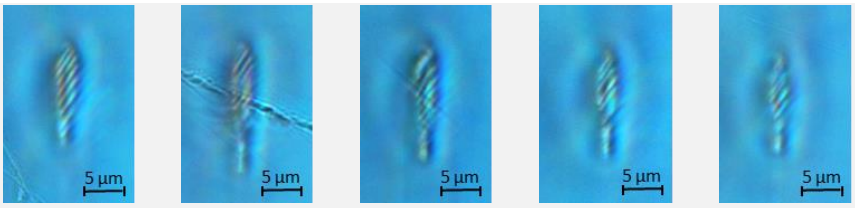				
$E = 45.5$ nJ $P = 0.50$ W	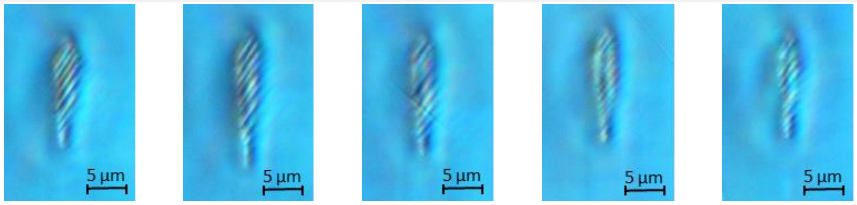				
$E = 54.6$ nJ $P = 0.60$ W	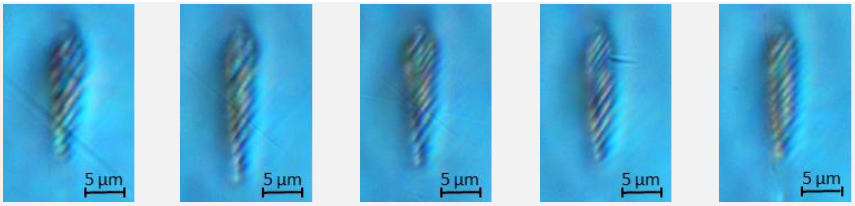				
D_{set} (µm)	60	70	80	90	100
D_{obs} (µm)	≈115	≈129	≈143	≈159	≈174
$E = 40.9$ nJ $P = 0.45$ W	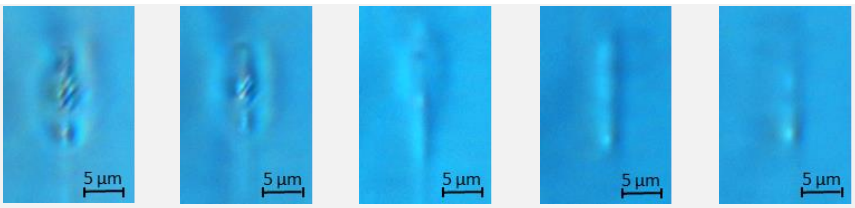				
$E = 45.5$ nJ $P = 0.50$ W	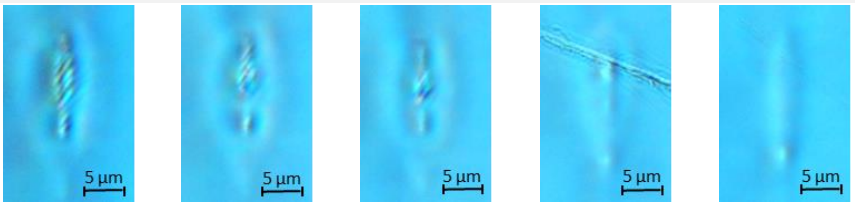				
$E = 54.6$ nJ $P = 0.60$ W	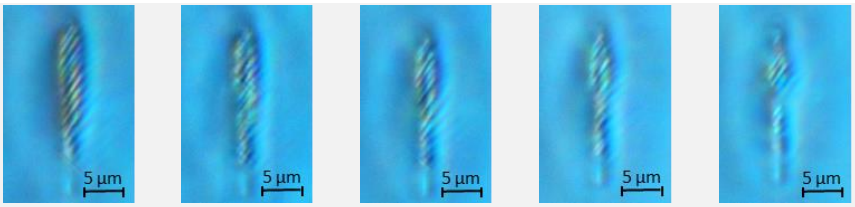				

Figure 3.9 Differential interference contrast (DIC) images of track's cross-sections captured by a light-transmission microscope. The inscription speed was set at 10 mm/s. The inscription direction was toward the $-x$ of crystal.

Figure 3.8 shows the plots of either the cross-sectional dimensions (on the left plots) or the refractive index modification contrast (on the right plots) of the tracks in relations to the inscription depths (D_{obs}). Note that a minus sign in front of Δn denotes the decrease in refractive index with regard to an unmodified area. The cross-sectional heights and widths tended to slightly increase at small depths and then decrease after the depth of around 75 μm with the increasing depth. The similar trend can also be observed for the refractive index changes *(*Δn), but with a deeper tuning point of roughly 80 μm. This behaviour can be simply explained by using the numerical simulations of aberration effects in Figure3.6e which indicate the declines of maximum pulse intensity when the distance or depth of focus increased. The observed increasing trend at the small depth can be presumably caused by the pre-set corrections of a microscope objective lens that could effectively compensated these effects of optical aberrations in this depth range.

Figure 3.9 shows the microscopic images of inscribed track's cross-sections recorded by the differential interference contrast (DIC) technique. The images were captured on a facet, which had been diced and optically polished, of the tested sample. A highly elliptic shape of the laser-modified structures can be clearly observed, and it tended to be elongated in the vertical direction when the focus depth was greater than 115 μm. This behaviour reflects the effects of spherical aberration that was illustrated in the simulation results in Figure 3.5a – 3.5b. A vertical split of the laser-modified areas can be noticed for the low pulse energies i.e. $E = 40.9$ and 45.5 nJ and for the depth D_{obs} greater than 115 μm, which was presumably stemmed from the effect of laser intensity splitting due to the birefringent astigmatism that was previously discussed. It should be mentioned that if compared with a study by Zhou *et al* [8] who used a focusing lens with a numerical aperture (NA) of 1.45 and utilized a linearly-polarised low-repetition-rate pulse laser, the advents of this vertical split of laser-modified structures presented in this study were found at the depths that were 4-5 times greater than that in their report. This might be partially due to the difference in the objective lens NA, which had been found to highly affect the beam focus via the distortions in our simulation study. In addition, it can be seen that when the depth of focus was further increased and exceeded 159 μm the location of a highly modified region (looks like a bright-color dot) was appeared at the bottom of the whole affected area. It is likely that this observed behavior of a laser-modification's relocation can be used to confirm the prediction of the spatial shift of a focused-beam's maximum intensity, which were found from the computer simulations in the Section 3.1.3.

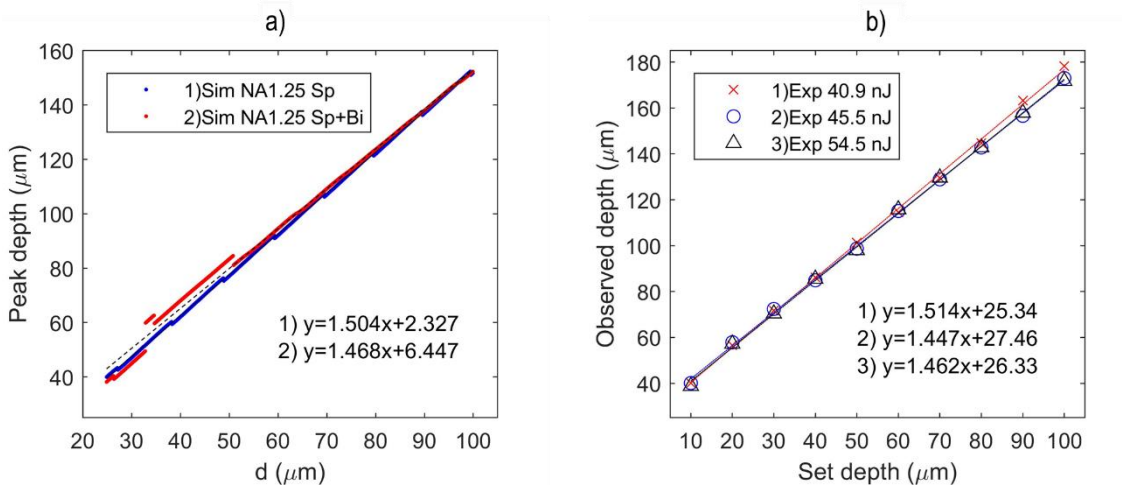

Figure 3.10 Plots of a) the simulation depth of peak intensity versus the distance d, and b) the observed depth of track centre versus the relative translation depth of objective lens. The lines present the linear fitting whose coefficients shown in the inset equations.

The relation between the setting depth (or a distance of vertical stage's translation of focusing objective lens) and the real structure's depth observed after the inscription was also one of the important information required for the optical waveguide fabrications. Figure 3.10b plots the observed depth of tracks written by three different pulse energies as functions of the setting depth. The fitting function showed the linear trends that had the multiplication coefficients of approximately 1.5, which were highly comparable with the fitting coefficients retrieved from the plots of simulation data shown in Figure 3.10a.

The grayscale images in Figure 3.11 show the two-dimensional phase profiles generated by the QPM (Quantitative Phase Microscopy) technique, whose details can be found in the Section 2.5.1. Apart from the calculations of refractive index change (Δn), these phase profiles can also be used for qualitatively observing the smoothness and topography of a laser-modified area by looking from the top-view direction. The dark and bright areas indicated the regions of refractive index decrease and increase, respectively. It can be seen that the tracks consisted of a decreased-index core and the laterally outer areas of refractive index increase. In fact, this region of decreased-index core had been noticed to be narrower when the depth (D_{obs}) increased and was eventually replaced by the bright area of refractive-index increase after exceeded certain depths which related to the inscribing pulse energy (E). These top-view images of tracks could also suggest that the structures were inscribed with the high degrees of smoothness and structural continuity along the writing direction, which can be considered the suitable properties for the fabrication of depressed-refractive-index claddings for an optical waveguide.

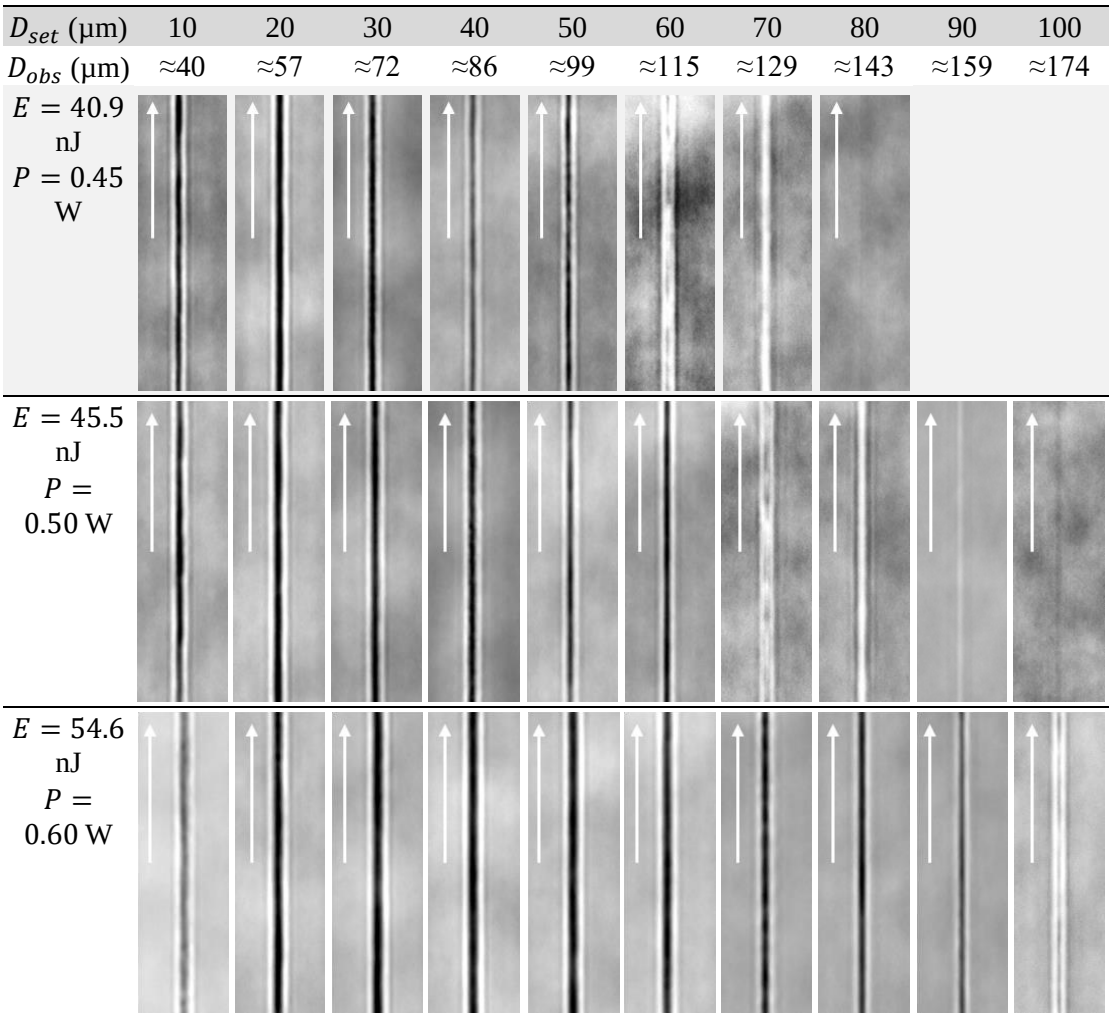

Figure 3.11 Phase profiles of the inscribed tracks, which were evaluated by the IATIA's QPm software mentioned in Chapter 2. The white arrows define the translation direction of laser in regard to the sample. The inscription speed was set at 10 mm/s. The inscription direction was toward the $-x$ of the crystal.

3.2 Total energy deposition of inscribing laser pulses

3.2.1 Effects of the pulse energy variations

The pulse energy, which can be typically approximated by a product of the average of a laser power and the inverse of a pulse repetition rate, is also one of the important factors that dramatically affect the physical and optical properties as well as the shape and dimensions of the region of laser modifications. The use of different levels of pulse energy can result in the different types of laser-matter interaction mechanisms that becomes dominant. The basic principles of these mechanisms and also the key parameters that can be used to justify the transitions between different interaction regimes were previously discussed by using the well-known theories, in the Section 1.1.3. In this section, the influences of pulse energy on the laser-inscribed structures, which had been practically observed on our substrates of lithium niobate wafer, will be presented.

Two sets of laser-written straight tracks were fabricated by writing toward the differing directions, which were toward the crystal's -x and +x directions, along the wafer's crystalline axis. Each set consisted of 11 tracks inscribed by varying the incident pulse energy ranging from 37.1 nJ to 61.8 nJ. The other operational parameters were fixed as the following quantities. A writing speed of 10 mm/s was used for the single-passed scan. The translation stage of an objective lens was vertically located such that the laser spot was focused at an approximate depth of 85 μm below the sample surface. It should be note that this focus depth was chosen because it was approximately the same depth as had been assigned for the centre of a laser-inscribed waveguide structure that will presented in the Chapter 4. In addition, the inscribing beam was adjusted to have a circularly polarised state before it was delivered through the focusing lens. The use of this circularly polarised beam was selected to reduce the direction-dependent effects that have been known to typically occur when an inscribing beam with linear polarisation is utilized.

In Figure 3.12, the plots show the track's cross-sectional sizes (height and width) and the peak-to-peak refractive index contrast (Δn) as functions of the pulse energy (E). It could be presumed that the index change and the pulse energy had a numerical relationship which could be linearly fitted by the following formula:

$$-\Delta n = k(E - E_{th}) \tag{3.16}$$

where k and E_{th} were the fitting coefficients that indicated the increasing rate of negative Δn and the damage threshold energy, respectively. It should be mentioned that a linear relationship -

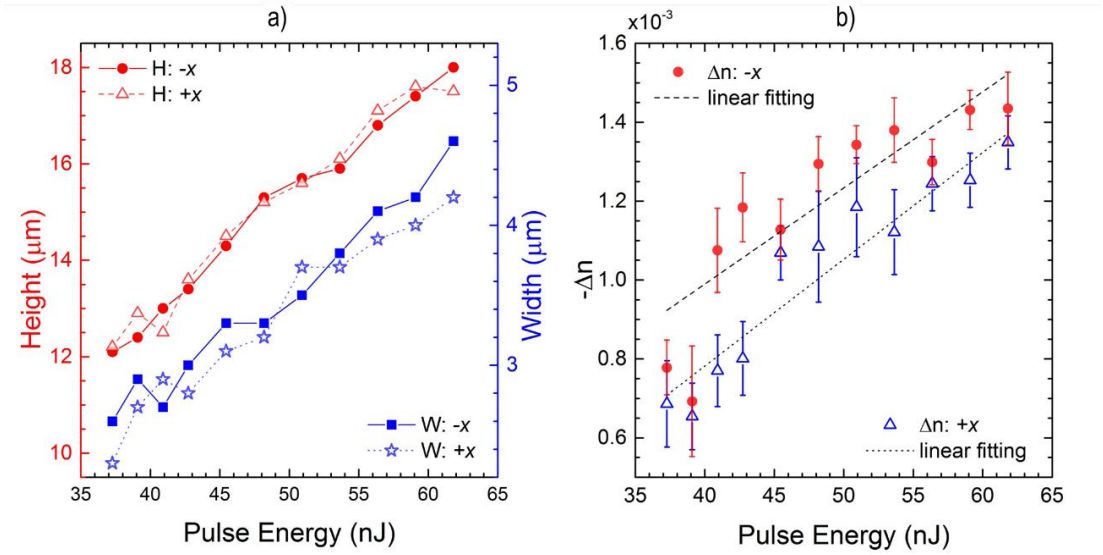

Figure 3.12 Plots of the inscribed track's a) cross-sectional dimensions: height and width versus laser pulse energy, and b) negative refractive index contrast $-\Delta n$ versus laser pulse energy. The inscription speed and the focus depth were set at 10 mm/s and 85 μm, respectively. The inscription directions were toward the $-x$ and $+x$ of crystal. The dashed and dotted lines in b) are the linear fitting of the measured data. This figure is adapted from [9].

between the track's dimensions and the pulse energy could also be observed in Figure 3.12a, but the fitting plots were omitted here.

Table 3.1 Linear fitting coefficients of Equation 3.16 in the plot in Figure 3.12b.

Writing direction	k (nJ^{-1})	E_{th} (nJ)
toward -x	2.71×10^{-2}	11.09
toward +x	2.44×10^{-2}	-0.59

The noticeable differences in the fitting parameters k and E_{th}, shown in the Table 3.1, for the track sets written toward the opposite directions implied that there was a presence of the phenomenon called 'nonreciprocal writing', which had been previously reported by Yang *et al* [10]. In contrasts to our results that showed this nonreciprocal-writing phenomenon for the structures written along the *x*-axis, their study demonstrated the directional dependence of the structural and optical properties for the tracks written along the crystalline *y*-axis only. It should be noticed that the Yang's work utilized a laser system with a low-repetition-rate of $R = 250$ kHz at $\lambda = 1064$ nm for the inscriptions of the micro-structures on a *z*-cut lithium niobate crystal. This differing regime of laser repetition might be presumably the cause for these dissimilar observations.

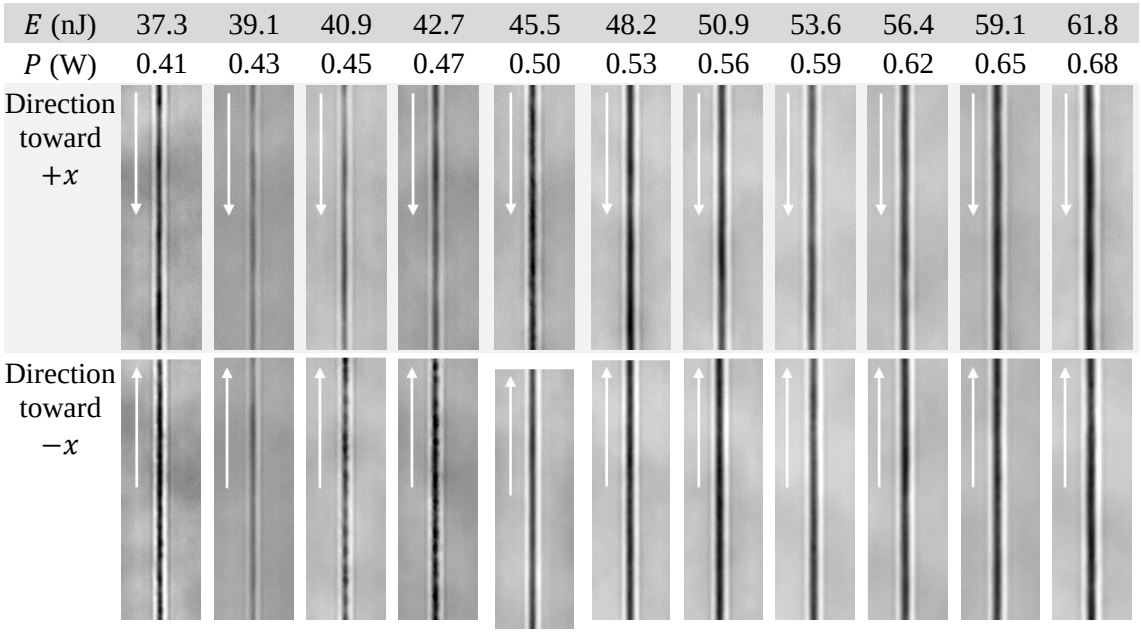

Figure 3.13 Phase profiles of the inscribed tracks, which were evaluated by the IATIA's QPm software mentioned in Chapter 2. The white arrows define the translation direction of laser in regard to the sample. The speed and the focus depth were set at 10 mm/s and 85 μm, respectively.

The effects of nonreciprocal writing can be also observed on the track's appearances which included the longitudinal smoothness, and the cross-sectional micro-structure orientations and dimensions. This mentioned longitudinal smoothness of tracks can be observed from the phase

profiles, obtained by the QPM technique, in Figure 3.13. At the regime of low laser pulse energy ($E < 45.5$ nJ), it can be noticed that the tracks written toward the direction of $+x$ showed the higher longitudinal smoothness than those written toward the $-x$ direction. However, in the regime of high laser pulse energy ($E > 45.5$ nJ), there was no significant difference in regard to the translation directions could be observed from the results. The white arrows in the figures indicate the writing directions of track structures.

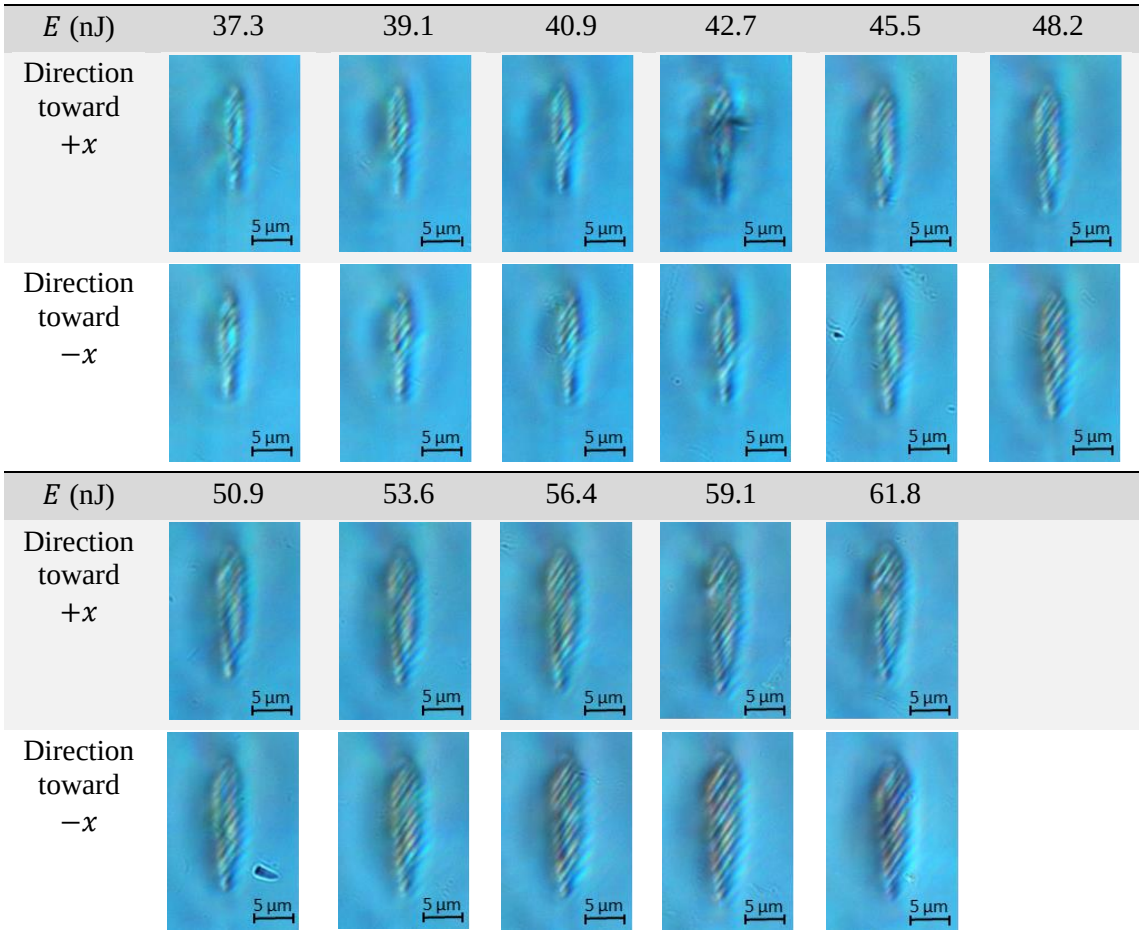

Figure 3.14 DIC images of track's cross-sections captured by a light-transmission microscope. The inscription speed and the focus depth were set at 10 mm/s and 85 µm, respectively.

The microscopic images of track's cross-section, which were recorded by the differential interference contrast (DIC) technique, were shown in Figure 3.14. The micro-grating-like structures or the so-called 'quill pen' can be observed in our fabricated structures. This quill pen was suggested to originate from the effect of a tilted laser front that causes an an-isotropic trapping of electron plasma during the laser interactions [11]. The average values of the cross-sectional height-to-width ratios were approximately 4.4 and 4.6 for the $-x$ and $+x$ writing directions, respectively. In addition, it was found that these ratios were decreasing when the amount of pulse energy of an inscribing laser increased. In fact, this behaviour of the lateral expansion of a laser-

modified region, which closely correlated to the laser fluence, is one of the important characteristics of a femtosecond-laser inscription in a regime of heat accumulations.

3.2.2 Effects of the inscription-stage translation speeds

In addition to the laser pulse energy, the speed of stage's translation is also a crucial factor that affects the total energy deposition of an inscribing laser which consequently influence the physical and optical properties of a laser-written structure. In our experiment, it was found that the uses of too high writing speeds could result in a weak and non-homogenous region of laser modifications. In contrast, the uses of too slow writing speeds can typically lead to a high number of structural defects being observed, and a prolonged time duration of a whole inscription process. In this section, a study of the writing speed effects from two sets of straight track structures written in the opposite directions along the *x*-axis of lithium niobate crystal will be presented. The range of translation speed was ranged from 1 mm/s to 30 mm/s. The pulse energy and the focus depth were fixed at 45.5 nJ and 85 µm, respectively.

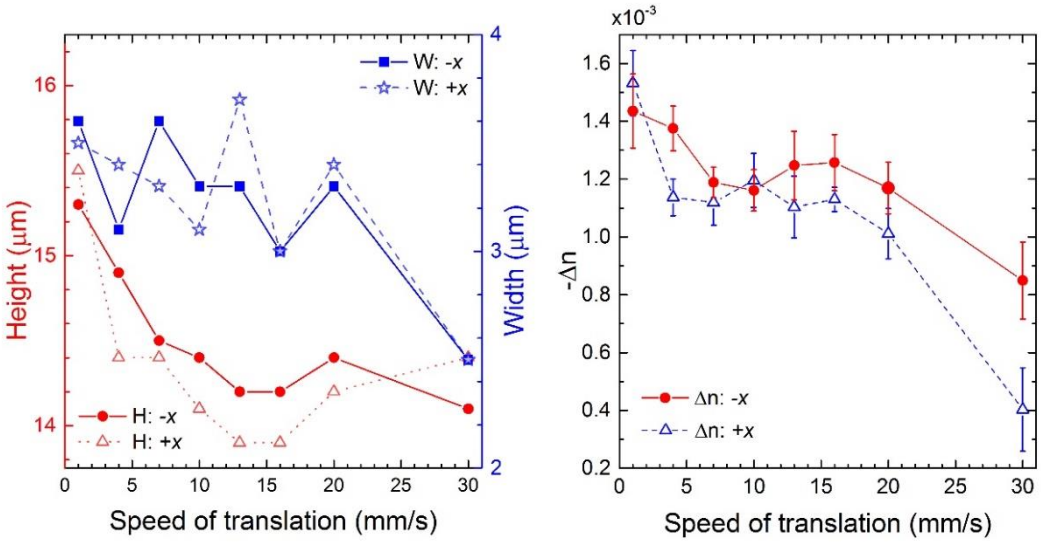

Figure 3.15 Plots of the inscribed track's a) cross-sectional dimensions: height and width versus translation speed, and b) negative refractive index contrast $-\Delta n$ versus the translation speed. The laser pulse energy and the focus depth were set at 45.5 nJ and 85 µm, respectively. The inscription directions toward the $-x$ and $+x$ of crystal. This figure is adapted from [9].

The plots in Figure 3.15 show the experimental results of the writing-speed variation tests. The left and right diagrams present the cross-sectional dimensions (height and width) and the refractive index modification (Δn) of the inscribed tracks as functions of the speed of stage translation, respectively. It can be noticed that the data plotted in both diagrams had a decreasing trend when the writing speed increased, except in a speed range between 5 mm/s and 20 mm/s. In this range of inscription speed, the properties of modification regions remained relatively un-changing compared to other speed regimes. These observed trends of data suggested that the laser-

material interactions of heat-accumulation likely occurred in this speed regime, in which the femtosecond-laser modifications were insensitive upon the speed of laser-pulse travelling.

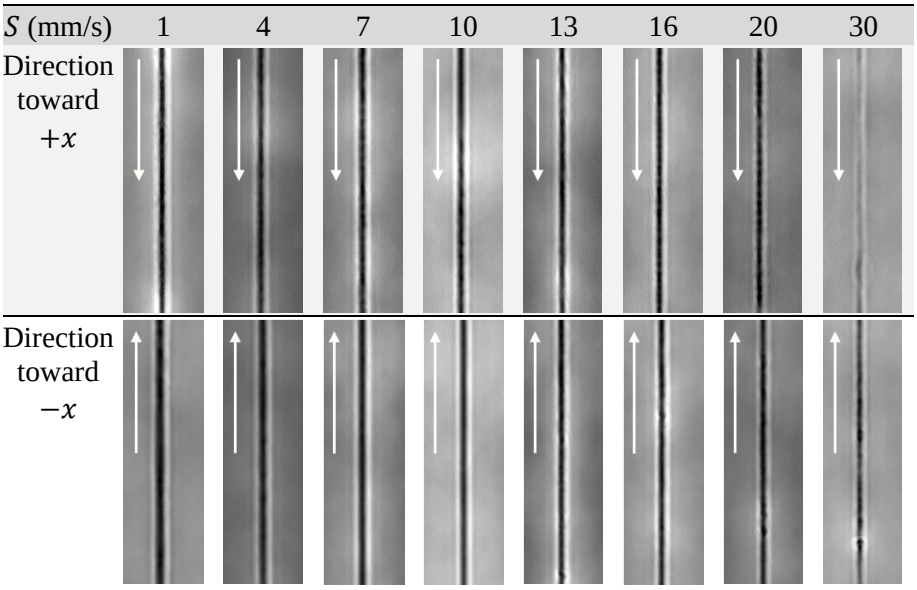

Figure 3.16 Phase profiles of the inscribed tracks, which were evaluated by the QPm software mentioned in Chapter 2. The white arrows define the translation direction of laser in regard to the sample. The pulse energy and the focus depth were set at 45.5 nJ and 85 μm, respectively.

The phase profiles, obtained by the QPM technique, of tracks inscribed by various speeds of writing were presented in Figure 3.16. It can be clearly seen that the thickness of refractive-index decrease (dark-colour areas) enlarged when the translation speed reduced. For the high writing-speed regime ($S > 13$ mm/s), some periodically uneven features can be observed on the lateral bright regions of refractive index increase. This kind of structural inhomogeneity could be presumably stemmed from the instability of laser-matter interactions that occurred in the vicinity of a laser focal volume. For the low writing-speed regime ($S < 13$ mm/s), the tracks written in the direction toward the *-x* direction of a lithium niobate crystal were found to have a higher degree of structural smoothness than that of the opposite direction. Also, it can be noticed in the cross-sectional DIC images in Figure 3.17 that the structures fabricated by low-speed writing tended to have some kinds of stress-field induced defects, which were seen as a dark short stripe surrounded the inscribed structures. In fact, the inscription speed of 10 mm/s was found to be the optimum condition for the laser inscription of a straight-line track that could achieved both high longitudinal smoothness and high index changes. Hence, this writing speed of 10 mm/s had been used for the fabrications of low-loss optical waveguides that will be later presented in the Chapter 4 and 5. Note that the white arrows in the figures indicate the writing directions of track structures.

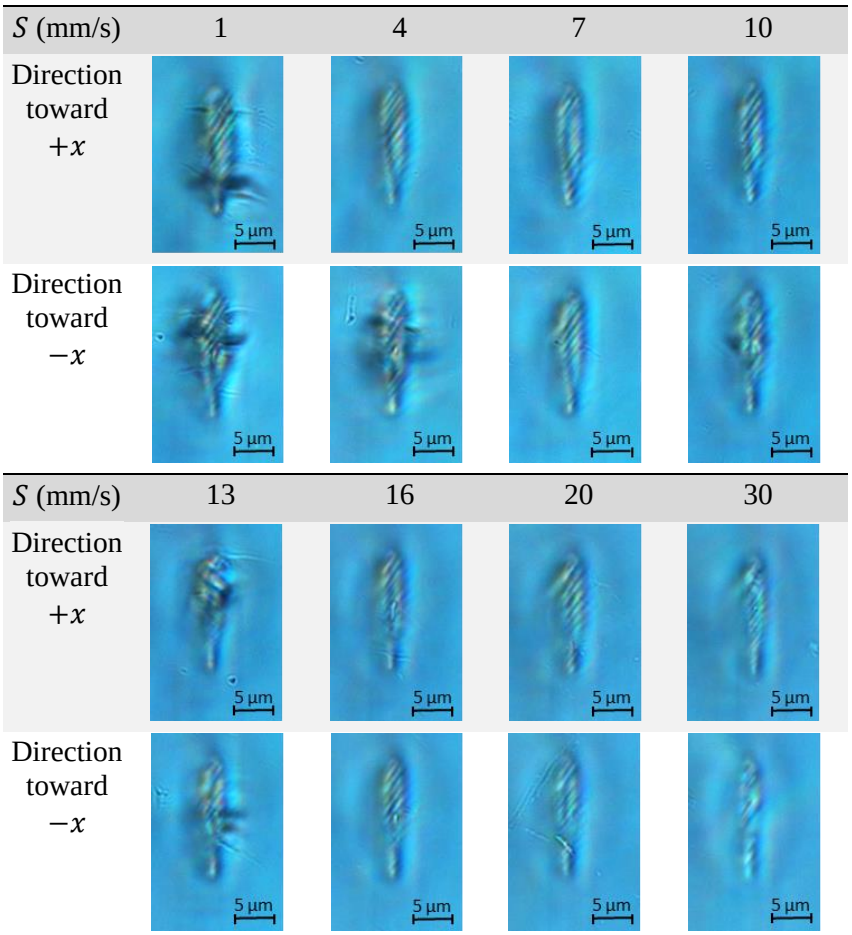

Figure 3.17 DIC images of track's cross-sections captured by a light-transmission microscope. The laser pulse energy and the focus depth were set at 45.5 nJ and 85 µm, respectively.

3.3 Post-processing method of thermal annealing treatments

To investigate the impacts of thermal annealing on the laser-inscribed structures, a series of thermal annealing treatments were performed on our samples of lithium niobate in an open-air furnace. There were six temperatures, including 250, 350, 500, 700, 850 and 950 °C, of annealing that had been processed by an incremental order. After each stage of heat treatments was completed, the samples were thoroughly characterised on the variations of optical and physical properties. The duration of thermal annealing per a temperature was lasted for 3 hours which excluded the heating-up and cooling-down processes. The rate of heating and cooling were set at approximately 1 °C/s and 3 °C/s, respectively. The tested tracks were the same sets that were used in the Section 3.2.1, in which the two sets of tracks were written in the -*x* and +*x* directions and each set consisted of 11 tracks of varying pulse energies ranging from 37.1 nJ to 61.8 nJ. The writing speed of 10 mm/s was used for the single-passed scan, and the depth of focus was at approximately 85 µm. The technical specifications of the heating furnace used in this work can be found in the Section 2.4.2.

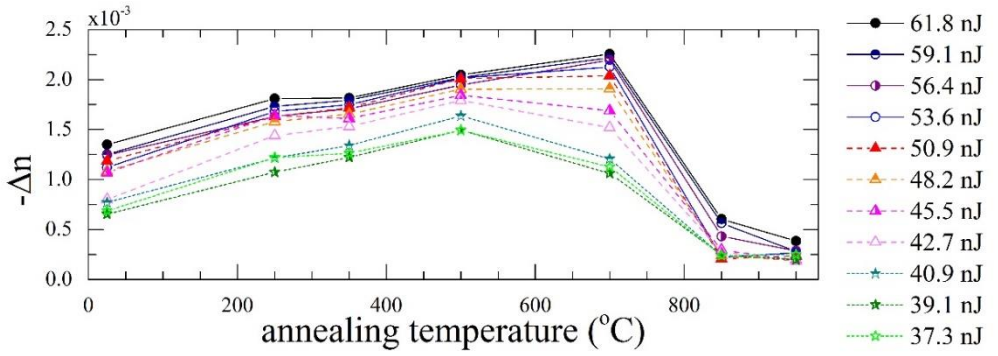

Figure 3.18 Effects of the thermal annealing on the refractive index contrast (Δn) of the tracks inscribed by various pulse energies. The tracks were written along the x-axis (toward the $-x$ direction) with the translation speed of 10 mm/s. The depth of inscription was at around 85 μm beneath the surface. This figure is adapted from [9].

In Figure 3.18, it was found that the trends of refractive index contrast (Δn) regarding the applied annealing temperatures were sensitive to the pulse fluences being used for the laser inscriptions. For the inscriptions with low pulse energies (< 53 nJ) which were represented by the dashed and dotted lines, the refractive index contrast (Δn) increased with the temperature of annealing in the range between 250 and 500 °C. Then, the refractive index change became reduced till the last temperature of testing. For the inscriptions with high pulse energies (> 53 nJ) which were represented by the solid lines, the increasing trends of index contrast can be observed till the higher annealing temperature of 700 °C. The measured Δn then dropped in the last two testing temperatures. These results suggested that the effective refractive index modifications (Δn) which were induced by the pulse laser of our setup could be enhanced up to 2-3 times depending on the temperature of annealing. In addition, the thermal stability of an inscribed structure could be significantly improved by the increase of an inscribing pulse energy. In Figure 3.19 and 3.20, the microscopic images of track cross-sections were presented for each stage of heat treatments. It can be noticed that the stress fields around the track surrounding were reduced by heats and were likely vanished after the temperature of around 350 °C, which could be a reason of the increase of the measured refractive index contrast. The overall appearances of the inscribed tracks had become noticeably changed when the temperature reached at 700 °C. Then, the tracks can be observed to be partially erased after the final temperature of 950 °C. It should be noted the melting temperature and the Curie temperature for the phase transition (from the ferroelectric to paraelectric phases) of a lithium niobate are at 1140 and 1250 °C, respectively. Compared to the previous studies by Nguyen *et al* [12] who used the femtosecond-laser pulses in a low-repetition-rate regime, our results have shown a significant improvement in the thermal stability of a laser-written structure. Although these is not yet an explicit explanation about the nature of laser-material modifications in this regime of heat accumulation being reported, our experimental results had provided a clue suggesting that this mechanism could be possibly related to the hardly reversible processes e.g. chemical composition shift, crystallization, amorphization and so forth.

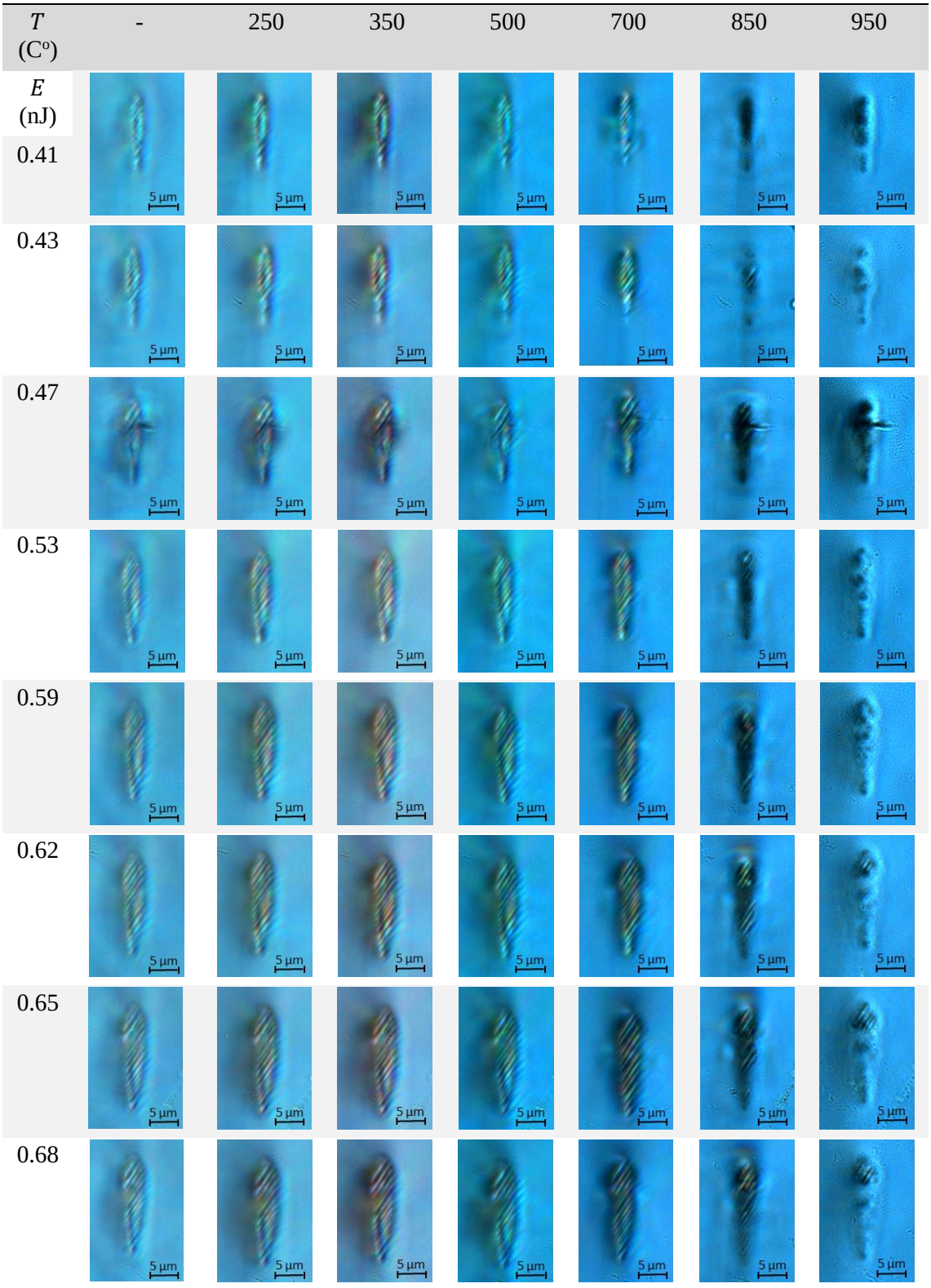

Figure 3.19 Differential interference contrast (DIC) images of track's cross-sections captured by a light-transmission microscope. The images were captured before and after each step of heat treatments. The inscription speed and the focus depth were set at 10 mm/s and 85 µm, respectively. **The inscription direction was toward the $-x$ of crystal.**

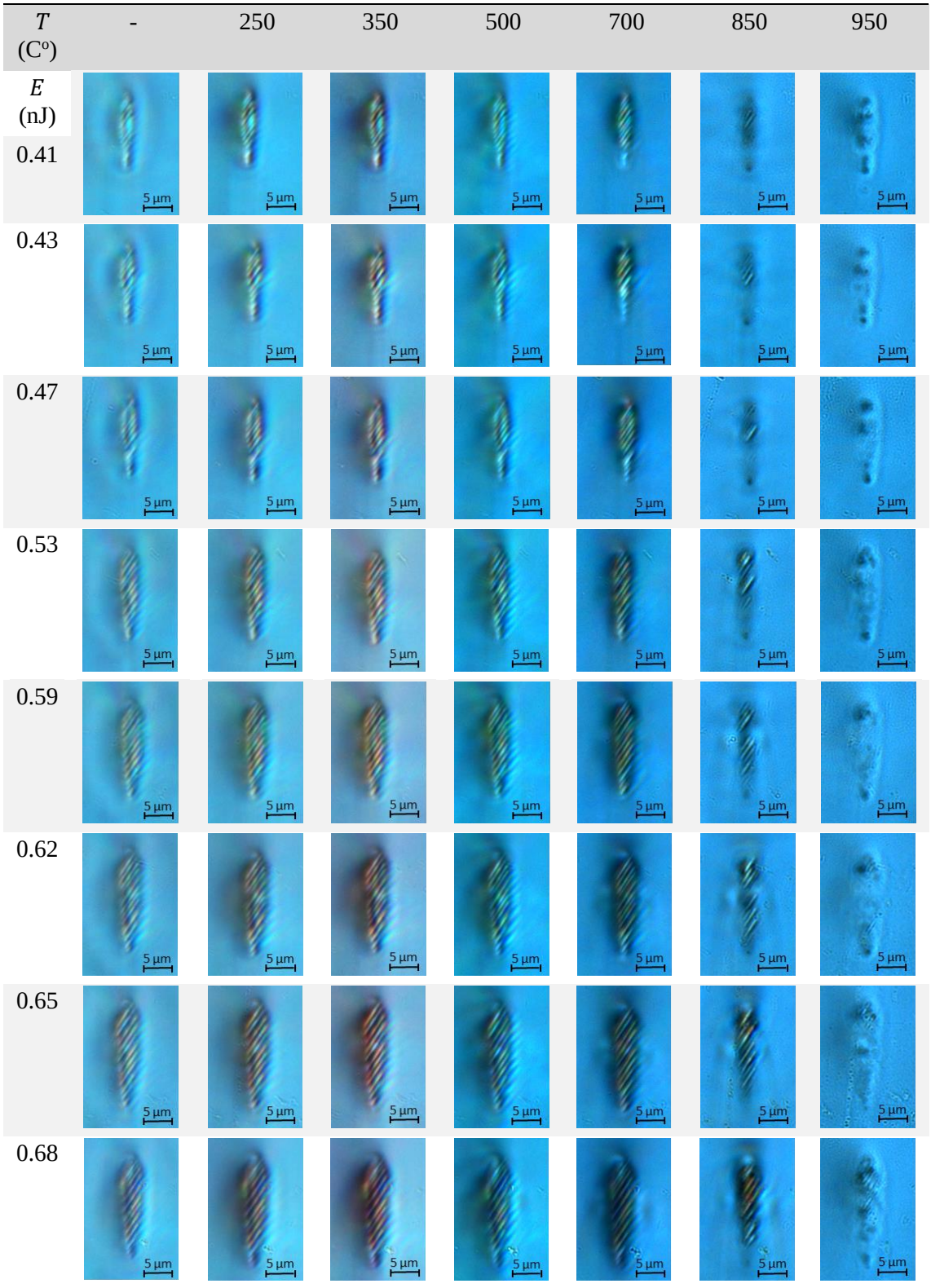

Figure 3.20 Differential interference contrast (DIC) images of track's cross-sections captured by a light-transmission microscope. The images were captured before and after each step of heat treatments. The inscription speed and the focus depth were set at 10 mm/s and 85 µm, respectively. **The inscription direction was toward the $+x$ of crystal.**

Discussions and summary

In this chapter, our numerical and experimental results which had focused on the three important factors that affected the physical and optical properties of a laser-inscribed structure on a sample of lithium niobate crystal have been presented. The discussed factors included the optical distortions of a beam focus, the total energy deposition of inscribing laser pulses, and the post-processing method of thermal annealing treatments.

Two optical distortions, i.e. spherical aberration and birefringent-astigmatism aberration, that have been well-known to be highly problematic for a femto-second laser inscription process were discussed based on the numerical derivation of extended integral representation of light wave diffractions. The mathematic equations were presented and were applied for the computer simulations in a Matlab software to obtain the optical intensity profiles of a beam focus under these mentioned distortion effects. The computational results showed that the spherical aberration which was stemmed from the refractive index mismatch resulted in the elongation of a beam focus toward the beam propagation direction. In addition, this elongation of beam intensity profile had caused the degradations of intensity maximum which were more severely noticed when the distance of focusing increased. Also, the simulations of optical astigmatism effects caused by the refractive index birefringence of a lithium niobate crystal had shown the phenomena of an intensity-profile split and a position shift of intensity maximum, which had been found to be sensitive to the focus distance and the numerical aperture (NA) of a focusing objective lens. The experimental results also showed the focusing-distance-dependent properties of a laser-inscribed track structure. The data of cross-sectional sizes and refractive index modifications had the decreasing trends when the depth or distance of focus increased. The cross-sectional shape of an inscribed track was found to be highly elliptic with a height-to-width ratio of approximately 4.4-4.6. The vertical splits of laser-modified regions were observed when the depth was greater than 115 μm and the inscribing pulse energy was in the range between 40.9 and 45.5 nJ. These results of experiments and simulations had shown significant correlations, which can be further applied for the fabrication of optical guiding structures.

The total energy deposition of an inscribing beam, which were closely related to the inscription parameters of laser pulse energy and writing speed, had been discussed for the practical impacts on a laser-modified region on our sample of lithium niobite. The cross-sectional dimensions including height and width, and the total refraction index contrast of the laser-written tracks had been found to be linearly proportional to the pulse energy of an incident beam. The coefficients from the linear-fitting functions suggested the behavior of writing-direction dependences on the laser-inscribed structures in our study. This non-reciprocal writing properties had been also observed in the top-view and cross-sectional profiles of a straight-line track

inscribed along an *x*-axis of the crystal, which had not yet been reported in any other literature. A study of the writing-speed variations showed that the track's properties were highly sensitive to the inscription-stage translation in the regimes of low (< 13 mm/s) and high (> 13 mm/s) speeds. The uses of low speed resulted in the larger dimension of modified regions and the higher refractive index change, but the structures were occupied with a higher degree of stress-induced defects. On the other hands, the uses of high writing speed resulted in low refractive-index modification and low laser-induced stress, but there were some kinds of periodic inhomogeneity occurred along the tracks. In fact, the optimum speed of approximately 10 mm/s was found to suitable for the fabrications of our optical waveguide structures, in terms of both high uniformity and less structural defects.

The effects of post-processing treatments of thermal annealing on the laser-written structures were investigated in a temperature range between 250 to 950 ^{o}C within a time duration of 3 hours per each temperature. The results showed a significant enhancement of overall refractive index contrast after the structures were thermally treated up to the temperature of 500 ^{o}C. After the temperature exceeded this value, the refractive index changes declined with the increasing temperature. The uses of higher pulse energy tended to produce the structures with the greater thermal stability. The microscopic images of track's cross-sections after each stage of thermal annealing were presented, which benefitted in visualizing the physical deformations of a laser-induced structure under the treatments of heat. It had been observed that the stress fields surrounded the laser-inscribed tracks were vanished after the annealing at 350 ^{o}C, and the areas of laser modification started to be diminished after the temperature of 850 ^{o}C. In fact, this property of high thermal stability was found to be unique for the inscription of laser pulses with a high repetition rate that caused the strong laser-matter interaction in the heat accumulative regime, which can be highly useful for manufacturing the optical devices that require a high temperature resistance such as harsh-environment sensors, high power laser applications and so forth.

In the future works, the operation parameters including pulse energy, writing speed, focus depth and annealing temperature being assigned for the laser-inscription process can be further extended to cover a wider parameter range and varied by a narrower variation step in order to improve the comprehensiveness and precision, respectively, of the experiment studies that had been done in this chapter. In addition, the other relevant parameters such as laser polarisations state and focusing objective specifications can be also included to investigate their effects on the laser-inscribed structures. More sample characterization techniques like Raman spectroscopy and Fluorescence imaging [13] can be utilized for the detailed analysis of the material modifications caused by the laser pulses. The advance techniques, e.g. refractive near-field (RNF) [14] and micro-reflectivity [15] methods, for the acquisition of a refractive index change can be applied to improve the accuracy and resolution of the experiment data.

References

[1] P. Török, P. Varga, Z. Laczik, and G. R. Booker, "Electromagnetic diffraction of light focused through a planar interface between materials of mismatched refractive indices: an integral representation," *J. Opt. Soc. Am. A, JOSAA*, vol. 12, no. 2, pp. 325–332, Feb. 1995, doi: 10.1364/JOSAA.12.000325.

[2] C. J. R. Sheppard and P. Török, "Effects of specimen refractive index on confocal imaging," *Journal of Microscopy*, vol. 185, no. 3, pp. 366–374, Mar. 1997, doi: 10.1046/j.1365-2818.1997.d01-627.x.

[3] P. Török, "Focusing of electromagnetic waves through a dielectric interface by lenses of finite Fresnel number," *Journal of the Optical Society of America A*, vol. 15, no. 12, p. 3009, Dec. 1998, doi: 10.1364/JOSAA.15.003009.

[4] E. Wolf, "Electromagnetic diffraction in optical systems - I. An integral representation of the image field," *Proceedings of the Royal Society of London. Series A. Mathematical and Physical Sciences*, vol. 253, no. 1274, pp. 349–357, Dec. 1959, doi: 10.1098/rspa.1959.0199.

[5] A. Marcinkevičius, V. Mizeikis, S. Juodkazis, S. Matsuo, and H. Misawa, "Effect of refractive index-mismatch on laser microfabrication in silica glass," *Appl Phys A*, vol. 76, no. 2, pp. 257–260, Feb. 2003, doi: 10.1007/s00339-002-1447-z.

[6] M. Gu, D. Day, O. Nakamura, and S. Kawata, "Three-dimensional coherent transfer function for reflection confocal microscopy in the presence of refractive-index mismatch," *Journal of the Optical Society of America A*, vol. 18, no. 8, p. 2002, Aug. 2001, doi: 10.1364/JOSAA.18.002002.

[7] D. E. Zelmon, D. L. Small, and D. Jundt, "Infrared corrected Sellmeier coefficients for congruently grown lithium niobate and 5 mol. % magnesium oxide–doped lithium niobate," *J. Opt. Soc. Am. B, JOSAB*, vol. 14, no. 12, pp. 3319–3322, Dec. 1997, doi: 10.1364/JOSAB.14.003319.

[8] G. Zhou *et al.*, "Axial birefringence induced focus splitting in lithium niobate," *Opt. Express, OE*, vol. 17, no. 20, pp. 17970–17975, Sep. 2009, doi: 10.1364/OE.17.017970.

[9] T. Piromjitpong, M. Dubov, and S. Boscolo, "High-repetition-rate femtosecond-laser inscription of low-loss thermally stable waveguides in lithium niobate," *Appl. Phys. A*, vol. 125, no. 5, p. 302, Apr. 2019, doi: 10.1007/s00339-019-2609-6.

[10] W. Yang, P. G. Kazansky, and Y. P. Svirko, "Non-reciprocal ultrafast laser writing," *Nature Photonics*, vol. 2, no. 2, pp. 99–104, Feb. 2008, doi: 10.1038/nphoton.2007.276.

[11] P. G. Kazansky *et al.*, "'Quill' writing with ultrashort light pulses in transparent materials," *Appl. Phys. Lett.*, vol. 90, no. 15, p. 151120, Apr. 2007, doi: 10.1063/1.2722240.

[12] H.-D. Nguyen *et al.*, "Low-loss 3D-laser-written mid-infrared $LiNbO_3$ depressed-index cladding waveguides for both TE and TM polarizations," *Opt. Express, OE*, vol. 25, no. 4, pp. 3722–3736, Feb. 2017, doi: 10.1364/OE.25.003722.

[13] W. J. Reichman, J. W. Chan, C. W. Smelser, S. J. Mihailov, and D. M. Krol, "Spectroscopic characterization of different femtosecond laser modification regimes in fused silica," *J. Opt. Soc. Am. B, JOSAB*, vol. 24, no. 7, pp. 1627–1632, Jul. 2007, doi: 10.1364/JOSAB.24.001627.

[14] S. M. Eaton *et al.*, "Transition from thermal diffusion to heat accumulation in high repetition rate femtosecond laser writing of buried optical waveguides," *Opt. Express, OE*, vol. 16, no. 13, pp. 9443–9458, Jun. 2008, doi: 10.1364/OE.16.009443.

[15] Y. Youk and D. Y. Kim, "Reflection-type confocal refractive index profile measurement method for optical waveguides: Effects of a broadband light source and multireflected lights," *Optics Communications*, vol. 277, no. 1, pp. 74–79, 2007, doi: 10.1016/j.optcom.2007.04.029.

Chapter 4

Fs-laser Inscriptions of Optical-lattice-like Waveguides

The aims of this chapter were to investigate for a set of optimum parameters, which involved the waveguide's cross-sectional geometry and the operational conditions, that could be used in the femto-second laser inscriptions of a low loss guiding structure. The waveguide's type and cross-sectional geometry that were of interest were the depressed-cladding type and the optical-lattice-like structure, respectively. In general, this kind of waveguide configuration consists of several damaged tracks arranged in a multi-layer hexagonal packing. The adjacent tracks are separated by an equal spacing, and some inner-track's positions are left un-exposed to the laser pulses to create a core region where the light beam can propagate through. Compared to other depressed cladding configurations such as circular or rectangular ring(s), this hexagonal optical-lattice-like packing have shown benefits on the thicker area of cladding with the same (or less) number of written tracks. In fact, it was recently demonstrated by Karakuzu *et al* [1], [2] by the numerical simulations that this type of waveguide packing could possibly offer a significantly low loss over a broad range of spectrum, particularly, on a substrate of lithium niobate.

This chapter consists of 5 sections, where the first section will be about the computer simulation of waveguides and the rest sections will mention about the experiments of femto-second laser writing of waveguides. In the ***Section 4.1***, the Comsol Multiphysics software was used for investigating a suitable waveguide geometry that was later applied in the fabrication process. The study focused on optimizing three parameters which were a width of waveguide's core, a separation between adjacent tracks (a_s) and number of cladding layers. The ***Section 4.2*** will mention about the strategies used in the laser inscription processes of our waveguides. |The operational parameters implemented for different waveguide groups will be described. Also, this section will define the schemes of pulse-energy variation which were initially aimed for recompensing the effect of optical aberrations. Optical characteristics of the fabricated waveguide structures, before the thermal annealing treatments, will be presented in the ***Section 4.3***. The results demonstrate the relationship between the inscribing pulse energy and the guiding properties which included a propagation loss and a mode field diameter (MFD). The influences of different energy variations on the near-field intensity distributions will be revealed. The ***Section 4.4*** will report on the impacts of thermal annealing on the waveguide's guiding characteristics. The annealing processes had been done at 6 temperatures ranging from 250 ^{o}C to 950 ^{o}C for the time duration of 3 hours per temperature.

4.1 Computer simulations of an optical waveguide with a cross-sectional geometry of the optical-lattice-like packing

This section presents our results of the computer simulations that were used to investigate and optimize the packing geometry and the relevant parameters for the fabrication processes of a depressed-cladding waveguide, which will be demonstrated in the Section 4.2 – 4.4. An example of the cross-sectional arrangement of laser-inscribed tracks for a waveguide written in an optical-lattice-like geometry can be visualised in Figure 4.1a. The track arrangement, presented here, consists of 4 layers of hexagonal rings which contains a total number of elliptic-shape tracks of 84 tracks. In the diagram, the spacing between the adjacent tracks was denoted by a_s. Two circular domains of diameters W_1 and W_2 represent the computer-simulation areas of un-modified material with the refractive indices n_1 and n_3, respectively. For our simulations, the Sellmeier's equation was applied for approximating the wavelength-dependent refractive index of an un-modified lithium niobate (n_1). The index n_3 was a complex refractive index, which contained

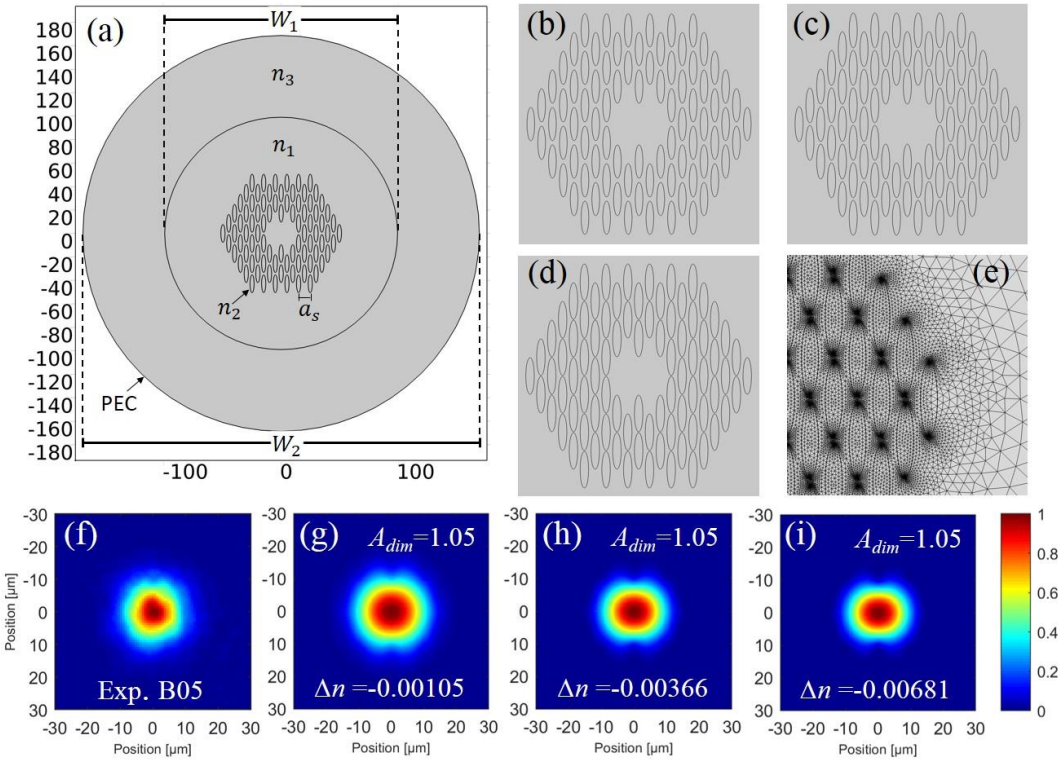

Figure 4.1 Simulation geometries, used in a Comsol Multiphysics software, of a) the entire simulation domain and the waveguide's cladding domain of the simulation conditions with b) $A_{dim} = 1.00$, c) $A_{dim} = 1.05$ and d) $A_{dim} = 1.10$. e) Shows the Free-Triangular mesh (extra-fine sizes) used in the finite-element method (electro-magnetic waves, frequency domain interface). The mode intensity distribution of f) the experimental result from B05 waveguide and the simulation result with the conditions $A_{dim} = 1.05$ and g) $\Delta n = -0.00105$, h) $\Delta n = -0.00366$ and i) $\Delta n = -0.00681$. The outer domain's boundary was applied with a Perfect Electric Conductor (PEC) boundary condition. The testing wavelength was at 1550 nm.

the real part that equalled n_1 and the imaginary part that increased with the radial distance. In fact, the imaginary part of this n_3 was properly adjusted for attenuating an electric field distributed nearby the outer boundary, which could cause the scattering effects. Also, the outer boundary of the simulation-domain had been set to have the properties of the perfect electric conductor (PEC) that could absorb the incoming normal e-field. The n_2 was the refractive index of the laser-modified regions, which were represented by the ellipses in Figure 4.1a. This refractive index n_2 was simply calculated by adding the refractive index n_1 by the assigned value of a refractive index contrast (Δn), which was $n_2 = n_1 + \Delta n$. The dimensions including height (h_{sim}) and width (w_{sim}) of an ellipse in the simulations were set by applying the observed values of track's cross-section from the experiment in the Chapter 3, which were $h_{exp} = 15.18$ µm and $w_{exp} = 3.54$ µm. The multiplication coefficient A_{dim} was used for alternating these parameters in the simulations. Figure 4.1b – 4.1d illustrate the waveguide geometries generated by the different values of a coefficients $A_{dim} = 1.00, 1.05$ and 1.10. Figure 4.1e depicts an example of the Free-Triangular mesh with an adaptive arrangement of nodes.

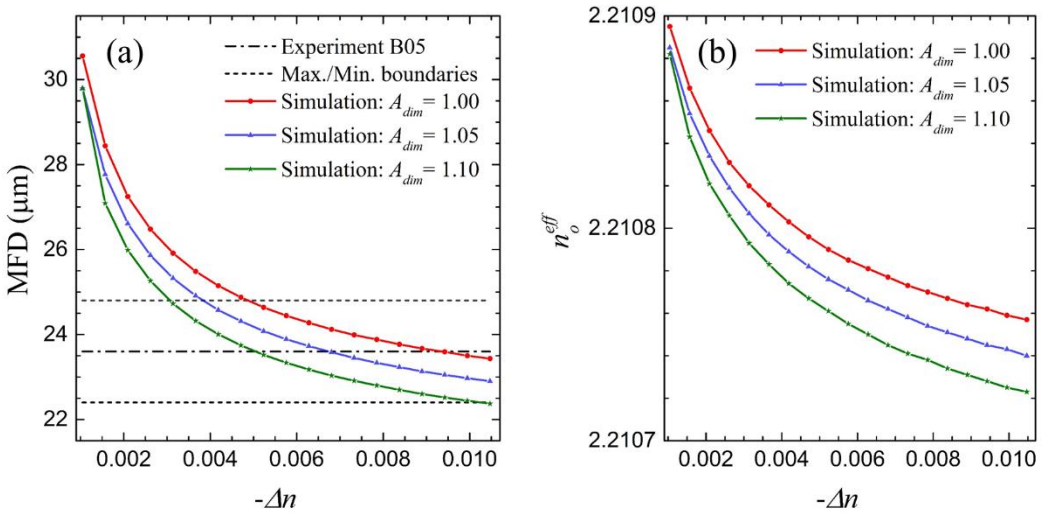

Figure 4.2 Computer simulation results show the characteristics of propagation modes in TE polarisation i.e. plots of a) the mode-field-diameter (MFD) and b) the effective mode refractive index (n_o^{eff}) versus the change of refractive index (Δn) in the areas of ellipse tracks. The testing wavelength was at 1550 nm.

The simulations had been done in a Comsol Multiphysics software that utilized the finite element method and the computational interface of electro-magnetic waves and frequency domain. For a testing wavelength of 1550 nm, the plots in Figure 4.2a show the simulation results of a mode-field-diameter (MFD) of the guiding modes using various values of A_{dim} as a function of the refractive index contrast (Δn). It was found that the MFD exponentially decreased with the increasing value of Δn. Also, the increase of track sizes by the coefficient A_{dim} resulted in the reduction of the MFD. These results simply suggested that the light confinement can become

stronger when the refractive index contrast between the waveguide's core and cladding was greater, and when the depressed-cladding zone was closely packed. The dashed-with-dotted line in Figure 4.2a indicates the experiment value of MFD which had been measured from a laser-inscribed waveguide B05. The details of this B05 waveguide will be later described in the section 4.2. The region between the dotted lines represent the boundary of measurement's standard deviations (SD). By using these data of computational and experimental MFD, the effective refractive index contrast (Δn) of this B05 waveguide structure could be estimated to be -0.0068, says for the $A_{dim} = 1.05$. In addition, the mode-field intensity distributions measured from the waveguide B05 presented in Figure 4.1f had shown a good agreement with the simulation intensity profile in Figure 4.1i that used the simulation parameters of $\Delta n = -0.00681$, $A_{dim} = 1.05$ and $a_s = 9.9$ μm. Also, Figure 4.2b had shown the possible range of an effective refractive index for the single-mode excitations as the functions of a refractive index contrast Δn.

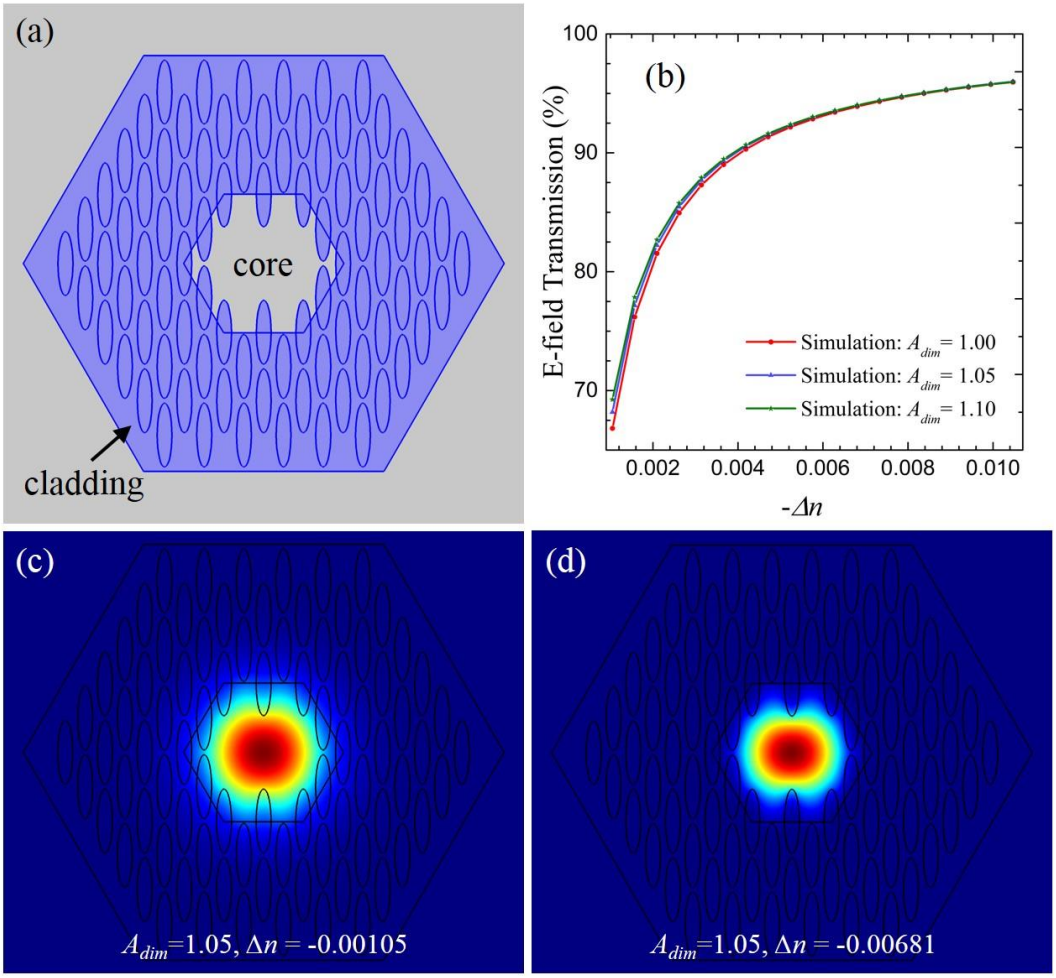

Figure 4.3 a) A simulation geometry shows the separated areas of waveguide's core and cladding for the electric-field integrations. b) Plot of the electric-field transition versus the refractive index contrast (Δn) of the elliptic tracks of various track's dimension factor (A_{dim}). The electric field profiles of the propagation mode of the simulation geometry with c) $\Delta n = -0.00105$ and d) $\Delta n = -0.00681$. The testing wavelength was at 1550 nm.

To quantitatively assess the optical guiding performance of the simulation waveguides, the parts of waveguide's core and cladding were specified as depicted in Figure 4.3a. The magnitude of an electric field located in each area was added up by the surface integration, and then was used for calculating the percentage of an electric field occupied in the core section (named 'an electric-field transmission'). In fact, Figure 4.3b shows that the electric-field transmission can be raised with the increasing values of Δn. The variations in sizes of the tracks via the coefficient A_{dim} was found to insignificantly affect the transmission ratio. Figure 4.3c and 4.3d show the electric-field profiles of the simulation waveguides with the refractive index contrast (Δn) of -0.00105 and -0.00681, respectively. It can be apparently noticed that the field for the case of lower Δn was more broadening into the cladding section than that of the higher Δn case.

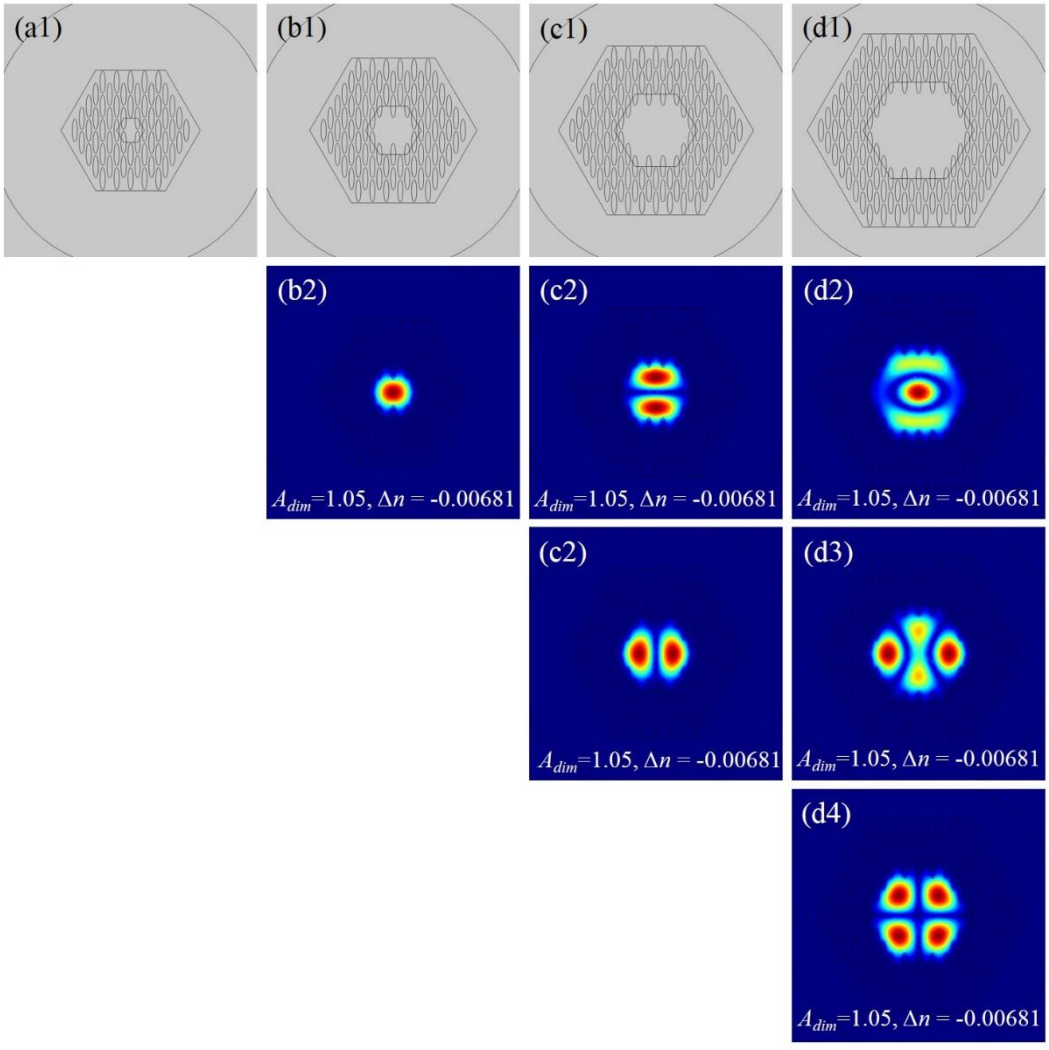

Figure 4.4 Computer simulation results show the effects of the waveguide's core size to the guiding mode in the simulation geometry. The parameters: $A_{dim} = 1.05$, $\Delta n = -0.00681$ and $a_s = 9.9$ µm, were fixed. The testing wavelength was at 1550 nm.

From our experiences in implementing the laser-inscription experiments, there were three parameters, i.e. the width of a waveguide core, the separation between adjacent tracks (a_s) and

the number of hexagonal cladding layer, of the waveguide's cross-sectional geometry which were found to significantly affect the optical guiding properties. To achieve the femtosecond inscription of an optical waveguide with low optical losses and fundamental-mode guiding, these three parameters were required to be properly optimized by using the computer simulations. The pictures in Figure 4.4 illustrate the effects of the width of a waveguide core on the optical exaction modes in this type of waveguide geometry. It should be noted that this core-size value, in the simulation, was altered by swapping the inner hexagonal layers to the outer-layer positions and vice versa. The number of cladding layers was fixed to 4 layers, and the computation parameters were set to $A_{dim} = 1.05$, $\Delta n = -0.00681$ and $a_s = 9.9$ µm. The simulation results of waveguide's excitation mode at a wavelength of 1550 nm, in Figure 4.4, show that it was only the geometry with a core width of ≈ 22 µm like in Figure 4.4.b1 which could excite the fundamental mode of an electric-field profile. It was found that the waveguide geometry with a smaller diameter of ≈ 9.9 µm in Figure 4.4.a1 could not support any guiding mode in the waveguide's core region, which could be plausibly due to the significantly low contrast between the core's and cladding's refractive indices. The uses of the larger core's sizes resulted in the higher-order mode excitations as can be seen in Figure 4.4.c and 4.4.d.

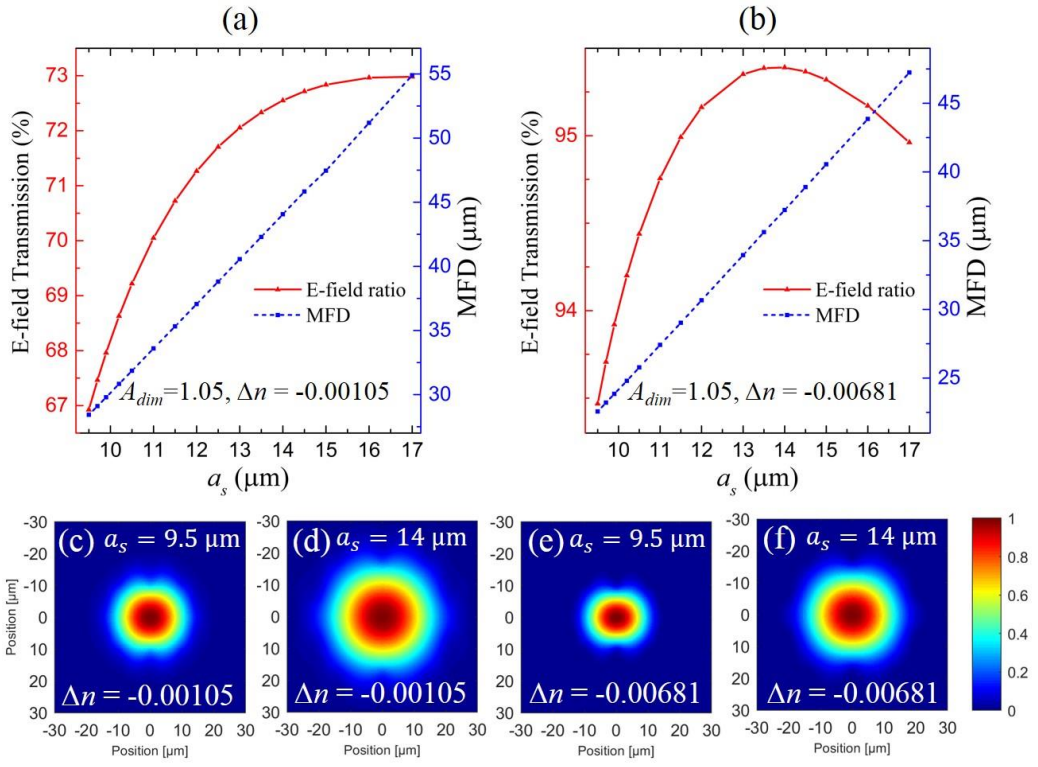

Figure 4.5 Computer simulation results show the effects of the track separation (a_s) to the electric field transmission, the mode-field diameter (MFD) and the guiding mode field. Plots of the electric field transmission and MFD versus the a_s for the simulation with a) $\Delta n = -0.00105$ and $\Delta n = -0.00681$. c-f) show examples of the electric field profile of different simulation conditions. The testing wavelength was at 1550 nm.

The double-axis graphs in Figures 4.5a and 4.5b demonstrate the impacts of the separation (a_s) between adjacent tracks on the electric-field transmission and the mode field diameter (MFD), which were were plotted in regard to the left and right axes, respectively. The graphs show that the MFD linearly increased with the increasing values of a_s. The transmission ratio tended to increase in the range of small a_s between 9 μm and 14 μm. For the range of a_s greater than 14 μm, the electric-field transmission seemed to be slowly varying and subsequently became decreased. The transmission ratio was found to reach the maximum when the a_s was around 16 μm and 13.5 μm for the track's refractive index contrast (Δn) of -0.00105 and -0.00681, respectively. In Figure 4.5c to 4.5f, the electric-field distributions showed that the fundamental mode was still be observed when the separation a_s was increased. These results suggested the trends of the transmission ratio and the MFD in regard to the parameter of track spacing a_s, which thus could be later used as a guideline for the fabrication experiments for this type of waveguide packing geometry.

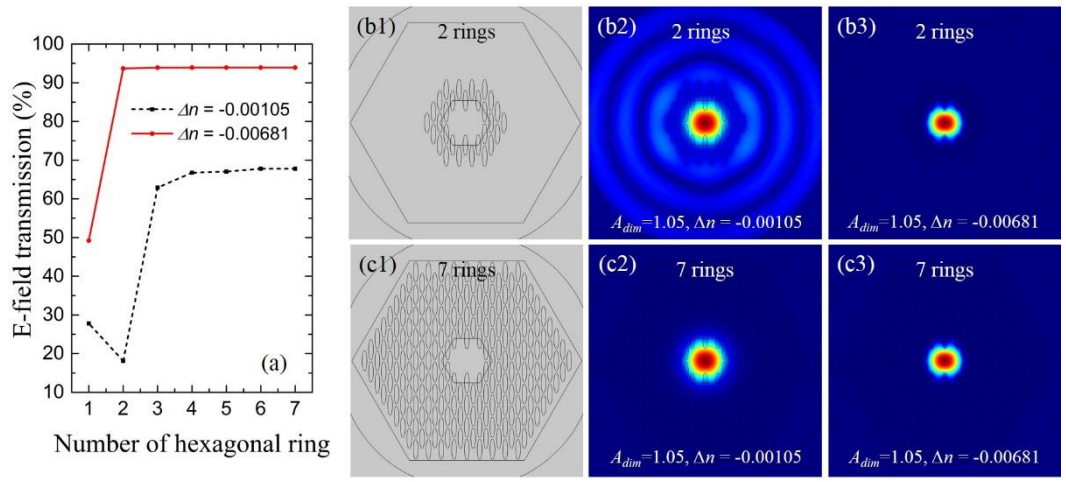

Figure 4.6 Computer simulation results show the effect of the number of hexagonal layers to the electric field transmission and the guiding mode fields. a) shows a plot of the electric field transmission versus the number of hexagonal layers for different Δn. Examples of the electric field profile of different simulation conditions for the simulation geometry with b) 2 rings and c) 7 rings. The testing wavelength was at 1550 nm.

The last parameter of waveguide's cross-sectional geometry which had been tested in our simulations was the number of track's hexagonal layer or ring. The computational results presented in Figure 4.6a suggested that the increases in the hexagonal ring dramatically enhanced the ratio of electric-field transmissions. In fact, these enhancements of waveguide's transmission were found sensitive to the track's refractive contrast (Δn). For the high Δn of -0.00681, the transmission reached its maximum value of ≈ 94 % when the layer number was just 2 layers or higher. In contrast, the simulations of waveguides with the low Δn of -0.00105 showed an abrupt increase of the e-field transmission to ≈ 63 % when the number of layers was 3 layers. Also, the

ratio tended to gradually raise to ≈ 68 % at the ring number of 7. The sets of images in Figures 4.6b and 4.6c present the electric-field profiles of the excited modes obtained from the simulations that used differing values of the layer number and the refractive index contrast Δn.

4.2 Fabrication strategies of the waveguides by Fs-laser inscription

In this section, the experimental results of our four sets of optical depressed-cladding waveguides (Set A, B, BX and C) fabricated by using the optical-lattice-like geometry will be presented. The parameter information of waveguide's cross-sectional arrangement that was investigated by the Comsol simulations, in the Section 4.1, had been applied to the study in this section for fabricating the waveguides with the optimized optical guiding characteristics. As illustrated in Figure 4.7, a laser-inscribed waveguide consisted of 84 Type-II tracks that were arranged in a hexagonal pattern where the adjacent tracks were equally separated by a spacing *d* of 9.9 μm which was chosen from our preliminary trails. Note that the *d* here was equivalent to the parameter as in the previous section. In fact, it had been the spacing values between 9 μm and 12 μm were found optimal in that the structures were neither too loosely located to excite multi-mode guiding nor too densely packed to induced strong structural stress.

The ratio of the inscription stage's vertical disposition (represented by circles in Figure 4.7) to the expected track's arrangement was found to be approximately 0.7. By using this ratio, it was found that the track mis-arrangement stemmed from the effects of optical refraction, self-focusing, and so on could be compensated. The total waveguide length was 2.35 cm. The indices, *n* and *m*, indicate the track's cross-sectional positions and will be later used in assigning the pulse energy of each track.

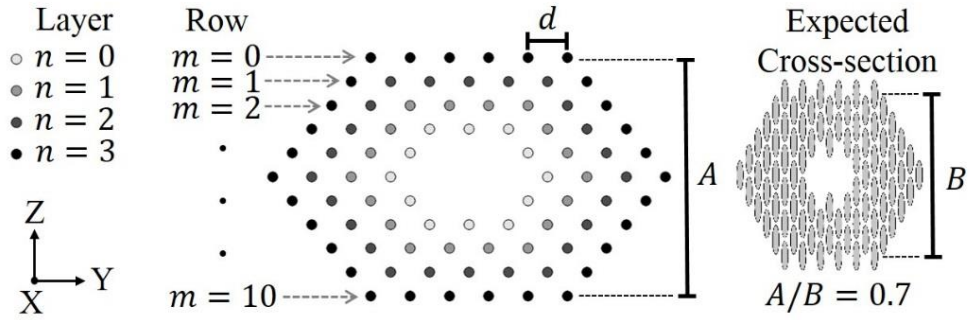

Figure 4.7 A cross-sectional layout of an inscribed waveguide. The circles represent the track disposition assigned in the translation-stage's controller software. The ellipses represent the expected appearance of a fabricated waveguide. The indices *n* and *m* label each track its order of radial layer and row, respectively.

The tracks were written by single-scanning of laser pulses along the x-axis of a z-cut lithium niobate crystal. The use of a focussing microscope objective with high numerical aperture

(NA=1.25) and also by maintaining the pule energy to not exceed the self-focusing threshold were found to be sufficient to minimize the filamentation of an inscribed structure. The range of writing depth was set close to the sample surface (between 35 μm and 130 μm) to reduce the effects of focus-splitting and spherical aberration effects mentioned in the Chapter 3. To avoid overlap between the already written structures and the laser focusing path, I started inscribing from the tracks of high *m* to low *m*.

Group	Waveguide Name and Initial Pulse Energy E_0 (nJ)											ΔE_d (nJ)	ΔE_r (nJ)	p	S (mm/s)
A	-	A01	A02	A03	A04	A05	A06	A07	A08	A09	A10	0.0	0.0	0.0	10
	-	39.1	40.9	42.7	45.5	48.2	50.9	53.6	56.4	59.1	61.8				
B	B00	B01	B02	B03	B04	B05	B06	B07	B08	B09	B10	0.3	0.0	0.0	10
	37.3	39.1	40.9	42.7	45.5	48.2	50.9	53.6	56.4	59.1	61.8				
BX	-	BX1	BX2	BX3	BX4	-	-	-	-	-	-	0.3	0.0	0.0	7
	-	39.1	43.6	50.9	56.4	-	-	-	-	-	-				
C	C01: 40.9 nJ											0.3	13.7	2.2	10
	C02: 42.7 nJ												8.2	1.0	
	C03: 40.9 nJ												13.7	1.0	

Table 4.1 Operational parameters for the fs-laser inscription of differing groups of laser-inscribed waveguide structures.

It was shown in the Chapter 3 that the laser energy density can be degraded by the spherical aberration when the depth of focus increases. This effect can cause the decline of refractive index modification of tracks located at higher *m*, hence, causing the inhomogeneity of the waveguide's cladding in vertical direction. However, I noticed that from the parameter testing experiment in Chapter 3 a proper control of pulse energy for different depths of focus was sufficient to compensate the energy density degradation and, thus, would improve the symmetry of our waveguide's depressed cladding region. To examine this assumption, we fabricated three groups (Group A, B and C) of waveguides using different schemes of pulse energy variation (see Table 4.1). **Group A** was assigned as a reference, where all tracks of each waveguide were written with equal pulse energy (E_0). In **Group B(X)**, the pulse energy was linearly increased when the track's depth increased. The waveguides in **Group C** were fabricated with both vertical and radial variation of pulse energy. The radial variation was included in this experiment in order to investigate whether it could be used to enhance the optical confinement in waveguides as it was suggested in the numerical study of Karakuzu *et al* [1]. To clarify the mentioned schemes, the values of pulse energy ($E_{m,n}$) allocated for a track of row *m* and layer *n* can be described by

$$E_{m,n} = E_0 + m\Delta E_d + \Delta E_r \left(\frac{n}{3}\right)^p \tag{4.1}$$

where the values of the initial pulse energy E_0, the energy-increasing steps ΔE_d and ΔE_r and parameter p are given in Table 4.1 for the Group A, B(X) and C. Note that ΔE_d and ΔE_r were chosen based on the empirical grounds of the experiment result shown in Chapter 3.

4.3 Optical confinement characteristics

The results of the optical guiding characterization of different waveguide groups before the thermal annealing process are summarized in Figure 4.8. It can be seen that both propagation loss (α) and mode field diameter (MFD) measured at 1550 nm wavelength were sensitive to the varying inscription parameters and the scheme of pulse-energy variation. In fact, the losses α and MFD tended to decrease with the increasing pulse energy (E_0) that induced higher refractive index contrast (Δn). However, when the E_0 was greater than approximately 50 nJ, the losses α of waveguides written by higher E_0 tended to grow presumably due to the increasing amount of laser-induced stress field and structural defects. A comparison between Group B and BX indicated that using lower stage's translation speed (S) can result in the inferior optical confinement. This behaviour may relate to the greater amount of track's roughness and stress, which generally occur when the tracks were inscribed with low speeds.

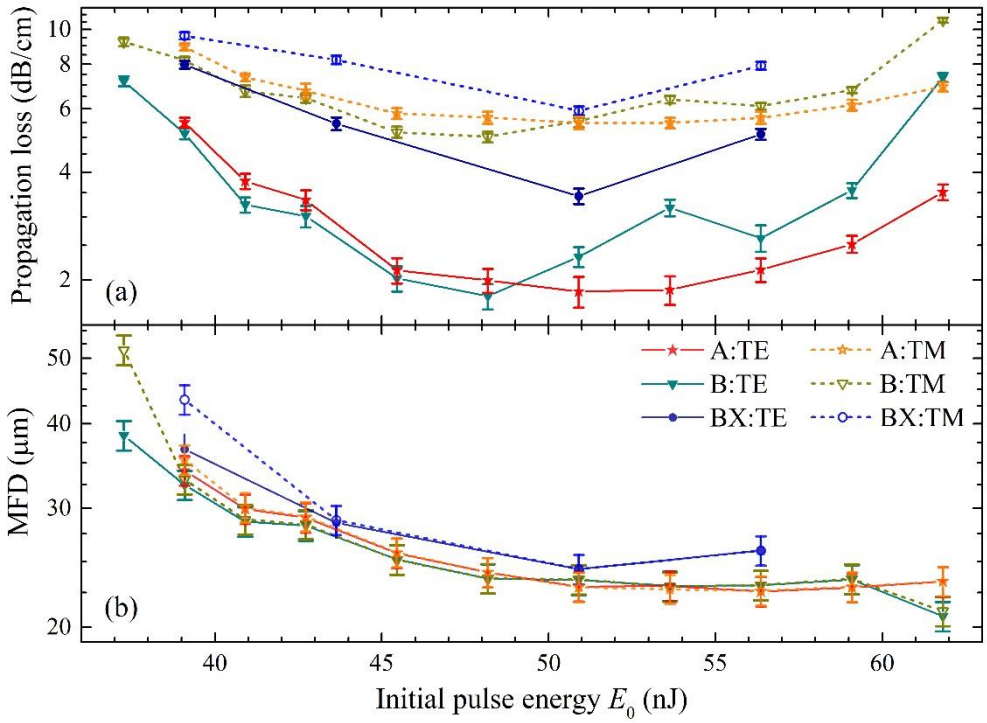

Figure 4.8 Optical guiding characteristics of unannealed waveguides. a) Optical propagation losses, and b) mode field diameters (MFD) of waveguides in Group A, B and BX versus the initial pulse energy E_0. The testing wavelength was 1550 nm. The length of a waveguide structure was approximately 2.35 cm. This figure is adapted from [3]

From the losses plotted in Figure 4.8, it can be observed that at this wavelength our waveguides can well confine the light of TE mode (polarisation direction perpendicular to the z-axis of lithium niobate crystal) but became lossy guiding in TM mode (polarisation direction parallel to the z-axis of lithium niobate crystal). One may try to understand this behaviour by considering on these two assumptions: 1) the anisotropic piezo-optic (APO) refractive index

change induced by the stress field around the laser-modified regions, and 2) the modal radiation leakage (MRL) effect caused by the mode coupling of orthogonal polarisations.

In the literature by Burghoff *et al* [4], the APO effect was mentioned to explain the optical confinement mechanism of the Type-II dual-track structure which was observed to support only the TM-polarisation propagation. The leaky guiding in TE mode was explained to stem from an anisotropic conformation change of crystal lattice on the lateral sides close to the laser-modified areas. Consequently, a negative refractive index change in TE polarisation (leaky mode) occurred due to a compressing stress in the horizontal direction, while a positive refractive index change in TM polarisation (guiding mode) presented due to a mechanical tension in the vertical direction. Nguyen *et al* [5] also applied the similar explanation to a depressed-cladding waveguide of single-ring geometry. They stated that because this APO effect occurred in the waveguide's cladding areas, it reduced the optical guiding in TM mode and improve the light confinement in TE mode. Still, this assumption is not yet clear if the APO effect could be used to explain the waveguide that was thermally treated to remove the residual stress field.

There are several literatures discussed about the MRL effect in a waveguide on a birefringent dielectric host, for example, in [6], [7]. The MRL is typically observed when the difference between the host's birefringent refractive indices is sufficiently high compared to the waveguide's core-cladding contrast, and also if the propagation direction is not exactly along the host's principle axis [6]. For the waveguide that suffers this MRL effect, the leaky mode will present in the polarisation of lower refractive index (which is the TM mode for lithium niobate). Since the MRL should be unaffected by the thermal annealing processes, it can likely be used to explain the anisotropic light confinement observed in this and the next section.

Before the thermal annealing process, I achieved the lowest propagation losses of $\alpha_{TE} = (1.8 \pm 0.1)$ dB/cm, $\alpha_{TM} = (5.0 \pm 0.2)$ dB/cm, and MFD $= (23.6 \pm 1.2)$ μm from B05 which was one of the waveguides implemented the suggested vertical pulse-energy variation scheme (Group B). If compared this result with the reference group (Group A), the waveguide A05 that shared the same E_0 had slightly higher losses $\alpha_{TE} = (2.0 \pm 0.2)$ dB/cm, $\alpha_{TM} = (5.6 \pm 0.2)$ dB/cm, and slightly larger MFD $= (24.1 \pm 1.2)$. In fact, it can be observed that the B05 consisted of tracks with more consistent cross-sectional size and refractive index modification than the A05 (see Figure 4.9, top row), which were assumed to cause the lower loss and more symmetric mode-field profile (see Figure 4.9, bottom row). Although the losses measured from the Group B waveguides did not show significant enchantment over the Group A, which indeed tended to become worse when E_0 was greater than 50 nJ (see Figure 4.8), more circular intensity distribution of Group B's mode field should provide a great benefit of less coupling losses when the inscribed waveguides were connected to a standard optical fibre.

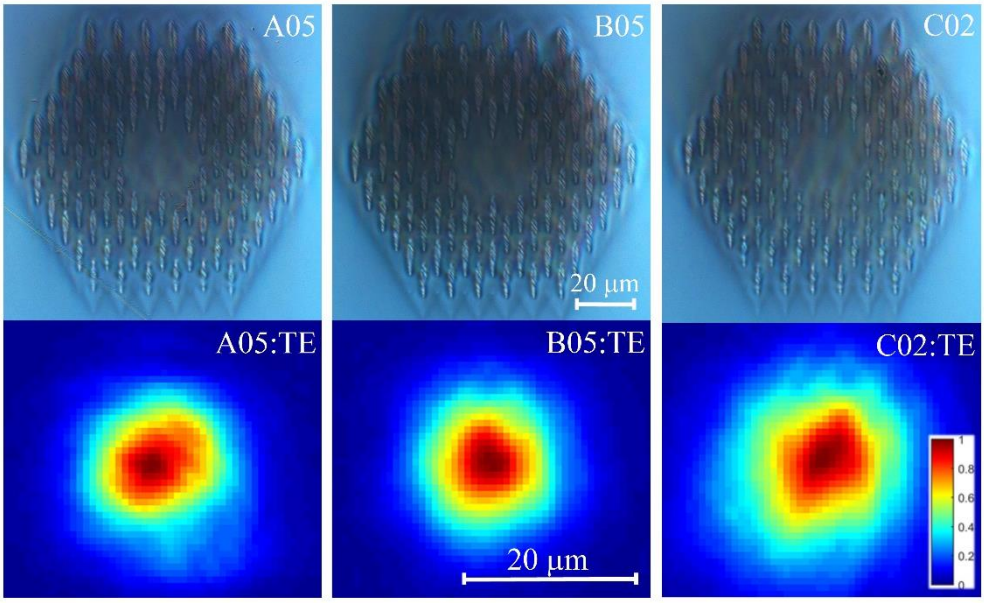

Figure 4.9 The DIC images of (unannealed) waveguide's cross-sections (top row), and the near-field intensity distributions of waveguide's outputs measured in TE mode. The testing wavelength was 1550 nm. The length of a waveguide structure was approximately 2.35 cm. This figure is adapted from [3].

If we compared the waveguide C02 with A05 and B05, the C02 showed more spreading mode-field intensity. However, the C02's losses were only slightly higher than those of A05 and B05 (see Figure 4.11). This might be because, although, the C02 consisted of the inner layer tracks of smaller size and weaker modification, their inner tracks may be smoother and had less laser-induced structural defects. The result suggests that this scheme of radial pulse-energy variation, used with Group C, might be useful in controlling the size and spatial distribution of waveguide's mode-field. Still, I believe that it is required further optimization to achieve the propagation loss as low as demonstrated in Karakuzu's simulation work [1]. It should be noticed that the fundamental guiding mode was observed the dominant mode excited in all waveguides fabricated in Group A, B(X) and C. A slight adjustment of the input coupling stage's positions did not result in the excitation of higher-order mode.

4.4 Effects of thermal annealing on the waveguide structures

Figure 4.10 shows the microscopic images of waveguide B07's cross-sections before and after each step of thermal annealing processes. The top-right image illustrates the waveguide looking from the top-view and focused on the plane of waveguide's centre. It can be observed that the areas which were assumed to be the stress and the non-damaged modifications were largely faded after the waveguides were treated at temperatures of 250 ^{o}C and 350 ^{o}C (for 3 hours each), and they seemed to completely disappear after the temperature of 700 ^{o}C. If compared to

the previous literature of Burghoff *et al* [8] that used the low-repetition-rate laser (1 kHz, $\lambda = 800$ nm), the non-damage modification areas were completely erased after the annealing at relatively lower temperature (200 ^{o}C) and shorter time (30 minute). In Figure 4.10, the crack-like structures occurred in the cladding area were assumed to be the result of non-uniform thermal expansions and/or contractions of the areas exposed and unexposed by the laser. The cracks seemed to exist only at a shallow depth from the waveguide facets and did not noticeably affect the optical guiding in the core area.

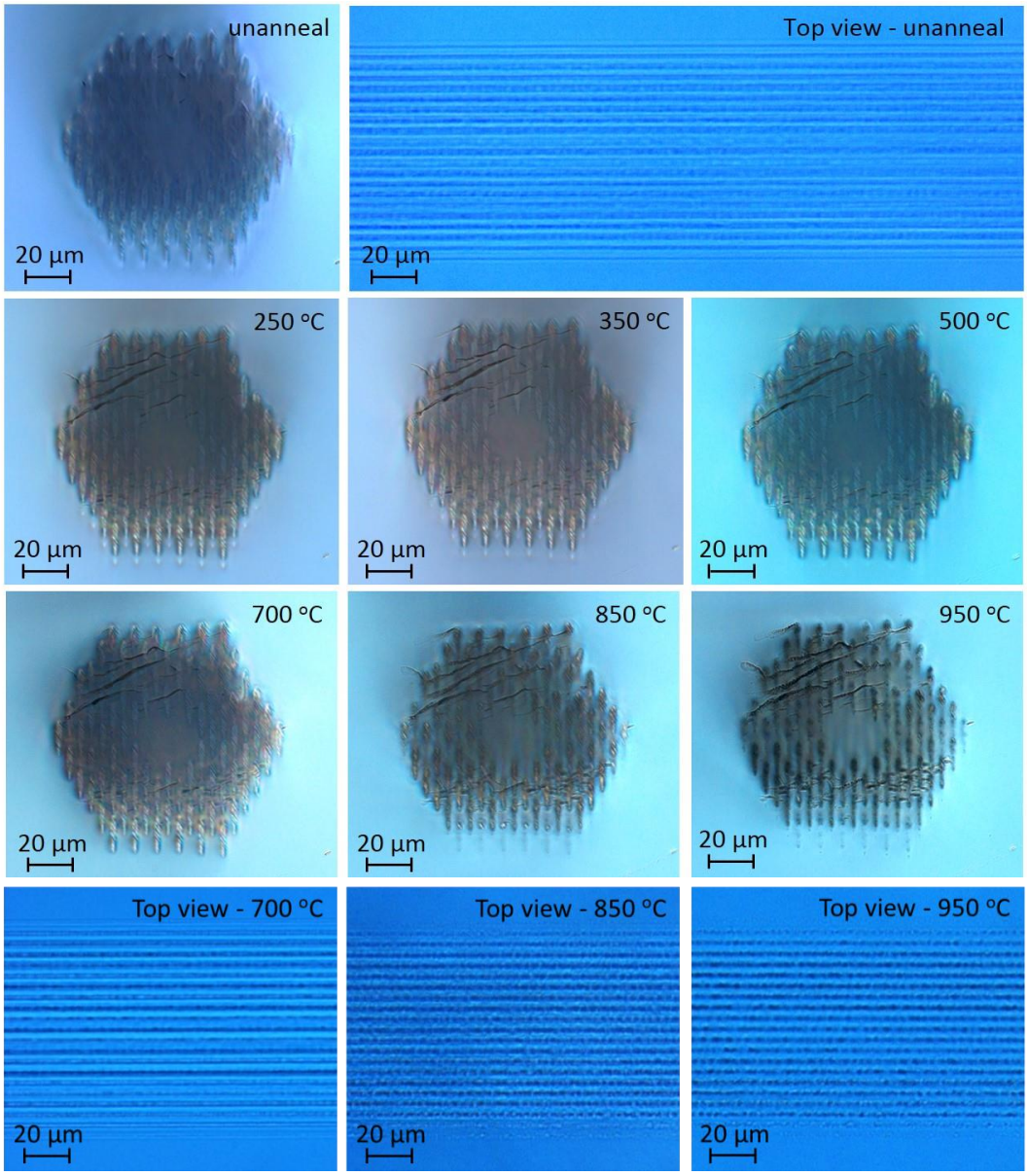

Figure 4.10 The DIC images of the B07-waveguide's cross-section and top-view captured before and after the thermal annealing processes. This figure is adapted from [3]

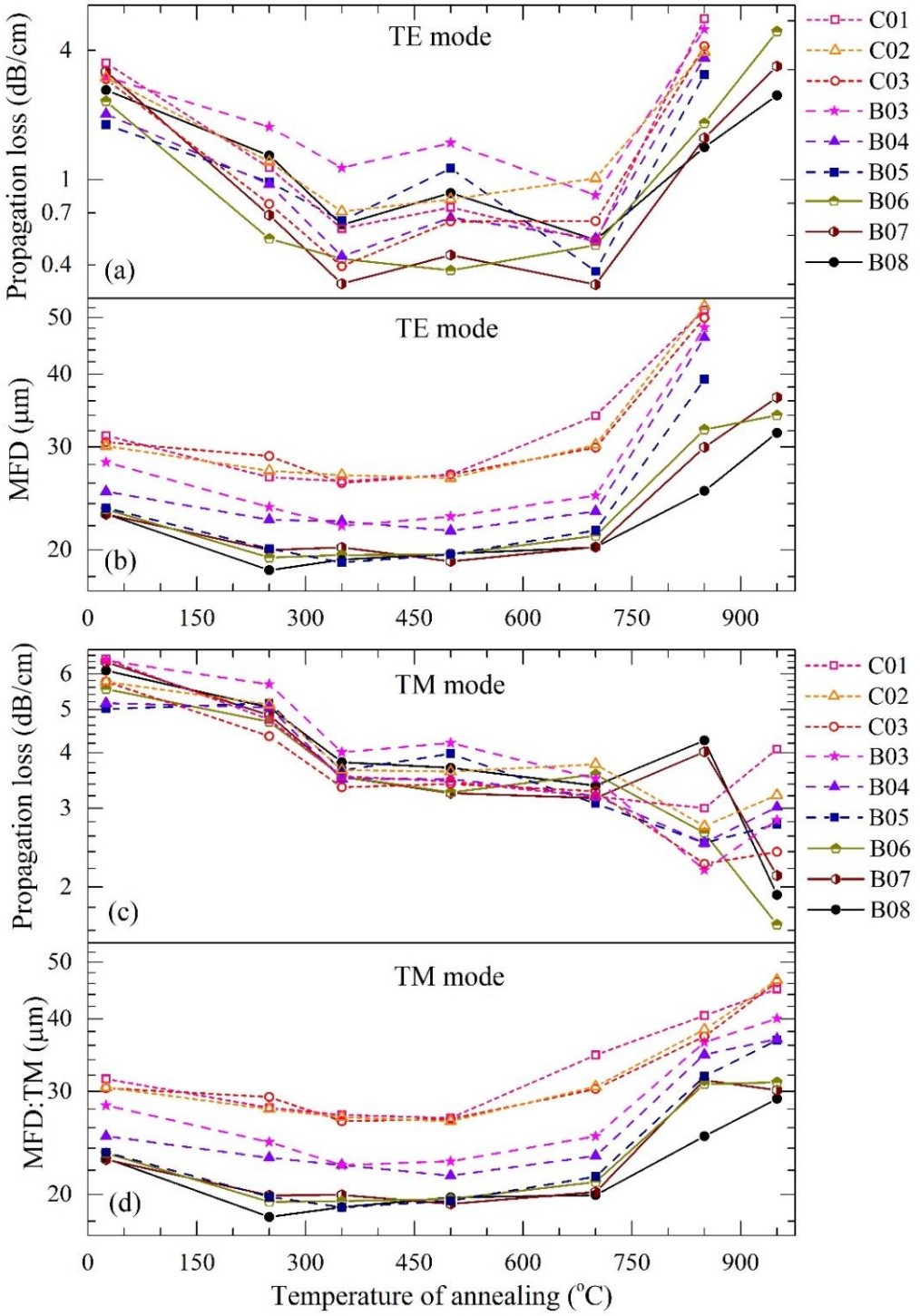

Figure 4.11 Optical guiding characteristics of annealed waveguides. The optical propagation losses in a) TE mode and c) TM mode versus the annealing temperatures. The mode field diameters (MFD) in b) TE mode and d) TM mode versus the annealing temperatures. The testing wavelength was 1550 nm. The length of a waveguide structure was approximately 2.35 cm. This figure is adapted from [3]

From the plots in Figure 4.11, the propagation losses measured in TE and TM polarisations at the wavelength of 1550 nm were found to be significantly reduced after the first two thermal annealing stages at temperatures of 250 °C and 350 °C. The minimum losses of $\alpha_{TE} = (0.4 \pm 0.1)$ dB/cm and $\alpha_{TM} = (3.5 \pm 0.2)$ dB/cm were recorded from the waveguide B07 after thermally treated at 350 °C. This low propagation loss in TE was derived from the total insertion loss of 3.7 dB, the estimated double Fresnel loess of 1.3 dB, and the loss from input beam's mode-mismatch of around 1.6 dB. The improvement in optical confinements may be explained as the result of the increase of overall refractive index contrast and the reduction of residual stress. The optical guiding in TE mode of some waveguides fabricated with low E_0 diminished after the temperature of 850 °C, and stopped guiding after 950 °C. It is worth noting that these temperatures are close to the lithium niobate's Curie point at 1140 °C. For the TM polarisation, interestingly, the light confinements were still observed even after the waveguides had been annealed at very high temperature of 950 °C.

In Figure 4.12, the wavelength dependence of optical confinement in the waveguide B06 was reported after it thermally treated at 350 °C. The TE propagation losses were found to be approximately constant over the testing spectral range, but the TM losses appeared to sharply increase at the near-infrared wavelengths (the fundamental mode was still observed). The MFD of near-field intensity of both TE and TM tended to raise with increasing wavelength and then slightly drop when the wavelength of testing lasers approached ≈ 1550 nm.

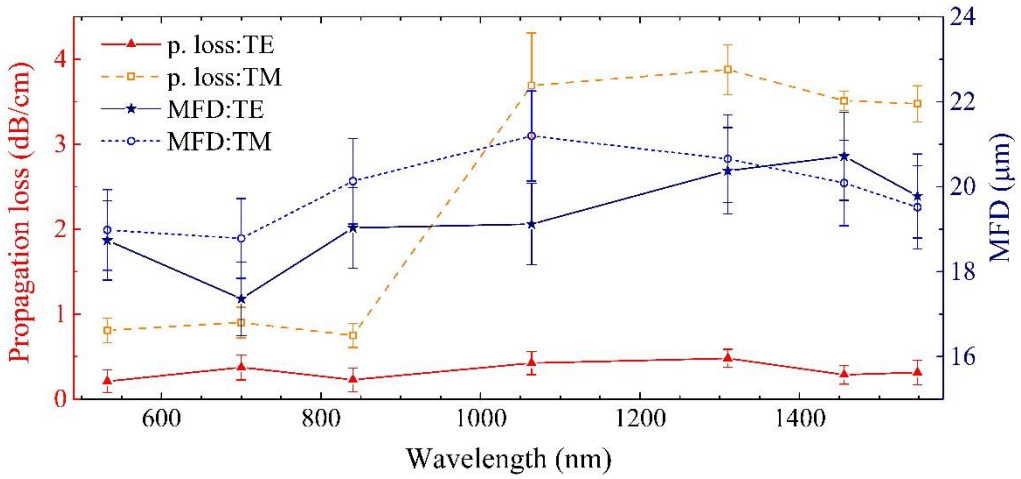

Figure 4.12 Optical guiding characteristics of the waveguide B06 after the step of thermal annealing at 350 °C. The plot shows propagation losses (left axis) and the MFD (right axis) versus the testing wavelength. The length of a waveguide structure was approximately 2.35 cm. This figure is adapted from [3]

Discussions and summary

In this chapter, our results of computational and experimental works on the parameter optimization and the femtosecond-laser inscription of an optical depressed-cladding waveguide have been reported. In the part of computational studies, a Comsol Multiphysics software had been used to numerically simulate the excited modes of a guiding electric field, which had been subsequently used for analyzing the mode field diameter (MFD) and the e-field transmission ratio of the differing waveguide geometries. The simulations focused on studying the impacts of the parameters that were relevant to the waveguide's cross-sectional arrangements on the spatial profile of an excited electric field. It should be noted that the simulation method was based on the finite-element approach and a Comsol's calculation interface in the frequency domain. In addition, the adaptive triangular mesh had been utilized to enhance the simulation accuracy. As had been discussed in the Chapter 2 about the technical details of our experiments, our substrate for laser inscriptions was a wafer of *z*-cut lithium niobate crystal and the inscribing laser was a high-repetition-rate pulse that was optically focused by a 100× microscope objective lens that had a numerical aperture (NA) of 1.25.

The results from the computer simulation showed that there were three parameters, including the core width, the separation between tracks (a_s) and the number of hexagonal cladding layer, which could significantly affect the spatial distribution and the mode of excitations on this type of waveguide geometry. Also, the increases in a refractive index contrast (Δn) of the cladding tracks tended to decrease the mode field diameter (MFD) and, hence, likely resulted in the more capability of light confinements in the waveguide's core region. By comparing the MFD and the guiding mode-field from the simulations with that retrieved from the experiments, the effective refractive index contrast of ≈ -0.0068 could be estimated for a laser-inscribed waveguide of B05. The optimizations of the waveguide's core width suggested that it was only the core width of approximately 22 μm, in which the positions of two inner hexagonal layers were unexposed to the inscribing pulses, that could lead to the simulation result of the fundamental-mode excitation. The computer simulation tests on the variation of track spacing (a_s) showed that the a_s was directly proportional to the MFD, but it had a nonlinear relationship with the e-field transmission that was found to reach its maximum when the a_s was approximately 16 μm and 13.5 μm for the simulations with track's refractive index contrast (Δn) of -0.00105 and -0.00681, respectively. For the last parameter of the testing simulations, it had been found that the increase of hexagonal layer number resulted in the smaller MFD and the less spreading distribution of the guided electric fields into the region of waveguide cladding, which thus implied a stronger optical confinement on the computer simulated structures. In the regime of high Δn of -0.00681, two layers of hexagonal ring were shown to suffice in maximizing the waveguide's transmission ratio of ≈ 94%.

In contrast, the ring number of at least 4 was required for the waveguides with the low Δn of -0.00105 to reach the transmission of ≈ 67%. Also, this transmission percentage was found to be gradually increased when the number of hexagonal layers was risen up to the number of 7 rings. This waveguide's optical confinement behaviour that was sensitive to the refractive index contrast and the cladding thickness could be plausibly explained by the effects of evanescent field coupling. The waveguide with a high refractive index contrast between the core and cladding regions can strongly confine a light beam having a mode field that is tightly distributed, and hence a thin cladding could suffice to prevent the optical loss caused by an evanescent field coupling. In contrast, the guided electric-field distribution in a waveguide that has a lower value of the index contrast tends to be more spatially spreading-out from a core region, resulting in a thicker cladding layer being required.

In the experiment part of this chapter, the femto-second laser inscriptions of a depressed-cladding waveguide with the hexagonal optical-lattice-like geometry had been demonstrated. The information of the optimum waveguide arrangement from the computer simulation results had been applied in this part. In addition, this section had revealed the impacts of inscription parameters including the pulse energy and the writing speed, and the thermal annealing treatments on the optical guiding characteristics of the laser-written waveguides. There were four sets, i.e. the set A, B, BX and C, of waveguides that had been fabricated by the different pulse-energy variation schemes and the writing speeds. Two schemes of vertical and radial pulse-energy variations for the tracks arranged in the cross-sectional plane were suggested to compensate the effects of optical distortions, and they had been practically utilized in our laser-inscription processes. From the results, it was found that the pulse energy and witting speed significantly influenced the optical losses and the mode field diameter (MFD), which hence highlighted the necessities of operational parameter optimizations. Before the thermal annealing, the minimum propagation losses of $\alpha_{TE} = (1.8 \pm 0.1)$ dB/cm and $\alpha_{TM} = (5.0 \pm 0.2)$ dB/cm at a wavelength of 1550 nm could be achieved from a waveguide B05 which was fabricated by using the initial pulse energy and the writing speed of 48.2 nJ and 10 mm/s, respectively. The uses of vertical pulse-energy variation, in which the energy gradually increased with the increasing depth of focus, had been observed to benefit in improving the waveguide's cross-sectional cladding symmetry, which apparently resulted in the more circular guiding mode and slightly lower propagation losses when compared to the fabrication scheme of uniform pulse-energy. Also, for another pulse-energy scheme of radial variation, its potential use had been found for the manipulation of a guiding mode profile in which its MFD could be flexibly adjusted.

It must be mentioned that our waveguides fabricated in this study had shown a well-guiding property for an input beam of TE-polarised state but were found to have lossy guiding modes in the TM-polarised state at a wavelength of 1550 nm. This behavior could be presumed to be

stemmed from the modal radiation leakage (MRL) effect, which was originated from the mode coupling between the orthogonal polarisations. The study on the thermal annealing effects revealed that, after the sample was treated at the temperatures of 250 °C and 350 °C for 3 hours each, the waveguide's optical losses of both orthogonal polarisations could be highly reduced. The minimum propagation losses of $\alpha_{TE} = (0.4 \pm 0.1)$ dB/cm and $\alpha_{TM} = (3.5 \pm 0.2)$ dB/cm could be measured from the waveguide B07 at a wavelength of 1550 nm. In fact, this low attenuation could also be observed for a broad spectrum ranging from 530 nm to 1550 nm. The thermal stability of our waveguides had been found to be relatively high compared to that of other previous literatures. This characteristic of heat tolerance, up to an annealing temperature of 700 °C, was presumably stemmed from the strong laser-material interactions in the heat-accumulation regime occurred when the pulse repetition of an inscribing laser was sufficiently high. Because of these two outstanding features of the low propagation losses in a wide range of spectrum and the high thermal tolerance, the waveguide structures demonstrated in this chapter were potentially suitable for many applications such as telecommunication data-transfer devices, photonic circuits for nonlinear optics and optical sensors for the harsh environments.

References

[1] H. Karakuzu, M. Dubov, and S. Boscolo, "Control of the properties of micro-structured waveguides in lithium niobate crystal," *Opt. Express, OE*, vol. 21, no. 14, pp. 17122–17130, Jul. 2013, doi: 10.1364/OE.21.017122.

[2] H. Karakuzu, M. Dubov, S. Boscolo, L. A. Melnikov, and Y. A. Mazhirina, "Optimisation of microstructured waveguides in z-cut $LiNbO_3$ crystals," *Opt. Mater. Express, OME*, vol. 4, no. 3, pp. 541–552, Mar. 2014, doi: 10.1364/OME.4.000541.

[3] T. Piromjitpong, M. Dubov, and S. Boscolo, "High-repetition-rate femtosecond-laser inscription of low-loss thermally stable waveguides in lithium niobate," *Appl. Phys. A*, vol. 125, no. 5, p. 302, Apr. 2019, doi: 10.1007/s00339-019-2609-6.

[4] J. Burghoff, S. Nolte, and A. Tünnermann, "Origins of waveguiding in femtosecond laser-structured $LiNbO_3$," *Appl. Phys. A*, vol. 89, no. 1, pp. 127–132, Oct. 2007, doi: 10.1007/s00339-007-4152-0.

[5] H.-D. Nguyen *et al.*, "Heuristic modelling of laser written mid-infrared $LiNbO_3$ stressed-cladding waveguides," *Opt. Express, OE*, vol. 24, no. 7, pp. 7777–7791, Apr. 2016, doi: 10.1364/OE.24.007777.

[6] M. Lu and M. M. Fejer, "Anisotropic dielectric waveguides," *J. Opt. Soc. Am. A, JOSAA*, vol. 10, no. 2, pp. 246–261, Feb. 1993, doi: 10.1364/JOSAA.10.000246.

[7] W. Burns, S. Sheem, and A. Milton, “Approximate calculation of leaky-mode loss coefficients for Ti-diffused $LiNbO_3$ waveguides,” *IEEE Journal of Quantum Electronics*, vol. 15, no. 11, pp. 1282–1289, Nov. 1979, doi: 10.1109/JQE.1979.1069927.

[8] J. Burghoff, H. Hartung, S. Nolte, and A. Tünnermann, “Structural properties of femtosecond laser-induced modifications in $LiNbO_3$,” *Appl. Phys. A*, vol. 86, no. 2, pp. 165–170, Feb. 2007, doi: 10.1007/s00339-006-3750-6.

Chapter 5

Fs-laser Inscriptions of Other Optical Structures

This chapter's aims were to investigate the suitable geometry and configuration for the fabrications of curvilinear structures and optical power splitters. Also, it was aimed to demonstrate the structure integration of multiple optical components for enhancing the optical functionalities and the structure compactness of a laser-inscribed device. The cross-sectional arrangement of our optical guiding structure was still utilized the depressed-cladding optical-lattice-like packing. In addition, the fabrication scheme of vertical pulse-energy variation had been used in the laser inscription process to ensure the cross-sectionally symmetric confinement of the device's cladding regions.

This chapter consists of four sections which include the studies on the impact of cladding thickness and bending radius of a curvilinear structure, the structure optimization of a beam splitter based on the multi-mode interference effect, and the fabrication of a beam splitter structure with an extended separation distance between the output branches. In the ***Section 5.1*** and ***5.2***, two sets of waveguides were fabricated in the differing forms of straight and curvilinear arrangements. Their optical guiding characteristics were compared between the structure sets fabricated with 4 and 7 hexagonal lattice layers. Also, the relationship between the radius of curvature of the fabricated curvilinear waveguides and the optical loss were revealed in the Section 5.2. The ***Section 5.3*** will present the results of the laser-inscription of beam splitters, which consisted of the multi-mode guiding section that had been numerically optimized by the computer simulations in a Comsol Multiphysics software to enhance their optical transmissions. In the ***Section 5.4***, the fabrication of a beam splitter, in which its splitting-arm separation distance was extended by a structure incorporation with the curvilinear guiding channels, will be demonstrated.

5.1 Effects of waveguide cladding thickness

In this section, the effects of cladding thickness on the optical guiding properties of a straight optical-lattice-like waveguide will be revealed by using the experiment results obtained from two sets of laser-inscribed waveguide structures that consisted of differing number of hexagonal lattice layer, as shown in Figure 5.1a and 5.1b. After the fabrications, the waveguides consisting of 4 layers (in Figure 5.1a) and 7 layers (in Figure 5.1b) were measured in their cladding sizes resulting in the obtained thickness values of approximately 40 and 70 μm, respectively. Hence, the difference in cladding thickness of the waveguides between these two sets was roughly 30 μm. It should be noted that the waveguides with 4 hexagonal layers presented in this section were written with a similar cross-sectional arrangement as those in the Chapter 4, but with slight differences in the parameters for pulse-energy variation that will be later described. For a simple identification between these two fabricated sets, our structures consisting of 4 and 7 layers will be hereafter called the 'wg_4R' and 'wg_7R', respectively

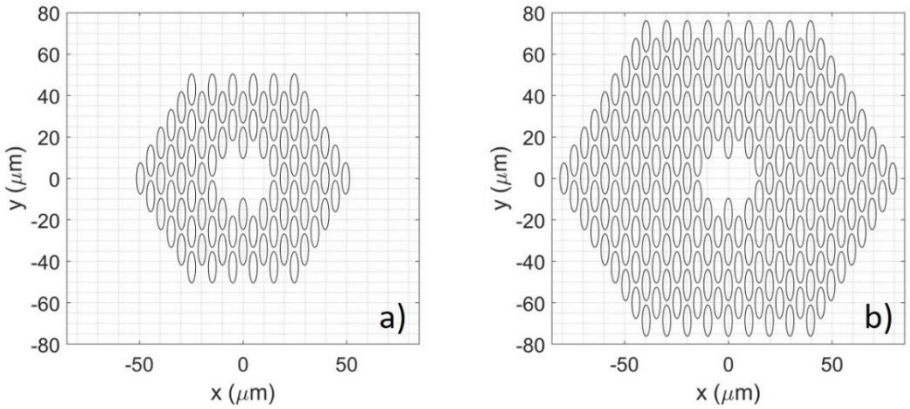

Figure 5.1 Cross-sectional track's arrangments of the waveguides wg_4R and wg_7R, respectively.

Both sets of waveguides were laser-inscribed by using the same scheme of vertical pulse-energy variation, which had been previously mentioned in the Section 4.2. However, there were some minor modifications in the coefficient values used in the Equation 4.1. The coefficients of pulse-energy steps ΔE_d and ΔE_r were set to 1.45 and 0.0 nJ, respectively, for both wg_4R and wg_7R. For the initial pulse energy (E_0), the wg_4R was assigned with a value of 40.7 nJ, whereas the energy E_0 of 36.4 nJ was used in the wg_7R. It was worth mentioning that these sets of coefficients ΔE_d and E_0 had been accordingly adjusted based on the observations in the previous experiments in the Chapter 4, to achieve the waveguide structures with more symmetric cross-sections and less creations of the lattice defects induced by the high-energy pulses. After the inscription of waveguide structure had been completed, the substrate of *z*-cut lithium niobate crystal was cut and surface-polished into a sample with the total length of ≈ 2.5 cm. Then, the sample was applied to a single step of thermal annealing treatment at the temperature of 250 ºC

for 3 hours. In the stage of optical guiding characterizations, the structures were trouloughly tested for the propagation losses and the mode field diameter (MFD) at a wavelength of 1550 nm by the methods that had been already mentioned in the Section 2.5.

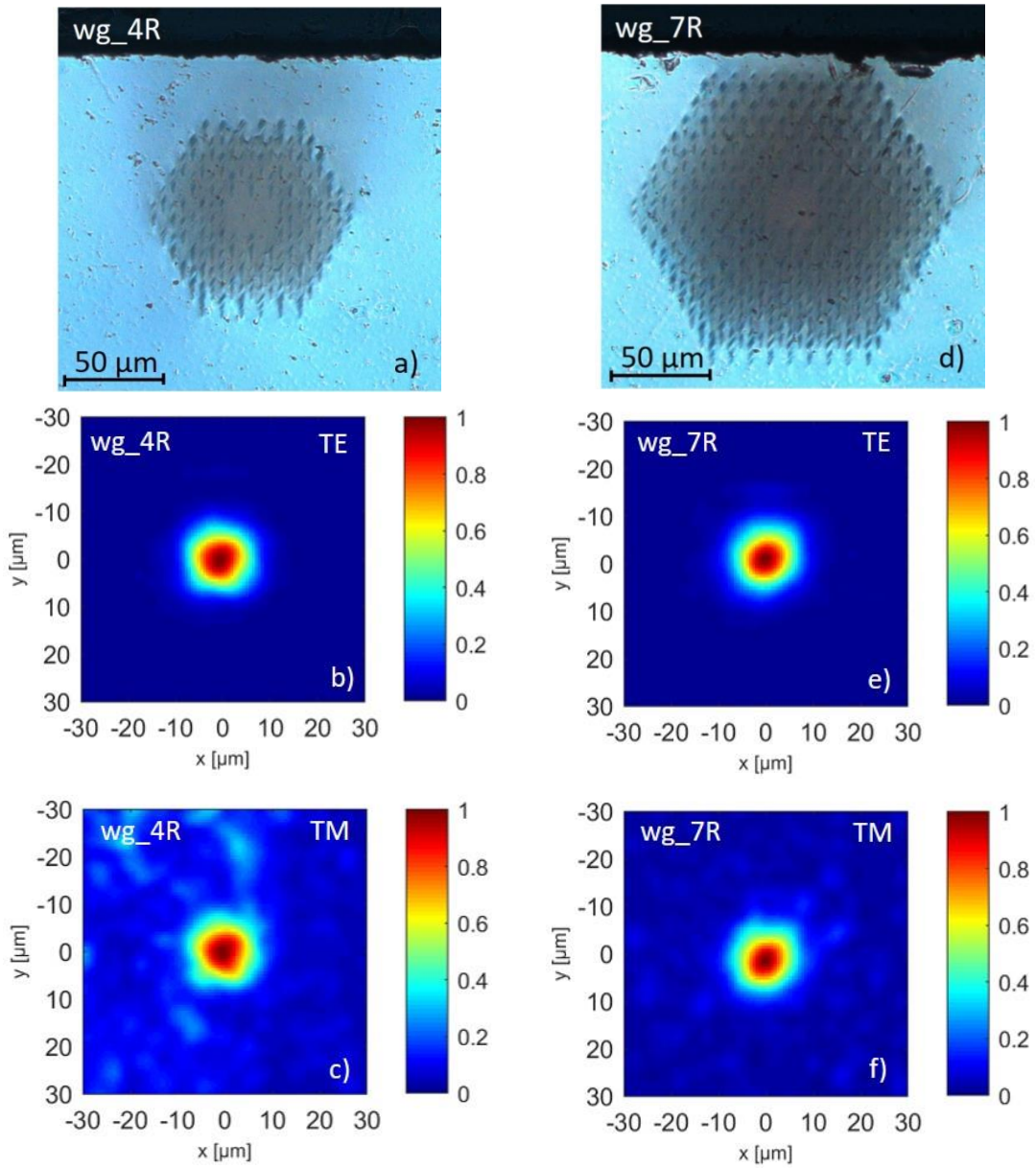

Figure 5.2 Cross-sectional DIC images of the waveguide a) wg_4R and d) wg_7R after thermal annealing. The near-field intensity ditributions measured from the waveguides b-c) wg_4R and e-f) wg_7R in TE and TM modes. The testing wavelength was at 1550 nm.

Microscopic images of the waveguide's cross-sections recorded from the sample's input facet were presented in the Figure 5.2a and 5.2d for the wg_4R and wg_7R, respectively. The laser-inscribed tracks had clearly appeared in the correct positions, and were also observed to have the nearly balanced strength in the laser-induced modifications along the vertical and horizontal directions of the cross-sectional plane. Hence, the optical measurements of near-field guiding mode from these optical guiding structures had resulted in the nearly circular and

symetruc intensity profiles as shown in Figure 5.2b-c and 5.2e-f. It should be noted that the testing wavelength was at 1550 nm, and the beam was altered between the TE and TM polarisation states by means of a polarizer and a haft-wave plate. These TE and TM modes were defined by the beam states with the polarisation directions that were parallel and perpendicular, respectively, to the crystalline z-axis of a lithium niobate crystal. In the TE-polarised mode, there was no significant difference between the guided mode-fields between the wg_4R and wg_7R could be noticed. In contrast, the mode field of the wg_7R had been found to be more spatially confined in the core region and less distributed in the cladding area than the that of the wg_4R in the polarisation mode of TM.

name	MFD (μm)		Total insertion loss (dB)		Propagation loss (dB/cm)	
	TE	TM	TE	TM	TE	TM
wg_4R	20.1	20.0	4.09 ± 0.21	22.75 ± 0.84	0.65 ± 0.08	7.90 ± 0.34
wg_7R	19.9	19.8	3.95 ± 0.08	22.57 ± 0.25	0.45 ± 0.03	7.83 ± 0.10

Table 5.1 Optical guiding properties of the waveguides wg_4R and wg_7R. The testing wavelength was at 1550 nm.

The optical characteristics including the mode field diameter (MFD), the total insertion loss and the propagation loss of the waveguide structures wg_4R and wg_7R were listed in the Table 5.1. It can be seen that the MFD in the TE and TM polarisations of the wg_7R were slightly smaller than that of the wg_4R, which corresponded to the observations of mode fields in Figure 5.2. Also, the propagation losses of the wg_7R were found to be less than those of the wg_4R in both states of polarisations. However, these differences between their optical characteristics were noticed to be only the marginal values, which indeed shown a good agreement with the computer-simulation outcomes (that used the $\Delta n = -0.00681$) presented in Figure 4.6 in the Section 4.1. Thus, this result may be used to imply the estimated value of an effective refractive index contrast of the tracks inscribed by these inscription conditions.

5.2 Curvilinear waveguide structures

The optical attenuations of a waveguide due to the structure curvature is also one of the important factors that should be quantitatively investigated and optimized for the fabrication of an optical structure that, especially, consists of complex arrangements and multiple components which can be typically found in the integrated photonics (IP) devices. To study this effect of structure curvature in our optical waveguides, two sets of waveguides that each comprised of two bending parts that had the equal angles of 3 degree and same curvature radii (R) had been fabricated. Each set consisted of 7 bending waveguide structures that were fabricated with varying radius (R) which were R = 20, 40, 60, 80, 100, 120 and 140 mm. Aslo, these two sets were laser-inscribed with similar values of all inscription paramters, except the cladding thicknesses which

were differeently implemented with the 4 and 7 hexagonal rings.The top-view arrangements of these curvilinear structures were illustrated in Figure 5.3a and 5.3b for an individual and a set of structures, respectively. As depicted in Figure 5.3a, the first section of straight waveguise had a fixed length l_1 of 5 mm. For the second and third straight sections, the lengths l_2 and l_3 were accordingly adjusted such that the total horizontal length L and the total structure's length of 25 mm and 25.006 mm, respectively, could be obtained.

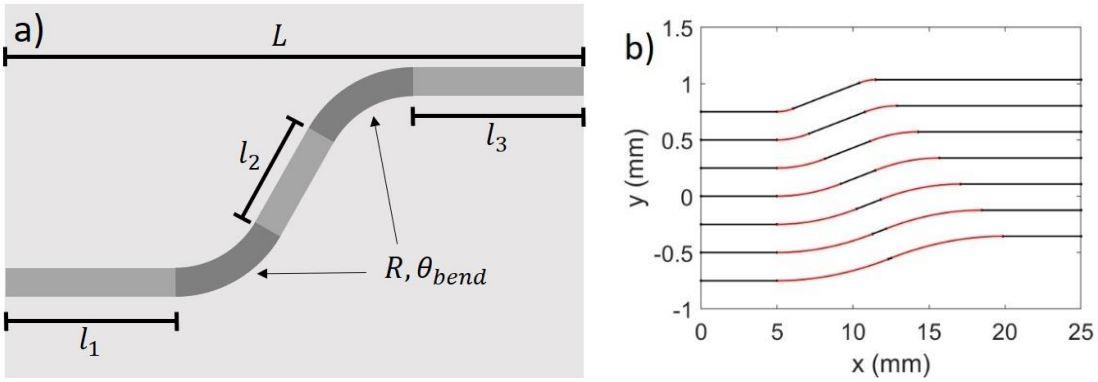

Figure 5.3 Diagrams of a) a waveguide with two bend sections of radius R and angle θ_{bend} and b) an array of 7 bend wavegiudes with different radii of curvature (R = 20, 40, 60, 80, 100, 120 and 140 mm). The angle was fixed at $\theta_{bend} = 3^o$.

Figure 5.4a and 5.4b plotted the total optical insertion losses of the two curvilinear structure sets as the functions of the radii of curvature measured with the guided beams at a wavelength of 1550 nm in the polarisation modes of TE and TM states, respectively. It can be noticed that the insertion losses in both modes of polarisation states highly reduced when the radii of bend sections increased. Interestingly, the sets of curvilinear waveguides wg_4R which were fabricated with a smaller number of hexagonal layers had shown lower losses in TE polarisation than those of the wg_7R when the radius of curvature was less than 60 mm. Outside this range of radius, there was no significant difference of the measured insertion losses between the wg_4R and wg_7R sets being observed.

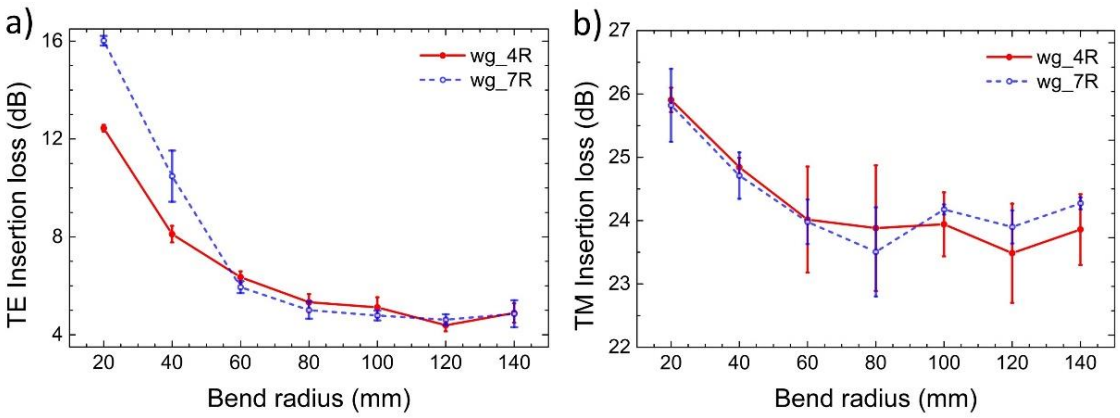

Figure 5.4 Total insertion losses of the bend waveguide structures measured in a) TE mode and b) TM mode versus the bend radius. The testing wavelength was at 1550 nm.

5.3 Optical power splitter based on multi-mode interference

An optical power splitter or a beam splitter, which has been typically used for dividing a light beam into multiple optical channels, is one of the basic optical components that have been importantly required for many kinds of integrated photonics (IP) devices. There are several splitter's configurations, such as the Y-junction splitters and the beam-coupler splitters, of the waveguide-based beam splitters that have been widely used and demonstrated in the literatures. Compared with these conventional splitters, a beam splitter that is based on the optical splitting mechanism of multi-mode interferences (MMI) has been considered relatively newer in the research field and it has been demonstrated to provide some promising advantages such as a compact footprint and a wavelength-sensitive beam split effect.

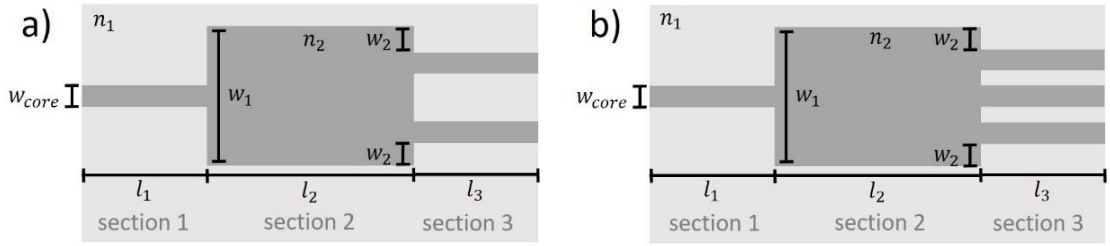

Figure 5.5 Simulation's geometries of the multi-mode interferencing splitters with a) two spltting outputs and b) three splitting outputs.

In this section, the femtosecond-laser inscription of a waveguide-based beam splitter which was based the multi-mode interference had been demonstrated. There were two structural geometries, that had two and three output branches as shown in Figure 5.5, of the power splitters being implemented in this study. To optimize the waveguide's section where the multi-mode inference occurred, a commercial software COMSOL with the EWBE (beam-envelop) interface and the two-dimensional finite element method was used for constructing the splitter's geometries like in Figure 5.5a-b and numerically simulating the excited modes of beam propagation. The parameters of this simulation work such as a straight waveguide's core size (w_{core}), cladding's refractive index (n_1), core's refractive index (n_2) were set according to the experimental results that were previously reported in the Chapter 4. From the figures, the relevant values included $w_{core} = 22$ µm, $n_1 = 2.2129$ and $n_2 = 2.2111$. Note that the value of n_2 was calculated from the corrected Sellmeier coefficients [1] for a congruently-grown lithium niobate's ordinary refractive index at a wavelength of 1550 nm. The other parameters, such as w_1, w_2 and l_2, that highly influenced the interference patterns of multi-mode excitations were iteratively adjusted so that the splitter's output intensities retrieved from the computer simulation were maximized.

Due to the waveguide geometry that was based on the hexagonal optical-lattice-like packing, there were two possible configurations of beam splitters which could provide the high optical transmissions when they were tested by the Comsol simulations. These splitter

configurations were different in that the parameter which determined the splitter's lateral extension width (w_2) could be either $w_2 = 0$ µm or $w_2 = 9.9$ µm. Also, the splitters with two and three output branches had been included in our study resulting in 4 sets of beam splitters being examined. The splitters with two and three branches were named 'sp1 - sp2' and 'sp3 - sp4', respectively. Other parameters, i.e. w_1, w_2 and l_2, indicating the structure geometry were listed in Table 5.2. It should be mentioned that these values of parameters had be already optimized for the maximum intensity transmission by means of the mentioned computer simulations, whose results of two-dimensional electric field profile of an excited mode at a simulation wavelength of 1550 nm were revealed in Figure 5.6 for different splitter sets. It should be noted that the values of setting refractive indices were assigned for the TE-polarised mode guiding. In addition, the total insertion losses and the splitting ratio of an optical intensity measured from the waveguide splitter outputs at a wavelength of 1550 nm have been presented in the same table of Table 5.2. It was observed that, for the two-branch splitter, the insertion loss of the structure sp2 with lateral extensions could performed the lower losses in both polarisation states than those of the sp1. In contrast, the structure with no side extension of the sp3 showed the lower losses than the sp4 for the case of three-branch splitter. A splitting ratio between the sp1 and sp2 showed no significant difference, which had nearly balanced outputs of the two splitter's branches. For the sp3 and sp4 structures, the difference of their splitting ratios can be clearly noticed. The three-branch splitter (sp3) with lateral extensions could output more balanced ratio of the measured splitting intensity.

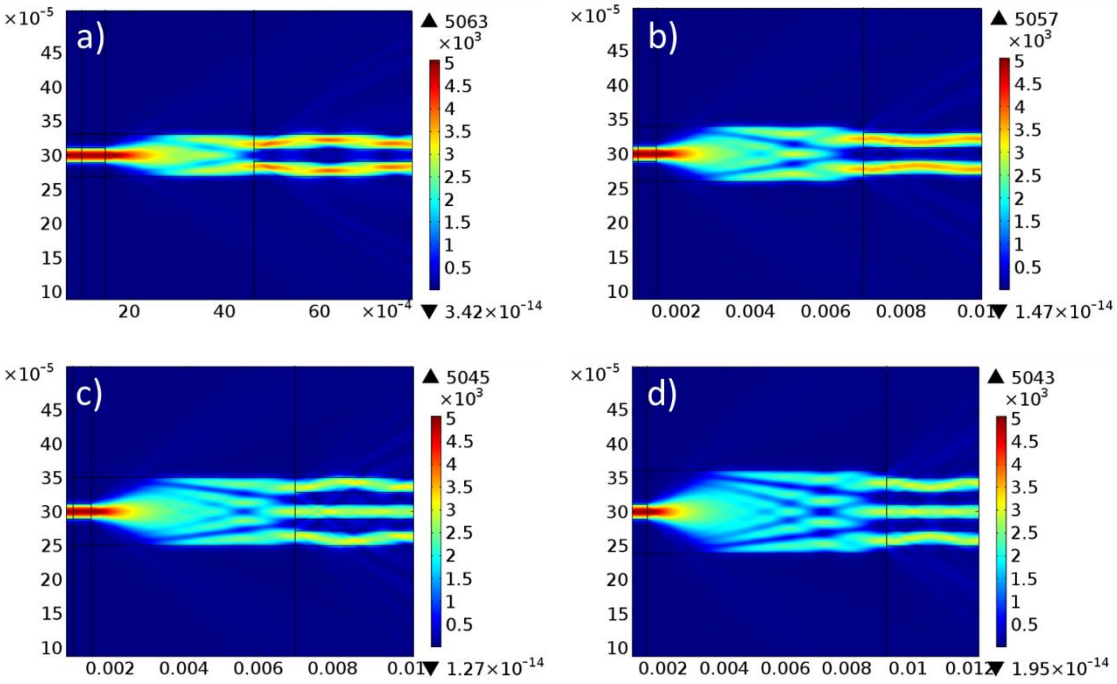

Figure 5.6 Computer simulation results from COMSOL. The intensity distribution of guided modes in the splitter structures of a) sp1, b) sp2, c) sp3 and d) sp4. The simulation wavelength was at 1550 nm. The values of setting refractive indices were assigned for the TE-polarised mode guiding.

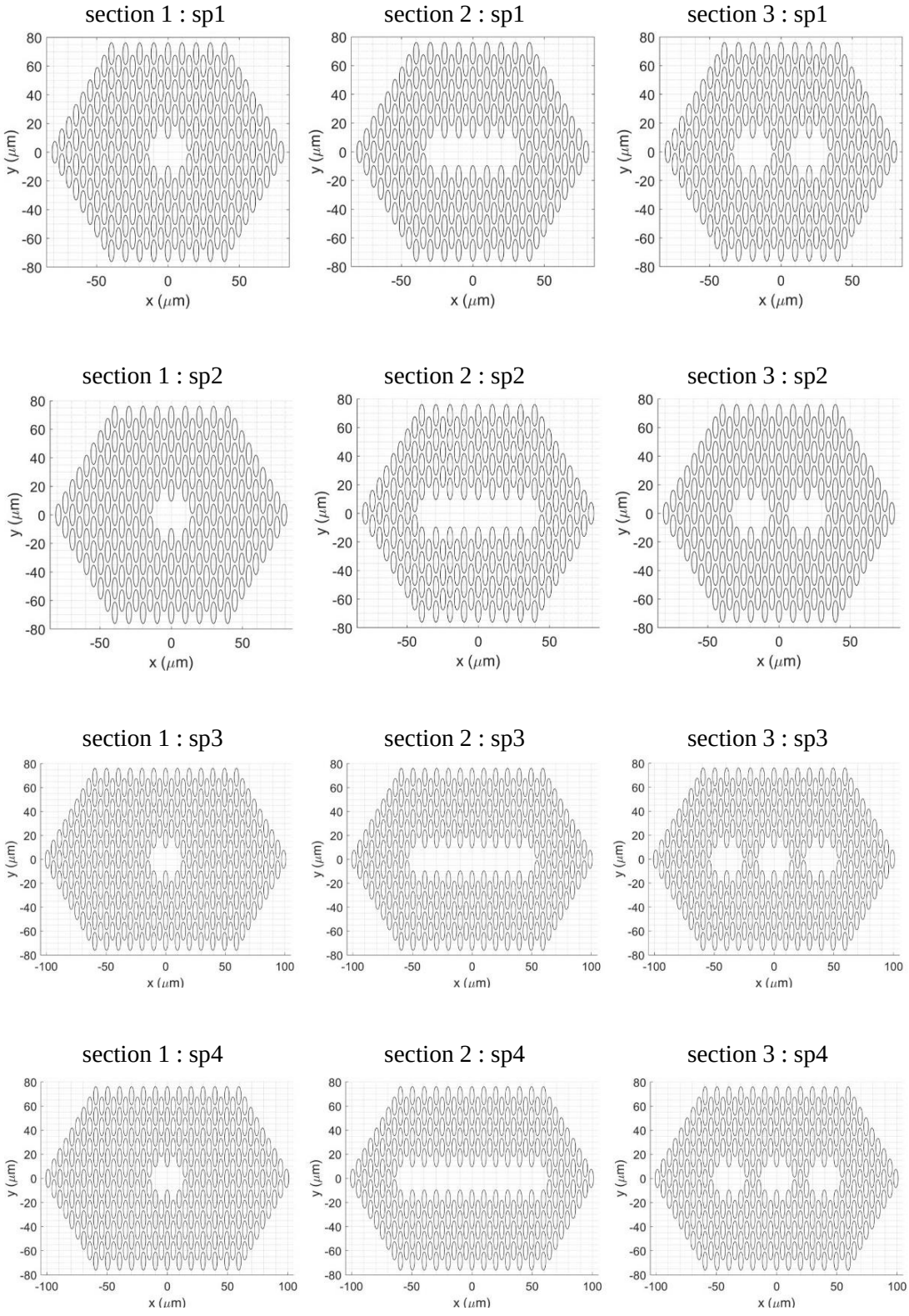

Figure 5.7 Cross-sectional track arrangement of two-output splitter (sp1), two-output splitter with side extensions (sp2), three-output splitter (sp3) and three-output splitter with side extensions (sp4) in the structure's section 1-3, indicated in the diagrams a) and b) in Figure 5.5.

As depicted in the top-view geometry diagram of our beam splitters in Figure 5.5, there were three sections along the splitter's longitudinal length which were the different components and had been required to be fabricated by dissimilar track's cross-sectional arrangements. In Figure 5.7, the schematic diagrams illustrate the dispositions of laser-inscribed tracks on the cross-sectional plane of differing splitter's parts that corresponded to their top-view representations in Figure 5.5. These track's arrangements had been implemented in our fabrication process, where the G-codes for controlling inscription-stage's translations had been carefully prepared to minimize any structural discontinuities between the connected sections. It should be noted that all operational parameters such as pulse energy, writing speed, depth of focus and so forth of the splitter fabrications in this section had imitated those of the straight waveguide inscriptions mentioned in the Section 5.1.

name	w_1 [μm]	w_2 [μm]	l_2 [mm]	Total loss [dB]		Splitting ratio	
				TE	TM	TE	TM
sp1	61.6	0	3.12	4.37 ± 0.16	23.67 ± 1.03	0.51:0.49	0.52:0.48
sp2	81.4	9.9	5.50	4.23 ± 0.14	21.99 ± 0.74	0.53:0.47	0.53:0.47
sp3	101.2	0	5.50	4.31 ± 0.20	22.62 ± 0.48	0.36:0.28:0.36	0.32:0.35:0.33
sp4	121.0	9.9	7.80	4.68 ± 0.21	23.73 ± 0.28	0.28:0.45:0.27	0.29:0.39:0.32

Table 5.2 Geometry parameters of the splitter's design, total insertion losses and splitting ratios of the fabricated beam splitters. The testing wavelength was at 1550 nm.

Examples of microscopic images recorded from the output facets of the beam-splitters sp1 and sp3 have been shown in Figure 5.8a and 5.8b, respectively. It can be noticed that the most written tracks had been appeared in the correct positions like in the diagrams in Figure 5.7. Also, the regions which were supposed to be an optical guiding core of the splitting branches had been clearly defined and contained no evidence of laser-induced crack or defect. The near-field intensity profiles of the beam splitters sp1, sp2, sp3 and sp4 measured in both modes of polarisations at a wavelength of 1550 nm have been presented in Figure 5.8c, 5.8d, 5.8e and 5.8f. It was clear that the beam in the TE state of polarisation could well propagate and split through the fabricated structures by means of the multi-mode interference. Although the profiles of split beams were not as symmetric and circular as those retrieved from the straight structures in the Section 5.1, they could still be considered their modes of propagation were excited in the nearly fundamental mode. In contrast, the mode fields in TM mode recorded from the splitter outputs had shown the lossy confinements and the irregular shapes of an intensity distribution. This behaviour of inferior guiding in TM polarisation could be potentially stemmed from either the modal radiation leakage (MRL) effects that was discussed in the Section 4.3 or the unsuitable geometry of a waveguide's multi-mode section that had been only optimized for the optical splitting of a beam in the TE-polarised state. It is worth mentioning the optimization process that was used was based on an iterative method, where the simulation geometry was systemically

altered to achieve the most stable guiding modes in the sections of multi-mode interference (MMI) and output branches. In addition, it was visualised in Figure 5.8 that the inclusion of lateral extension in the multi-mode waveguide section had resulted in the differences in the intensity profiles and the ratio of splitting beam, which were quantitatively measured and listed in the Table 5.2. Interestingly, if the total losses of splitters were compared to the losses of straight waveguides that were fabricated by similar set of inscription parameters in Section 5.1, the appended insertion losses in TE due to the additions of multi-mode and splitting branch sections can be calculated to

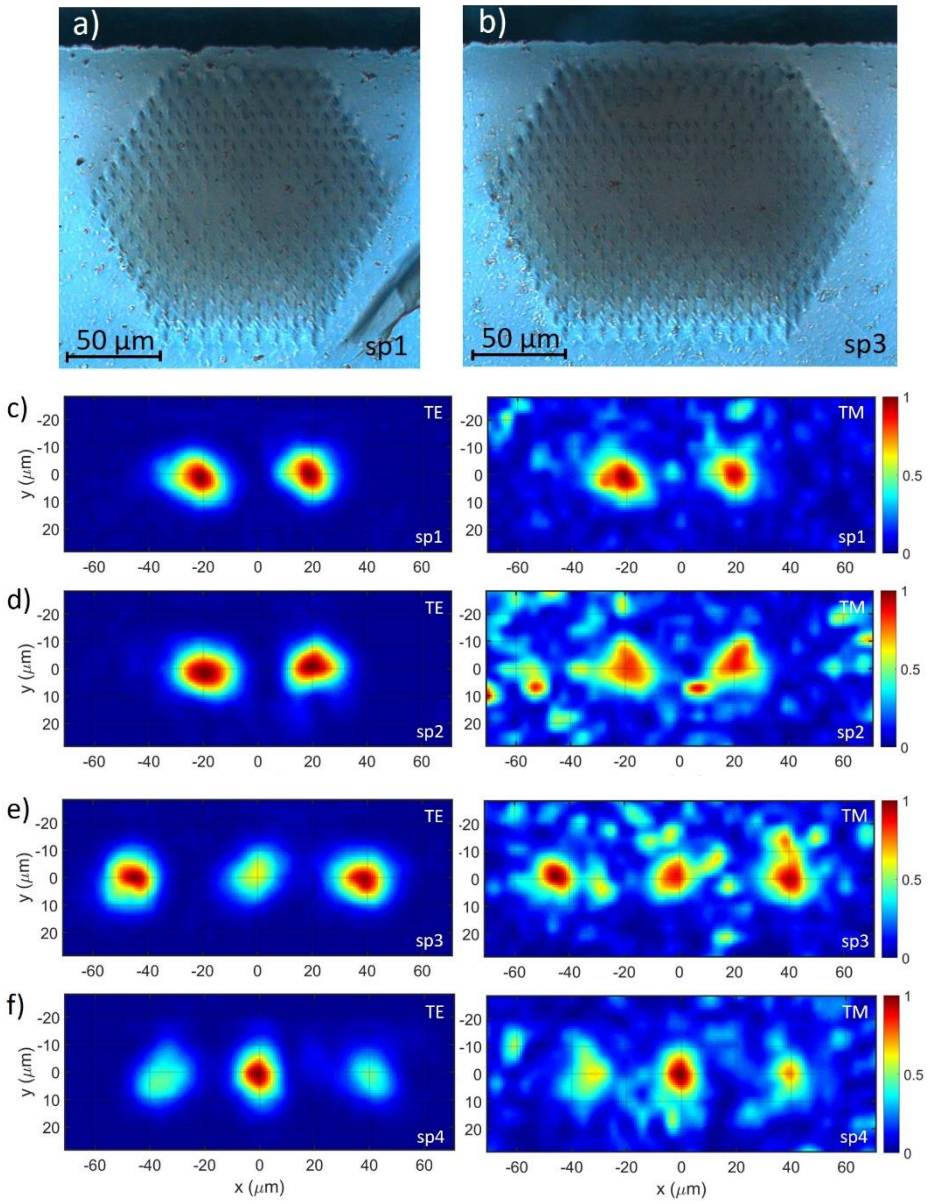

Figure 5.8 Cross-sectional microscopic images on the output facet of a) two-output splitter (sp1), and b) three-output splitter (sp3) after thermally annealed at 250 ºC for 3 hours. The near-field intensity ditributions measured from c) two-output splitter (sp1), d) two-output splitter with side extensions (sp2), e) three-output splitter (sp3) and f) three-output splitter with side extensions (sp4) in TE (left column) and TM (right column) modes. The testing wavelength was at 1550 nm.

be 0.28 dB and 0.36 dB for the splitter structures with two and three output-branches, respectively. These amount of additional losses were found to be relatively low if compared to the previous literatures of, for example, Lv *et al* [2] who utilized the conventional Y-splitter configuration and the optical-lattice-like waveguide geometry. Also, our sp1 structure required a shorter beam-splitting distance of ≈ 0.88 mm, which could greatly benefit in more compact size of a beam splitting device for an integrated photonic (IP) platform.

5.4 Structure integration of beam splitter and curve guiding channels for extending a separation of splitting branches

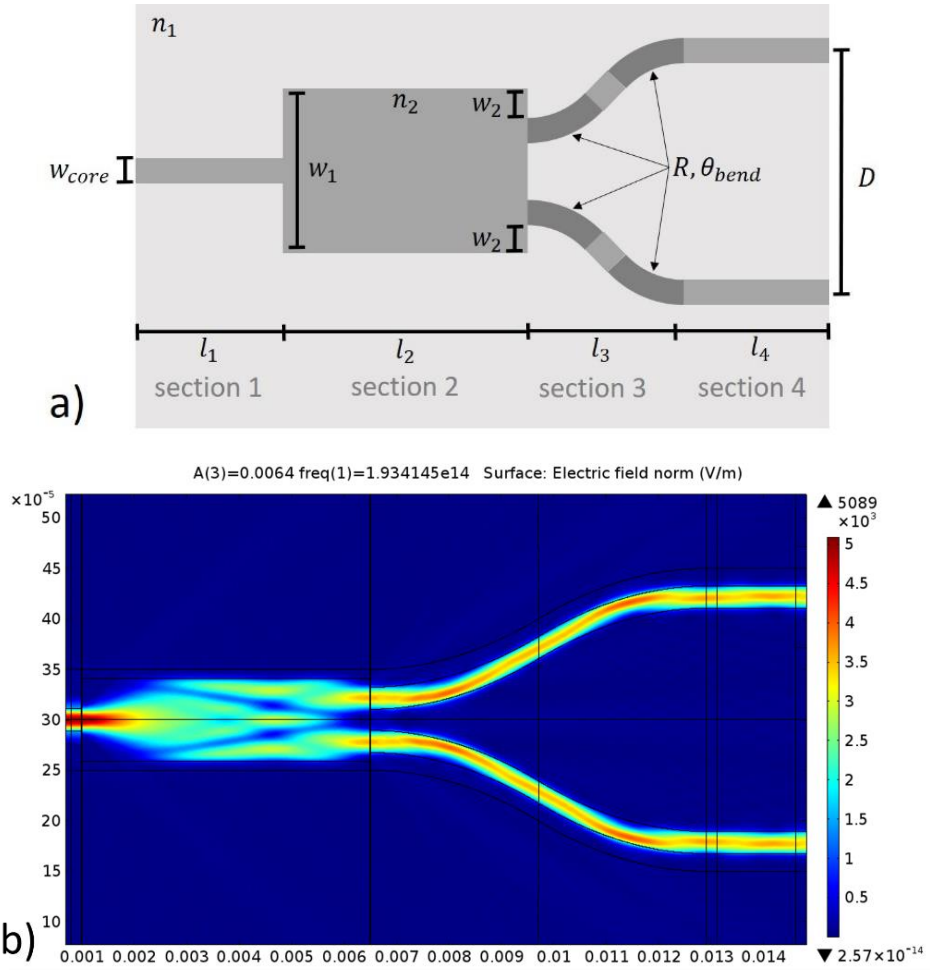

Figure 5.9 a) A diagram of a power splitter intergrated with bend waveguide structures. b) The simulation of beam propagtion mode in a structure shown in a). The wavelegnth of simulation was at 1550 nm.

A separation distance between the splitting branches of a beam splitter can be typically required to be extended up to several hundred micrometers, depending on the application of such optical splitting devices. To demonstrate this kind spatial extension of a distance between the output branches of a beam splitter in our work, the laser-inscribed structures of curvilinear

waveguides had been adapted and systemically optimized for integrating into the beam splitter's output channels. As depicted in Figure 5.9a, the curvilinear waveguide structures were located next to the beam-output channels of the multi-mode interference section. Some parameters, such as $w_1 = 80$ μm, $w_2 = 9.9$ μm and $l_2 = 5.5$ mm, that defined the geometry of a multi-mode guiding section had been taken from the structure of beam splitter sp2 presented in the Section 5.2. For the curvilinear parts, the parameters including a radius of curvature (R) and a bending angle (θ_{bend}) had been chosen in the ranges that showed low optical losses according to the experimental results in the Section 5.1. By using the numerical simulations in a Comsol Multiphysics software with the values of geometry parameters previously mentioned, the study showed that the beam's propagation mode simulation with the $R = 100$ mm and $\theta_{bend} = 2^o$ resulted in the high optical transmission from the splitting brances which were separated by a distance (D) of ≈ 293.7 μm, see Figure 5.9b. It can be observed that when the beam passed into the section 2 an optical interference occured and caused the beam to split into two steams, which were continuously passed through the curvilinear guiding chanels. It should be mentioned that the refractive indice of the core (n_1) and the cladding (n_2) were 2.2129 and 2.2111, respectively, which were similar to those values used in the computer simulations of power splitters in the Section 5.2.

In the fabrication processes of the beam splitter with curvilinear sections, the setups of a femto-second laser inscription and the pulse-energy variation scheme were identical to those of the experiments for the structure wg_7R in the Section 5.1 and the splitter sp2 in the Section 5.2. Although there were multiple components of differing configurations being combined, the writing path of inscribed tracks had been carefully organized so that the structure discontinuities between components, which could add the optical losses, were lessen. Examples of track's inscription paths were presented in Figure 5.10, where a row number corresponded to the order of row of track aligned in the cross-sectional plane. Note that this row orders were equivalent to the index *m* labelled in Figure 4.7, but here the row number had been shifted by four due to the increase of total hexagonal lattice layer (from 4 layers to 7 layers). For instance, the row number 8 in Figure 5.10 indicated the middle row of the structure cross-section, instead of *m* = 5 in Figure 4.7.

Figure 5.11a and 5.11b show the microscopic images of the beam splitter's cross-section recorded from the input and output facets, respectively. Most laser-inscribed tracks were observed to be correctly aligned, which resulted in the symmetric cladding regions and the well-defined guiding cores. In Figure 5.11c, a series of microscopic images of the fabricated power splitter recorded from the top-view direction have been presented. The images were arranged in sequence starting from the input facet (the most left image) to the output facet (the most right image). It can be seen that the written tracks showed a smooth-structure appearance and contained a low level of lattice defects. There was no overlap of tracks, which could be caused by the structure -

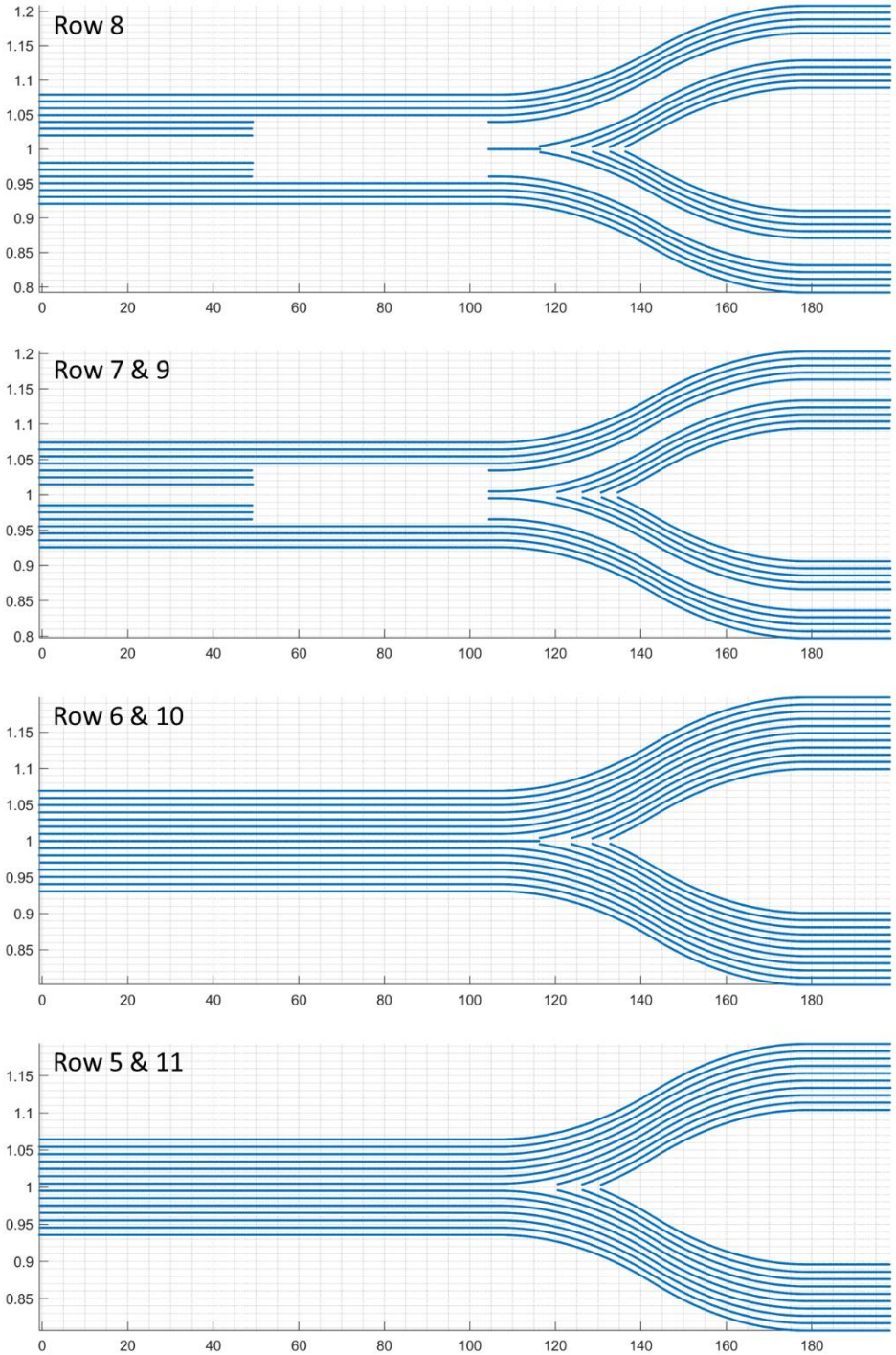

Figure 5.10 The track's inscription paths of the splitter and curve structure looked in the vertical direction. The row 8 indicates the middle vertical row. The row orders of lower/higher indices indicate the upper/lower positions on the waveguide's cross-section, see Figure 4.1 for an example.

misalignment, observed from the microscopic images. The near-field intensity profiles, in Figure 5.11d, demonstrated that the beam outputs from splitting branches could be separated by the nearly corrected distance of ≈ 293.7 μm. The measured intensity profiles suggested that the

fundamental mode of beam propagation was mainly excited in both perpendicular polarisation states of TE and TM. The total insertion losses of (4.96 ± 0.17) dB and (24.90 ± 0.32) dB were retrieved at a wavelength of 1550 nm for the polarisation states of TE and TM, respectively. In comparison with the structure of straight waveguide wg_7R in the Section 5.1, the additional parts of multi-mode interference and curvilinear waveguides in the structure presented in this section had caused the extra losses of approximately 1.01 dB in TE-polarised state and 1.33 dB in TM-polarised state. Also, the nearly-balanced splitting ratios of 0.48:0.52 and 0.47:0.53 could be achieved for the TE and TM modes, respectively. It should be mentioned that the total length of this beam splitter and curvilinear structure was ≈ 2.5 cm, and the length its of multi-mode guiding section for splitting the beam was ≈ 5.5 mm.

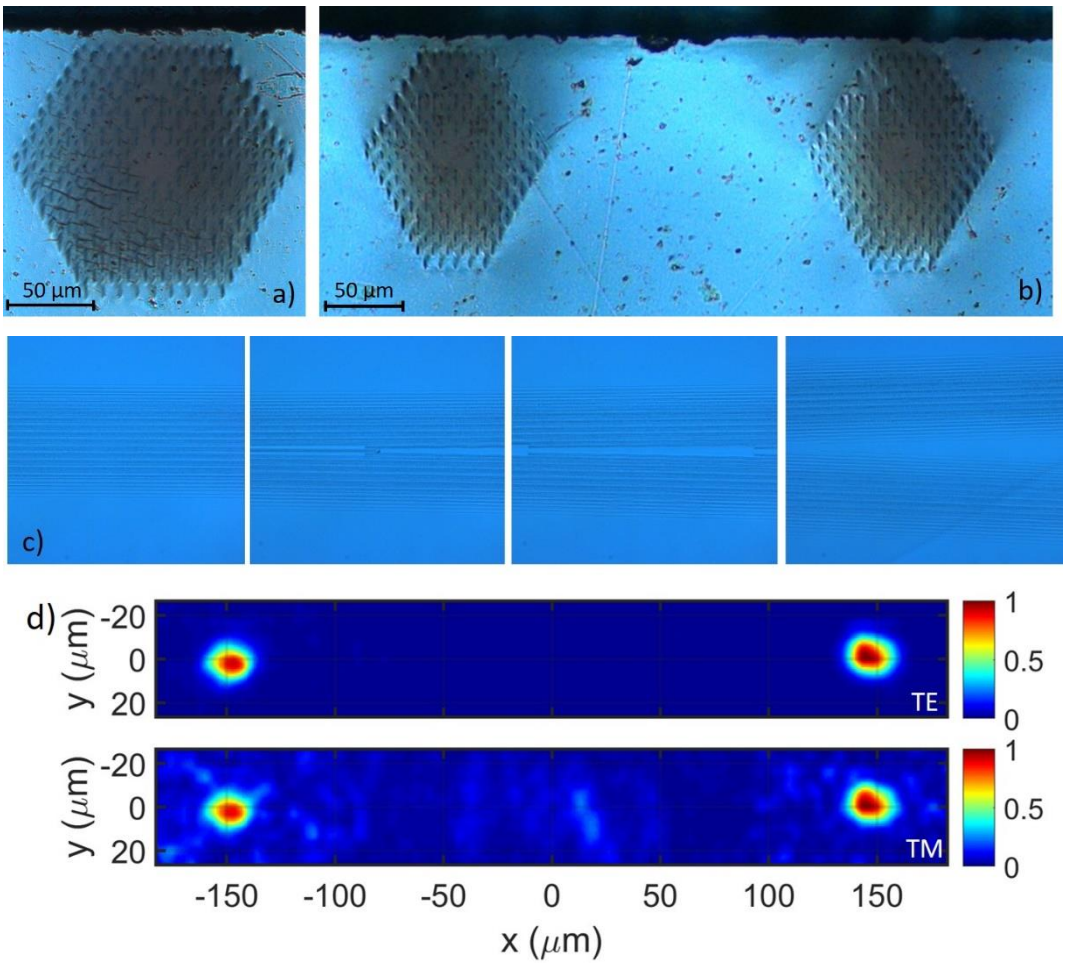

Figure 5.11 The microscopic images of the splitter and curve structure's cross-section captured from a) the input facet and b) the output facet. c) The top-view images of the structure. d) The near-field intensity distribution of the splitter and curve structure in TE and TM mode at a wavelength of 1550 nm.

Discussions and summary

In this chapter, the potential uses of a femto-second laser inscription technique for fabricating an optical device structure with more structure complexities and functionalities have been revealed. In fact, the fabrication strategies and the optimized range of inscription parameters which had been previously reported in the earlier chapters have been adapted (with some modifications) to the works in this chapter to achieve the optical structures with a high optical confinement and also a fundamental mode guiding. This chapter has demonstrated the fabrications of the curvilinear waveguide structures and the multi-mode interference beam splitter by using the direct-writing technique via the femto-second laser pulses with a high repetition rate. Also, the chapter has presented a structure integration of the beam splitter and the curvilinear guiding channels for extending a separation distance between the splitting arms. In addition, the computer simulations in a Comsol Multiphysics software had been utilized for predicting and optimizing the optical guiding characteristics of the fabricated devices.

In the Section 5.1 and 5.2, the influences of a waveguide's cladding thickness on the optical guiding performances of straight and curvilinear structures were investigated at a testing wavelength of 1550 nm and in two states of perpendicular polarisations. The thickness of waveguide cladding regions was altered by changing the number of track's hexagonal layers that were comprised in the optical-lattice-like packing. There were two values of 4 (named 'wg_4R') and 7 (named 'wg_7R') layers which resulted in the cladding thickness of around 40 and 70 μm, respectively, were used in the study. It has been found that the increase of the layer number from 4 to 7 layers slightly reduced the optical propagation losses from (0.65 ± 0.08) dB/cm to (0.45 ± 0.03) dB/cm in the TE-polarised state. Also, it could be observed no significant difference in the guiding intensity profiles between the wg_4R and wg_7R. For the test of curvilinear structures, the results also showed no significant difference in the overall guiding properties between the wg_4R and wg_7R sets, except that in the range of small curvature radii between 20 and 40 mm in which the wg_4R performed lower loss in the TE mode. In fact, these results actually supported the finding of a relationship between the layer number and the electric field transmission obtained from the computer simulations in the Section 4.1. Thus, this could give a good evidence on an estimated value of the effective refractive index changes which were induced by the laser pulses used in this experiment.

The Section 5.3 has demonstrated the fabrication results of laser-inscribed beam splitters that had the beam splitting mechanism based on the multi-mode interference. The structure geometry of the splitters with two and three splitting arms were designed and optimized for a guiding wavelength of 1550 nm and the TE-polarised state by using the computer simulations in a Comsol Multiphysics software. The simulation results suggested two configurations of the

multi-mode waveguide section, which either included or excluded the lateral guiding-region extension with a width w_2 of 9.9 μm. The minimum insertion losses in TE mode of (4.23 ± 0.14) dB and (4.31 ± 0.20) dB were achieved in the splitter with two and three splitter branches, respectively. Since the splitter's geometry had been systemically optimized and the track's writing paths had carefully organised for creating less discontinuities, the low optical losses of ≈ 0.28 dB and ≈ 0.36 dB for the two- and three-arm beam splitters, respectively, could be measured in addition to the reference structure of straight waveguide 'wg_7R'. Also, the records of near-field intensity profiles of the output beams had revealed the nearly fundamental mode for the optical guiding in TE polarisation. In comparison with other literature, our structures of multi-mode-interference beam splitters were found to operate with a lower optical attenuation and occupy in a smaller footprint, which could greatly benefit on a platform of integrated photonic (IP).

The structure integration of an optical power splitter and curvilinear guiding channels in the same fabrication stage of a laser inscription have been demonstrated in the Section 5.4. The beam splitting section was adapted from the beam splitter with two output branches, which had been optimized in the Section 5.2 for a high intensity transmission and a fundamental-mode propagation. The radius of curvature and bending angle of the curvilinear waveguide section of 100 mm and 2^o, respectively, had been chosen to achieve the total separation distance between the splitter's arms of ≈ 293.7 μm and to still maintain the low level of optical attenuations. The results showed that the structure could properly function in splitting the input beam into two steams of nearly-circular and fundamental-mode intensity profiles, and separating them with the separation distance that was designated without any sign of light scattering or leakage in the vicinity of non-guiding areas. The low insertion losses of (4.96 ± 0.17) dB and (24.90 ± 0.32) dB were achieved at a wavelength of 1550 nm in the TE- and TM-polarised state, respectively. By subtracting these losses with that of the straight waveguide wg_7R presented in the Section 5.1, the additional losses that were stemmed from the multi-mode guiding and curvilinear waveguide parts could be calculated approximately 1.01 and 1.33 dB for the TE and TM polarisations, respectively. Also, the nearly-balanced splitting ratios of 0.48:0.52 could be measured from two branches of the fabricated beam splitter. To the best of our knowledge, there is not yet any literature that has reported on this kind of laser-inscribed integrated structure in a material substrate of lithium niobate crystal. Thus, our results in this chapter has revealed the possibility in using this technique of ultrafast pulsed laser inscription, which have been thoroughly studied in this thesis, for the fabrications of many kinds of optical device that contain highly complex and multi-functional components. In fact, the fabrication strategies and experimental techniques suggested here have paved the way for further developments on the laser-inscribing technique for manufacturing of the three-dimensional and complex integrated photonic (IP) devices, with no

limitation on the material platform, that can be suitably used in a number of applications such as a high-speed data intercontact, an optical processing circuits, a photonic sensing device and so forth.

References

[1] D. E. Zelmon, D. L. Small, and D. Jundt, "Infrared corrected Sellmeier coefficients for congruently grown lithium niobate and 5 mol. % magnesium oxide–doped lithium niobate," *J. Opt. Soc. Am. B, JOSAB*, vol. 14, no. 12, pp. 3319–3322, Dec. 1997, doi: 10.1364/JOSAB.14.003319.

[2] J. Lv, Y. Cheng, J. R. V. de Aldana, X. Hao, and F. Chen, "Femtosecond Laser Writing of Optical-Lattice-Like Cladding Structures for Three-Dimensional Waveguide Beam Splitters in $LiNbO_3$ Crystal," *Journal of Lightwave Technology*, vol. 34, no. 15, pp. 3587–3591, Aug. 2016, doi: 10.1109/JLT.2016.2573841.

Chapter 6

Conclusions and Future Perspectives

6.1 Conclusions

This thesis has demonstrated the fs-laser micromachining of the straight waveguides, s-bend structures and power splitters that showed low optical loss on the z-cut wafer of lithium niobate. The use of fs-laser pulses with high-repetition-rate has revealed the benefits in not only the faster inscription speed, but also the inscribed structures that still preserved the light guiding after the thermal annealing at high temperatures.

The impacts of inscribing parameters on the optical and physical properties of the laser-modified regions have been reported. Also, the numerical analysis was conducted to study the conditions of laser focus under the effects of spherical aberration and birefringent astigmatism. The heat treatments at temperature up to 500 ^{o}C were shown to enhance the overall refractive index contrast and to erase some residual stress fields. The annealing at higher temperatures appeared to deteriorate the inscribed structures.

The depressed-cladding waveguides were fabricated in the geometry of optical-lattice-like packing, which consisted of 4 hexagonal rings of the Type-II damage tracks. Two suggested schemes of pulse-energy variations were applied, resulting in some unique advantages. The use of vertical variation scheme, where the pulse energy was linearly increased with the increasing focus depth, was found to suffice the compensation of energy-density declines stemmed from the spherical aberration occurred in this depth range. Thus, the cladding of waveguide implemented this scheme showed more symmetric size and strength in the refractive index modifications. The radial variation scheme, where the tracks close to the waveguide's core were written with lower pulse energy to reduce the laser-induced defect and stress, was found to noticeably widen the mode-field diameter but slightly increase the loss. Hence, this suggest a potential use for manipulating a spatial intensity profile of the waveguide's output. The lowest propagation losses of (0.4 ± 0.1) dB/cm and (3.5 ± 0.2) dB/cm for TE and TM polarised light, respectively, at 1550 nm were achieved after thermally annealed at 350 ^{o}C for 3 hours. In fact, the waveguides were found to be thermally stable and able to confine the light with low loss up to the temperature of 700 ^{o}C. Also, the fundamental guided mode was observed over a wide range of spectral between 500 nm and 1550 nm.

The increase in waveguide's cladding thickness (from 4 to 7 hexagonal rings) was found to slightly decrease the propagation loss in a straight waveguide, but it was found to increase the loss in the curve structures when the bending radius was less than 60 mm. The numerical simulations in COMSOL were used to design the optimal geometry for the multi-mode interference splitters with two and three outputs. The lowest insertion losses in TE mode of (4.23 ± 0.14) dB and (4.31 ± 0.20) dB for the two-output and three-output splitters, respectively, at 1550 nm were measured after the annealing at 250 ^{o}C for 3 hours. Plus, the integration of s-bends and splitter structure was demonstrated to achieve the low insertion loss of (4.96 ± 0.17) dB with the splitting ratio of 0.48:0.52 for TE mode at 1550 nm. Note that if compared to the reference straight waveguide, this structure showed an additional loss of approximately 1.01 dB.

6.2 Future perspectives

As mentioned in the previous section, this thesis has demonstrated the developments and optimizations of fs-laser writing technique to fabricate the optical guiding structures with low loss and high thermal-stability. The technique was also able to apply for writing the structures with higher degree of complexity such as s-bend and various designs of multi-mode interference power splitters. Besides, it was demonstrated that the integration of multiple optical elements is possible for our waveguide's geometry. However, in order to realise this fabrication technique for the commercial-scale manufacture of applications such as telecommunication interconnects, integrated optical sensors, signal-processing photonic circuits, and so forth, there are still several challenging tasks needed to be explored. Firstly, the methods for minimizing the undesired effects such as spherical aberration, birefringent astigmatism and self-focusing that distort the laser focus and, consequently, limit the inscription depth will be required to incorporate to our system. Various techniques of adaptive beam shaping may need to be chosen and accordingly adapted for this task. Secondly, an in-situ detection system of laser parameter as well as the feedback analysis software should be developed to allow the precise and real-time controls of laser-induced structure's properties. Last but not least, when the structures for inscription become more highly complex, it will be very necessary to construct a dedicated software that assists in designing the inscribing geometry and also optimizing the overall structure's performances. The numerical technique of conformal mapping [1], [2], for instance, can be implemented in the optimization software to simplify the simulation domains of a complex waveguide geometry and to improve the accuracy of computational analysis when combined with the finite element method [3]. Other advanced packing geometries such as spiral [4], [5] and aperiodic shapes, as well as the different inscribing-parameter variation schemes, can be also applied to the waveguide fabrication to further reduce the loss and/or to manipulate the guided mode-field.

References

[1] R. Schinzinger, P.A.A. Laura, “Conformal Mapping: Methods and Applications,” Dover Publ., 2003.

[2] R. Mittra, Ed, “Computational Electromagnetics: Recent Advances and EngineeringApplications,” Springer, 2014.

[3] A. Agrawal, B.M.A. Rahman, “Finite Element Modelling Methods for Photonics,” Artech House, Massachusetts, 2013.

[4] A. Agrawal et al., "Soft glass equiangular spiral photonic crystal fiber for supercontinuum generation," IEEE Photon.Technol. Lett., 21, 1722-1724 (2009).

[5] A. Agrawal et al. "Golden spiral photonic crystal fiber: polarization and dispersion properties," Opt. Lett., 33, 2716-2718 (2008).

Publications and Conferences

List of publications

1) T. Piromjitpong, M. Dubov, and S. Boscolo, “High-repetition-rate femtosecond-laser micromachining of low-loss optical-lattice-like waveguides in lithium niobate,” in Nonlinear Optics and its Applications 2018, 2018, vol. 10684, p. 106840D.

2) T. Piromjitpong, M. Dubov, and S. Boscolo, “High-repetition-rate Femtosecond-laser Inscription of Low-loss Thermally Stable Waveguides in Lithium Niobate,” in Frontiers in Optics / Laser Science (2018), paper JTu3A.34, 2018.

3) T. Piromjitpong, M. Dubov, and S. Boscolo, “High-repetition-rate femtosecond-laser inscription of low-loss thermally stable waveguides in lithium niobate,” Appl. Phys. A, vol. 125, no. 5, p. 302, Apr. 2019.

4) T. Piromjitpong, M. Dubov, and S. Boscolo, “Femtosecond laser writing of multi-mode interference power splitters and bend waveguide structures in lithium niobate,” (prepared)

List of conferences

1) SPIE Photonics Europe 2018, Strasbourg, France, 22 – 26 April 2018. (Oral presentation)

2) IOP Photon 2018, Birmingham, United Kingdoms, 3 – 6 September 2018. (Oral presentation)

3) OSA Frontiers in Optics 2018, Washington, DC, United States, 16 – 20 September 2018. (Poster presentation)